

PARTITIONED BY PROCESS: MEASURING POST-FIRE DEBRIS FLOW AND
RILL EROSION WITH STRUCTURE FROM MOTION

by

Nicholas Ellett

A thesis

submitted in partial fulfillment

of the requirements for the degree of

Master of Science in Geoscience

Boise State University

May 2019

© 2019

Nicholas Ellett

ALL RIGHTS RESERVED

BOISE STATE UNIVERSITY GRADUATE COLLEGE

DEFENSE COMMITTEE AND FINAL READING APPROVALS

of the thesis submitted by

Nicholas Ellett

Thesis Title: Partitioned by Process: Measuring Post-Fire Debris Flow and Rill Erosion
with Structure from Motion

Date of Final Oral Examination: 08 March 2019

The following individuals read and discussed the thesis submitted by student Nicholas Ellett, and they evaluated his presentation and response to questions during the final oral examination. They found that the student passed the final oral examination.

Jennifer Pierce, Ph.D. Chair, Supervisory Committee

Nancy Glenn, Ph.D. Member, Supervisory Committee

Jaime R. Goode, Ph.D. Member, Supervisory Committee

The final reading approval of the thesis was granted by Jennifer Pierce, Ph.D., Chair of the Supervisory Committee. The thesis was approved by the Graduate College.

ACKNOWLEDGEMENTS

Funding provided by Boise State University Department of Geosciences Burnham Family Research Fund, Boise State Department of Geosciences Teaching Assistantship, and Geological Society of America Student Research Grant to Nicholas Ellett. Boise National Forest and the Lowman Ranger District provided logistical support.

ABSTRACT

In mountainous regions burned by wildfires, profound changes in soil characteristics and combustion of vegetation increase hillslope and channel erosion during storm events. Reduced infiltration and abundant loose sediment produce large post-fire erosional events which endanger human lives and infrastructure and contribute significantly to long-term erosion rates. While the influence of fire in increasing erosion has long been recognized, quantifying volumes and sources of eroded material from burned landscapes is difficult. Pre-erosion high-resolution topographic data (e.g. lidar) are often not available in burned areas and determining specific contributions from post-fire hillslope and channel erosion is challenging. Multiple erosional processes mobilize sediment from hillslopes, but the connectivity of hillslopes to channels controls the basin-wide erosional response.

We quantify an important spatial threshold separating hillslope and channel erosion processes in a catchment burned in the 2016 Pioneer Fire. Further, we confirm the impact of post-fire erosion on landscape evolution, demonstrate the applicability of Structure from Motion photogrammetry (SfM) to quantify post-fire erosion without detailed pre-erosion topography, and improve estimates of rill erosion at adequate spatial scales. In this rugged 0.95 km² watershed in the weathered Idaho Batholith, widespread rilling and channel erosion produced a runoff-generated debris flow following modest precipitation in October 2016. We implemented unmanned aerial vehicle (UAV)-based SfM to derive 5 cm resolution topography of the channel scoured by debris flow. Lacking

cm-resolution pre-erosion topography, we created a synthetic surface defined by the debris flow scour's geomorphic signature and used a DEM of difference (DoD) to map and quantify channel erosion, finding $3467 \pm 422 \text{ m}^3$ was eroded by debris flow scour. Rill dimensions along hillslope transects and Monte Carlo simulation show rilling eroded $\sim 1100 \text{ m}^3$ of sediment and define a volume uncertainty of 29%. Next, we delineated sub-basins within the larger study catchment to investigate the evolution of hillslope and channel erosion with varying contributing areas. We document that a drainage area of 20 ha (0.2 km^2) represents the threshold from dominantly hillslope to dominantly channel erosion in this setting. Hillslopes contribute less to total erosion as drainage area increases, reflecting increased connectivity and efficiency of channel networks. Our experimental sub-basin results show a positive relationship between sediment yield (mass/area/time) and drainage area; contrary to most literature. The modern deposit volume was $5700 \pm 1140 \text{ m}^3$, indicating $\sim 60\%$ contribution from post-fire channel erosion. Our measured total eroded volume ($4600 \pm 740 \text{ m}^3$) aligns closely with the preliminary assessment from the US Geological Survey (USGS) post-fire hazard model for similar, modest precipitation intensities.

Holocene alluvial stratigraphic sequences exposed by the 2016 debris flows show fire-related deposition dominates the stratigraphic record. Dating of charcoal fragments preserved in stratigraphy at the catchment outlet and reconstructions of prior deposit volumes provide a record of Holocene fire-related debris flows at this site. Comparisons of fire-related sediment yields from episodic events with Holocene sediment yields reconstructed from other studies in the region suggest episodic wildfire-driven erosion dominates millennial-scale erosion. Further investigations into spatial thresholds of post-

fire erosion, hillslope-channel connectivity, and long-term landscape changes, especially when coupled with high resolution topography, will help to quantify the impacts of wildfire in other settings.

TABLE OF CONTENTS

ACKNOWLEDGEMENTS	iv
ABSTRACT	v
LIST OF TABLES	xi
LIST OF FIGURES	xii
PARTITIONED BY PROCESS: MEASURING POST-FIRE DEBRIS FLOW AND RILL EROSION WITH STRUCTURE FROM MOTION PHOTOGRAMMETRY	1
Abstract	1
Introduction	3
Study Site	6
October 2016 Precipitation and Debris-flow Events	7
Methods	12
Deposit Stratigraphy, Radiocarbon Ages, and Deposit Volumes	12
Erosion Rates and Sediment Yields	15
Hillslopes and Rill Eroded Volume	15
Calculation of Minimum Channel Erosion Volume	17
Structure from Motion Methods	18
Structure from Motion Error Analysis	24
Results	26
Channel Erosion	26
Structure from Motion Error	29

Eroded Volumes from Hillslopes and Rills	29
Deposit Stratigraphy, Radiocarbon Ages, and Deposit Volumes	32
Erosion Rates and Sediment Yields	33
Discussion	34
Precipitation Characterization and Context for Debris-flow Prediction....	34
Structure from Motion: Accuracy, Advantages, and Recommendations ..	36
Post-Fire Erosion Processes	38
Partitioning of Erosion Processes	41
Modern and Holocene Erosion Rate and Sediment Yield Comparison....	44
Conclusion	48
AN ISSUE OF SCALE: CONTRIBUTING AREA AND POST-FIRE EROSION	50
Abstract	50
Introduction	51
Study Site, Debris Flow Occurrence, and Field Observations.....	53
Methods.....	57
Results.....	58
Discussion	63
Uncertainty and Assumptions:	63
Channel Erosion Outpaces Hillslope Erosion as Drainage Area Increases.....	65
Spatial Threshold at 20 ha Drainage Area	66
Inconsistent Sediment Yield and Drainage Area Relationship.....	67
Hillslope Contribution as a Function of Drainage Area	73
Conclusion	74

REFERENCES	76
APPENDIX A.....	89
Structure from Motion Methods	89
APPENDIX B	109
Radiocarbon data	109

LIST OF TABLES

Table 1.1:	Summary of ground control points (GCPs), their RTK-GPS accuracy, and Agisoft-processed SfM root-mean-square error (RMSE). The 0.076 m (7.6 cm) total error includes all 20 available GCPs. For our SfM error analysis and volume uncertainty scenario 2 we randomly selected 10 GCPs to serve as control points, calculated the error, and repeated 3 times, resulting in 6.6 cm overall RMSE.....	19
Table 1.2:	Summary of eroded volumes and uncertainties. Values in bold used for analysis and discussion	27
Table 1.3:	Radiocarbon dates from charcoal fragments preserved in stratigraphy at study catchment outlet.	33
Table 1.4:	Estimated deposit volumes and conversions to catchment-averaged sediment yield and erosion rate. The deposit volumes represent single events based on stratigraphy and radiocarbon ages. The sediment yield and erosion rate are calculate including overlying deposits to represent longer-term averages.	34
Table 2.1:	Study catchment sub-basin data used in figures 2.2, 2.3, 2.4	60
Table 2.2:	Literature sediment yield and drainage area data used in figures 2.5 and 2.7.....	68

LIST OF FIGURES

- Figure 1.1: A) geographic setting within Idaho, USA. Orange outline is extent of 2016 Pioneer Fire. B) USGS Post-Fire Debris-flow Hazard model results for probability of debris-flow occurrence under 16 mm/hr peak 15-minute precipitation in the Clear Creek watershed. Study catchment is outlined in white. 10
- Figure 1.2: A) National Agricultural Image Program (NAIP) image of study site from 2013 (pre-fire). B) NAIP image of study site from 2017 (post-fire and post-debris-flow). C) Slope map of study area. 50 m contours for scale. D) Soil Burn Severity map from USFS Burned Area Emergency Response (BAER). 50 m contours for scale. 11
- Figure 1.3: A) Image of study catchment outlet post-fire and pre-debris-flow, taken from USFS helicopter. B) UAV image of debris-flow fan deposit. Orange rectangle marks approximate location of described and dated stratigraphy (Fig 4). C) Image of scoured channel from first visit to site, 9 days after debris-flow. Note mud lines, scarred trees and roots, and abrupt channel margins. D) UAV image of rilling on hillslope, arrows highlight individual rills. 12
- Figure 1.4: Fan deposit stratigraphy. Photo at left is 1 m upstream of described and dated section. At right, thicknesses and descriptions for units. Depths of dated charcoal fragments are shown by red triangles. In the field, we separated depths 10-130 cm into 3 units. Ages suggest they are from a single event. All deposits are fire-related except 130-150 cm depth. 14
- Figure 1.5: Study catchment detail. More detailed hillshade shows extent of SfM-derived 5 cm DEM. Green triangle is location of described and dated stratigraphic section (Fig 4). Black squares are locations of manually-surveyed channel cross-sections. Purple circles are locations of hillslope transects (n=15) scaled by the relative magnitude of rill erosion at each. Transects sample a range of slopes (14-37 degrees) and a variety of landscape positions. Blue diamonds mark channel head locations mapped in the field. 20 m contours shown for scale. 17
- Figure 1.6: SfM methods and error assessment. A) Perspective view of point cloud section. Blue flag represents an RTK-GPS ground control point. Blue squares represent locations and orientations of UAV images. Nadir images were acquired from several altitudes, while some oblique images were

collected to minimize distortion (e.g. James and Robson, 2014). Flow is from left to right in the image. B) Vertical RMSE for the processed point cloud compared to 20 RTK-GPS surveyed GCPs. A mix of positive (orange-red) and negative (blue-green) vertical errors indicates little systematic distortion of the analyzed DEM. 21

Figure 1.7: A) UAV detail image of channel eroded by debris-flow. Orange boxes are in same location to aid comparison. B) 10 cm contour intervals highlight abrupt channel margin. C) Synthetic, pre-erosion surface created by removing “scour” points. D) Diagram of assumption correcting total calculated volume for a generic, pre-erosion geometry. E) Point cloud perspective view of same channel segment, showing detailed topographic form and appearance of SfM point cloud. 23

Figure 1.8: A) DEM of Difference for debris-flow channel scour. Red values indicate erosion and blue values indicate deposition. SfM topography extent is shown as hillshade. 20 m contour interval for scale. B) Detail of DoD corresponding to Figure 1.7. C) UAV image of section of channel scoured to bedrock by debris-flow. Flow is from right to left in all panels. 28

Figure 1.9: Upper left, Boxplots of rill dimensions from full dataset (n=175) and rill counts per transect (n=15). Upper right, Monte Carlo simulation results showing variation in mean rill count per transect. Lower left, Monte Carlo simulation results showing variation in mean rill width (red) and depth (blue) dimensions. Lower right, Mean rill depth plotted against mean rill width, with linear best fit shown, note x and y axis scales. 31

Figure 1.10: Upper left, Boxplots of rill dimensions separated by aspect, and boxplots of mean rill count per transect separated by aspect. Upper right: Monte Carlo results showing variation in mean rill counts on north aspects (blue) and South aspects (red). Lower left, S aspect mean rill counts plotted against N aspect mean rill counts, note x and y axis scales. While not statistically significant, north aspects had about three times as many rills as South aspects. Lower middle, Monte Carlo results showing variation in rill width and depth, separated by north aspect (blue) and South aspect (red). Lower right: Mean rill depth plotted against mean rill width, separated by north aspect (blue) and South aspect (red). Linear best fits shown in black, note x and y axis scales. 41

Figure 1.11: Comparison of post-fire studies reporting contribution from channel erosion processes to total erosion. Channel processes include debris-flow, hyperconcentrated flow, and streamflow. Solid columns are from high-resolution topography and single catchments. Hollow columns are from other methods or averages from multiple catchments. Catchment sizes are 0.075 km² (DeLong), 0.5 km² (Meyer), various (Moody and Martin), 0.1-

2.2 km² (Nyman), 0.005 km² (Rengers), 0.5-5 km² (Santi), 0.07-0.2 km² (Smith), 0.01 km² (Staley), and 0.95 km² (this study). 44

Figure 1.12: Plot of erosion rates versus timescale of measurement from selected studies in discussion. Open symbols are data from Idaho, including this study shown in red. Closed symbols are from SW USA. Measurements of erosion rates are from a variety of methods and catchment sizes. Adapted from Kirchner et al., 2001 and Orem and Pelletier, 2016. 47

Figure 2.1: A) Area map of 2016 Pioneer Fire perimeter (orange) in Idaho. Yellow circle is study catchment location Study catchment contributes to Clear Creek. B) UAS (aerial) image of rills on planar hillslopes connecting to scoured debris flow channel. Arrows give direction of flow. C) Detail map of study catchment. 0.95 km² full extent outlined in gray. Extent of SfM 5 cm resolution DEM shown as hillshade. Red shading shows channel scour measured with DoD. Black triangles show locations of hillslope transect used to derive rill erosion volumes. Analyzed sub-basins are outlined. Labels at sub-basin outlets correspond to Table 2.1. 50 m contours for scale. 55

Figure 2.2: Eroded volumes from sub-basins within study catchment. Channel eroded volume surpasses hillslope eroded volume at a drainage area of about 20 hectares (0.2 km²). Channel erosion volumes also increase about three times faster than rill erosion volumes, reflecting increased integration and efficiency of channel networks. Total erosion volume (channel + rill) is shown in gray squares. Rill erosion volumes (triangles) are extrapolated from hillslope transect data and applied as a uniform 1.4 mm per unit area erosion where rilling was observed. Channel erosion volumes (X's) are from 5 cm resolution DEM of Difference derived from synthetic pre-erosion and surveyed post-erosion Structure from Motion survey. Orange circles are data from post-fire gully erosion, in similar Idaho Batholith terrain (Istanbulluoglu et al., 2003). 61

Figure 2.3: Sediment yield, in metric tons per hectare per year (mass/area/time) for sub-basins of varying size within the study catchment. Sediment yields increase as the scale of analysis increases, up to the 95 hectare study catchment size. Data from all drainage areas are fit with a power law function (black dashed line). Channel networks are not present at the smallest drainage areas. As drainage area increases, hillslopes are more closely coupled to channels and connectivity improves, allowing increased sediment yields. Green symbols represent contributing areas below 20 ha, where rill erosion contributes a majority of total erosion. Blue symbols represent contributing areas above 20 ha, where channel erosion contributes a majority of total erosion. Gray dashed lines are linear best fits above and below the 20 ha drainage area threshold, representing a change in process-dominance. A positive relationship between post-fire

sediment yield and drainage area is shown in other studies, e.g. Gabet and Bookter, 2008; Moody and Martin, 2009; Pelletier and Orem, 2014. Sediment yields are converted from measured eroded volumes using a bulk density of 1500 kg/m³. 62

Figure 2.4: Percent contribution of hillslope erosion (rilling) to total erosion for varying size sub-basins within the study catchment. At small drainage areas, erosion is entirely by hillslope erosion. As the drainage area increases and channels are present, the relative contribution of hillslope erosion diminishes. In this setting, the threshold between hillslope-process dominance and channel-process dominance (purple shading) occurs at a drainage area of about 20 hectares (0.2 km²). Data are fit with a power law function (dashed line). 63

Figure 2.5: Post-fire erosion literature values for sediment yield plotted against basin size. Sediment yield (t/ha) decreases as drainage area increases. A common explanation for this negative relationship is increased opportunities for sediment storage or deposition in larger catchments (Lane et al., 1997; Scott et al., 1998; Shakesby and Doerr, 2006; Wagenbrenner and Robichaud, 2014). However, this result seems at odds with data from sub-basins within our study catchment (Figure 2.3). Open circle symbols are measurements from multiple methods where basin sizes were clearly reported. Filled red diamond symbols are measurements from high-resolution topography (HRT) methods, this study is shown with purple squares. The HRT data are fit with a power law function (dotted line). 71

Figure 2.6: Conceptual diagram from Swanson (1981) illustrating the intermittent nature of post-fire sediment yields. 72

Figure 2.7: Post-fire literature values for the percent contribution of hillslope erosion to total erosion for varying basin sizes. At small drainage areas, hillslope processes contribute all or most erosion. As drainage area increases, channel processes become more dominant. Open circle symbols are measurements from multiple settings and methods where basin sizes were clearly reported. These data are fit with a power law function (black dashed line). Filled green triangle symbols are from high-resolution topography (HRT) methods, including this study shown with purple squares. HRT data are fit with a power law function (green dashed line). While taken from few data points, the similarity of fitted lines is encouraging. Variation in the literature values is reflective of diverse settings (geology, fire, precipitation, basin characteristics, etc) as well as multiple measurement methods. 73

PARTITIONED BY PROCESS: MEASURING POST-FIRE DEBRIS FLOW AND
RILL EROSION WITH STRUCTURE FROM MOTION PHOTOGRAMMETRY

Chapter under review for publication in Earth Surface Processes and Landforms

Abstract

After wildfire, hillslope and channel erosion produces large amounts of sediment and can contribute significantly to long-term erosion rates. However, pre-erosion high-resolution topographic data (e.g. lidar) is often not available and determining specific contributions from post-fire hillslope and channel erosion is challenging. The impact of post-fire erosion on landscape evolution is demonstrated with Structure from Motion (SfM) Multi-View Stereo (MVS) photogrammetry in a 1 km² Idaho Batholith catchment burned in the 2016 Pioneer Fire. We use SfM-MVS to quantify post-fire erosion without detailed pre-erosion topography and hillslope transects to improve estimates of rill erosion at adequate spatial scales. Widespread rilling and channel erosion produced a runoff-generated debris-flow following modest precipitation in October 2016. We implemented unmanned aerial vehicle (UAV)-based SfM-MVS to derive a 5 cm resolution digital elevation model (DEM) of the channel scoured by debris-flow. In the absence of cm-resolution pre-erosion topography, a synthetic surface was defined by the debris-flow scour's geomorphic signature and we used a DEM of Difference (DoD) to

map and quantify channel erosion. We found $3467 \pm 422 \text{ m}^3$ was eroded by debris-flow scour. Rill dimensions along hillslope transects and Monte Carlo simulation show rilling eroded $\sim 1100 \text{ m}^3$ of sediment and define a volume uncertainty of 29%. The total eroded volume ($4600 \pm 740 \text{ m}^3$) we measured in our study catchment is partitioned into 75% channel erosion and 25% rill erosion, reinforcing the importance of catchment size on erosion process-dominance. The deposit volume from the 2016 event was $5700 \pm 1140 \text{ m}^3$, indicating $\sim 60\%$ contribution from post-fire channel erosion. Dating of charcoal fragments preserved in stratigraphy at the catchment outlet, and reconstructions of prior deposit volumes provide a record of Holocene fire-related debris-flows at this site; results suggest that episodic wildfire-driven erosion ($\sim 6 \text{ mm/year}$) dominate millennial-scale erosion ($\sim 5 \text{ mm/Ka}$) at this site.

Keywords: Structure from Motion, post-fire erosion, debris-flow, rilling, Idaho

Introduction

Modern post-fire erosion demands attention. Anthropogenic climate change is exacerbating the size and severity of wildfires, leading to dramatic impacts on landscapes, ecosystems, human interests, and infrastructure (Goode et al., 2012; Abatzoglou et al., 2016; Sankey et al., 2017; Murphy et al., 2018). Pervasive post-fire erosion across steep landscapes exceeds background erosion rates by water-, gravity-, and wind-driven processes (Roering and Gerber, 2005; Shakesby and Doerr, 2006; Sankey et al., 2009; Moody et al., 2013). Hillslope and channel erosion processes interact with precipitation on steep, burned landscapes to produce and augment dramatic runoff-generated debris-flows (e.g. Meyer and Wells, 1997; Cannon et al., 2001; Gabet and Bookter, 2008). Runoff-generated debris-flows usually result from intense, convective precipitation in steep catchments, scouring channels and delivering large magnitudes of poorly-sorted sediment.

The occurrence and impacts of post-fire debris-flows are well documented (e.g. Cannon et al., 2010; Kean et al., 2011; Nyman et al., 2011), but questions remain about the relative contributions of hillslope and channel erosion to total sediment yield at various basin scales. In a range of basin sizes across the western United States, traditional surveying methods indicate post-fire channel erosion exceeds that from hillslopes (Santi et al., 2008; Moody and Martin, 2009). Hillslope processes, such as rilling, are difficult to measure across a landscape because they have small dimensions and are spatially variable. Prior efforts to measure rills in burned catchments are simplistic and do not report uncertainty (Meyer and Wells, 1997; Santi et al., 2008). Other workers have recorded erosion from hillslope plots (a few m²) under natural or simulated rainfall (e.g.

Benavides-Solorio and MacDonald, 2005; Pierson et al., 2009). However, plot-scale studies may miss the landscape-wide picture of erosion. Therefore, improving rill volume quantification, and its uncertainty, is required to more fully elucidate post-fire erosion processes.

Other recent work seeks to quantify the process-based erosion contributions using cm-resolution topography (e.g. terrestrial laser scanning, TLS) and multi-temporal change detection (e.g. DEM of Difference, DoD); several studies demonstrate that extensive hillslope erosion surpasses channel contributions (Staley et al., 2014; Rengers et al., 2016; DeLong et al., 2018). Staley et al. (2014) show that >80% of post-fire erosion is from hillslopes and note that more work is needed at a range of catchment scales to determine when and how channel erosion exceeds hillslope erosion.

TLS surveys achieve cm-resolution, capture small landscape details, and reveal the spatial fingerprints and magnitudes of post-fire erosion processes, but are limited by viewing angle, occlusion, and scan locations across larger scales and in rugged settings. These studies are focused on relatively small areas (a few hectares) where significant post-fire erosion is anticipated. Further, they usually depend on collecting topographic data with lidar prior to precipitation; possible in certain situations but not feasible everywhere. Structure from Motion, Multi View Stereo photogrammetry (simplified to SfM hereafter) represents a lower-cost, flexible alternative to acquire cm-resolution topographic data (Johnson et al., 2014).

SfM is an adaptation of traditional photogrammetry used to derive 3D information from imagery. SfM uses computer algorithms to match features from many overlapping digital images and create point clouds with x,y,z and r,g,b values at each point. As with

lidar, SfM point clouds are often gridded into DEMs during analysis. Many applications demonstrate SfM's flexibility including investigations of shallow river topography (Javernick et al., 2014), coral reef roughness (Leon et al., 2015), landslide monitoring (Stumpf et al., 2015), and dryland vegetation (Cunliffe et al., 2016). James and Robson (2014) and James et al. (2017) give encompassing discussions and provide suggestions to minimize SfM error including high-quality imagery with some convergent geometries, adequate spatial coverage of ground control points (GCPs), and the inclusion of GCP uncertainty in models. SfM has proven to be enormously flexible with accuracy and resolution comparable to TLS. Furthermore, coupling SfM techniques with an unmanned aerial vehicle (UAV) platform makes this technology viable for quantifying post-fire erosion over rough terrain at suitable extents and cm-resolutions

The majority of post-fire studies have temporal scopes restricted to the present or a few decades prior, and limited work has been done on post-fire erosion over Holocene and Quaternary timescales (Moody et al., 2013; Murphy et al., 2018). A handful of studies investigate erosion and sedimentation responses to wildfire driven by Holocene climate changes by dating charcoal fragments from alluvial fans (Meyer and Pierce, 2003; Pierce et al., 2004, 2011; Bigio et al., 2010; Nelson and Pierce, 2010; Weppner et al., 2013; Riley et al., 2015; Fitch and Meyer, 2016). Over Quaternary timescales, post-fire erosion is responsible for >90% of landscape denudation since 1.24 Ma at Valles Caldera, New Mexico (Orem and Pelletier, 2016).

Adding to our understating of post-fire erosion's role in landscape evolution requires temporal data beyond a few decades to place modern erosion magnitudes in a Holocene or even Quaternary framework. Additionally, combining an improved estimate

of rill erosion with high-resolution topography allows critical insights into the contributions of hillslope and channel processes to runoff-generated post-fire debris-flows.

Several primary research questions motivate this study: 1) How is channel and hillslope rill erosion partitioned following wildfire in a 1 km² Idaho Batholith catchment? 2) How can estimates of rill erosion, and their uncertainty, be improved? 3) In the absence of detailed pre-erosion topographic data, can SfM be used to map and quantify channel scour by runoff-generated debris-flow? A further goal of this study is to compare modern post-fire erosion with erosion over Holocene timescales. We apply cm-resolution SfM, traditional field work, and Monte Carlo simulation to quantify channel and rill eroded volumes and their uncertainties. We estimate paleo sediment yields at this site using radiocarbon dating of prior deposits. We then compare the Holocene values to observed modern post-fire erosion and to the results of similar studies.

Study Site

We studied a catchment within the ~35,000 km² Idaho Batholith in central Idaho which burned in the 2016 Pioneer Fire (Figure 1.1A). The Pioneer Fire began in July 2016 and burned ~750 km² of mountainous terrain on the Boise National Forest. Our study site is a steep, unnamed headwater catchment contributing to Clear Creek (Figure 2). Clear Creek drains 150 km² with 1500 m relief and receives 97 cm of precipitation per year (<https://streamstats.usgs.gov/ss/>, PRISM normals 1981-2010, accessed October 2018). Vegetation is mixed Ponderosa Pine (*Pinus ponderosa*) and Douglas Fir (*Pseudotsuga menziesii*) transitioning to Lodgepole Pine (*Pinus contorta*) and mixed conifer forests at high elevations with deciduous vegetation along riparian floodplains.

Over 80% (120 km²) of the Clear Creek drainage was burned at varying intensities in the Pioneer Fire (Burned Area Emergency Response

<https://fsapps.nwcg.gov/afm/baer/download.php?year=2016>, accessed October 2016).

The study catchment was burned around August 30, 2016 at moderate to high severities (Figure 1.2).

The study catchment is 0.95 km² in size, oriented approximately E-W, with elevations between 1778-2323 m. Mean catchment slopes are 26.2 degrees with a maximum of 45 degrees within the study catchment (Figure 1.2). Slopes are mostly soil-mantled with shallower, rockier soils and more bedrock outcrops on south aspects than north aspects. Latest-Pleistocene glacial features are present nearby in valleys above 2250 m elevation (Kiilsgaard et al., 2006), but mapped Quaternary deposits at the study catchment are limited to low stream terraces and fan gravel. The study catchment is underlain by biotite-granodiorite intruded approximately 75 Ma (Kiilsgaard et al., 2006) with sparse Eocene rhyolite and dacite dikes. The catchment was last logged in the late 1950's or early 1960s (D. Brown, personal communication, 2018). Most still-standing, burned trees have trunks <1 m diameter. Remnants of several skid roads are apparent on hillslopes.

October 2016 Precipitation and Debris-flow Events

The study catchment produced a debris-flow on October 15, 2016 following precipitation from a frontal-type storm. The Banner Summit Snow Telemetry (SNOTEL) site (20 km away, hourly resolution) recorded a maximum precipitation magnitude of 10 mm/hr (<https://wcc.sc.egov.usda.gov/nwcc/site?sitenum=312>, accessed September 2018). The Cozy Cove (~16 km away) and Jackson Peak (~18 km away) SNOTEL sites (also

hourly resolution) recorded maximum precipitation of 5 mm/hr and 8 mm/hr, respectively. For reference, the 2-year recurrence interval precipitation at this location is 61.2 mm in 24 hours (<http://www.nws.noaa.gov/ohd/hdsc/noaaatlas2.html>, accessed September 2018) and the estimated October 15, 2016 precipitation was 25 mm in 24 hours (<http://prism.oregonstate.edu/explorer/>, accessed September 2018). The complex topography surrounding our study site modifies, and likely enhances, the precipitation produced by frontal-type storms (e.g. Daly et al., 1994; Mock, 1996). High-temporal resolution precipitation data are not available within 4 km of the study site (Staley et al., 2016, 2017), and therefore we do not attempt to report specific forcing data (peak 15-minute intensity) for the studied debris-flow.

Our study catchment was the only basin to produce a debris-flow within the Clear Creek drainage, as determined from reconnaissance along the entirety of Clear Creek using road access in October 2016 and June 2017. Indeed, little evidence of fresh depositional response was noted at any other catchment outlets. While this is surprising given the burn severity, the lack of response from nearby basins results from the modest precipitation intensity from the October 15, 2016 storm. Other steep basins along the axial South Fork Payette did produce fire-related debris-flows, resulting in large sediment and wood inputs, and rearrangement of rapids on this recreationally popular river.

The US Geologic Survey (USGS) post-fire debris-flow hazard model provides a tool to quickly assess the probability of debris-flow occurrence and debris-flow volume in a basin receiving designed peak 15-minute precipitation intensities (Staley et al., 2016, 2017). The USGS post-fire debris-flow hazard map produced for the Pioneer Fire shows the study catchment has a debris-flow probability of 46% under 16 mm/hr peak 15-

minute rainfall intensity and 67% under 20 mm/hr peak 15-minute intensity (https://landslides.usgs.gov/hazards/postfire_debrisflow/detail.php?objectid=5, accessed October 2016). In all, 20 basins within the Clear Creek drainage have probabilities exceeding 45% at 16 mm/hr rainfall intensity (Figure 1.1B). These 20 basins have drainage areas ranging from 0.04 to 1.1 km² and the predicted debris-flow volumes range from 389 to 10751 m³.

Our preliminary visit to the study site was on October 24, 2016, 9 days after the debris-flow. We were not able to conduct extensive field work at this time, but we made observations of the debris fan deposit and the lower section of channel. Clear Creek had already incised through the debris fan and carried some material downstream. Ash and charred organic matter were several centimeters thick upstream of the debris fan and in local depressions, indicating some redistribution and ponding post debris-flow. Ash was present on nearly all surfaces except where fresh sediment was exposed or deposited (i.e. channel and fan). Woody debris ranging from small branches to large trunks was entrained throughout the debris fan and was most abundant at the toe. The character and thickness of deposits varied, indicating several types of flow with changing sediment to water ratios (i.e. debris-flow, hyperconcentrated flow, and streamflow), and levees were present but not well-defined on the fan surface. The scoured channel had distinct margins and a striking rectangular cross section. The channel sides exposed and cut through roots, and the channel bed was scoured to fresh bedrock in multiple locations (Figure 1.3). Large-caliber sediment and woody debris were deposited upstream of obstructions within the channel and along the sloping margins. Mud lines and matted, in-situ vegetation were

present up to 3 m above the freshly-scoured channel bed. We did not make observations of the upper channel reaches or much of the hillslopes during this preliminary visit.

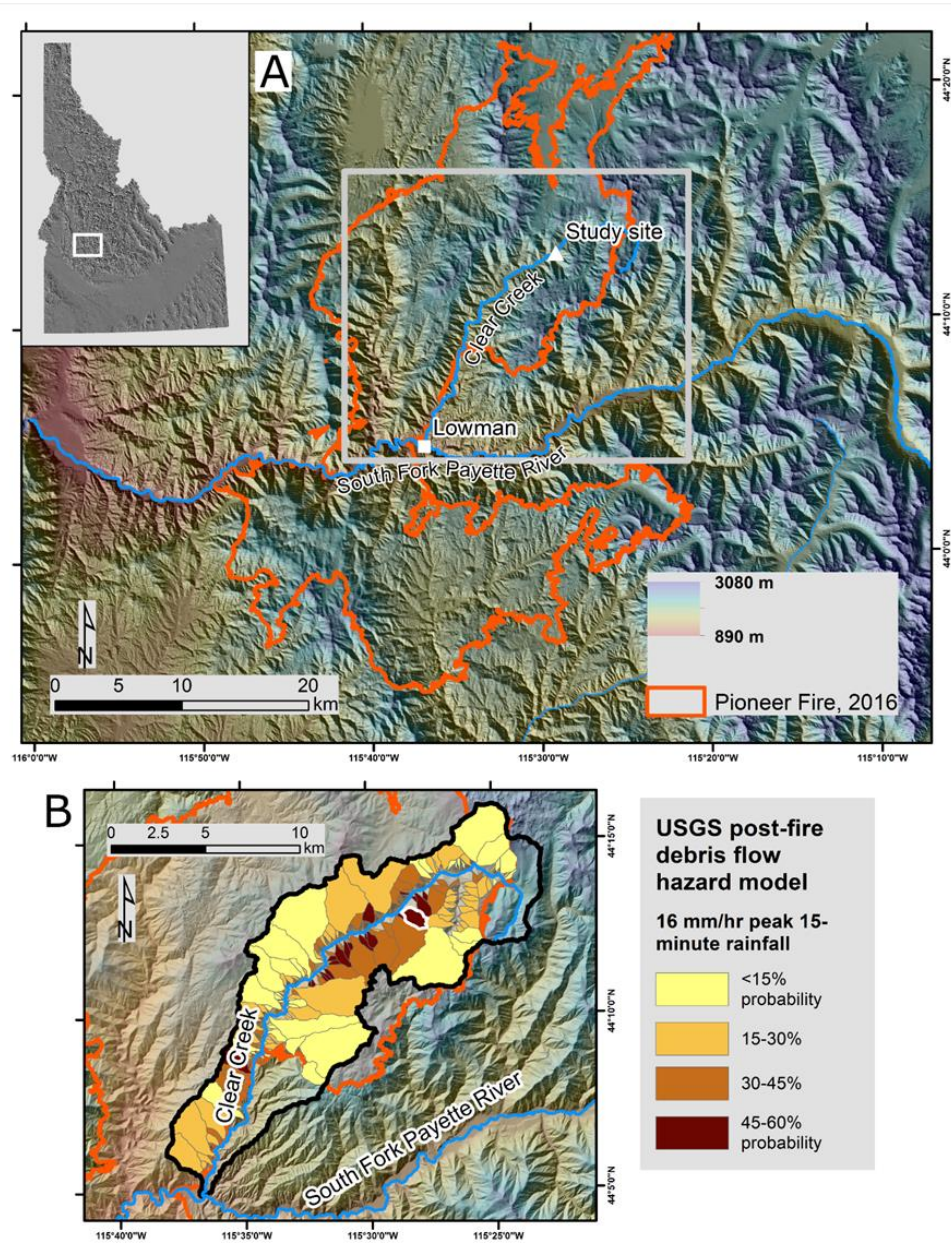


Figure 1.1: A) geographic setting within Idaho, USA. Orange outline is extent of 2016 Pioneer Fire. B) USGS Post-Fire Debris-flow Hazard model results for probability of debris-flow occurrence under 16 mm/hr peak 15-minute precipitation in the Clear Creek watershed. Study catchment is outlined in white.

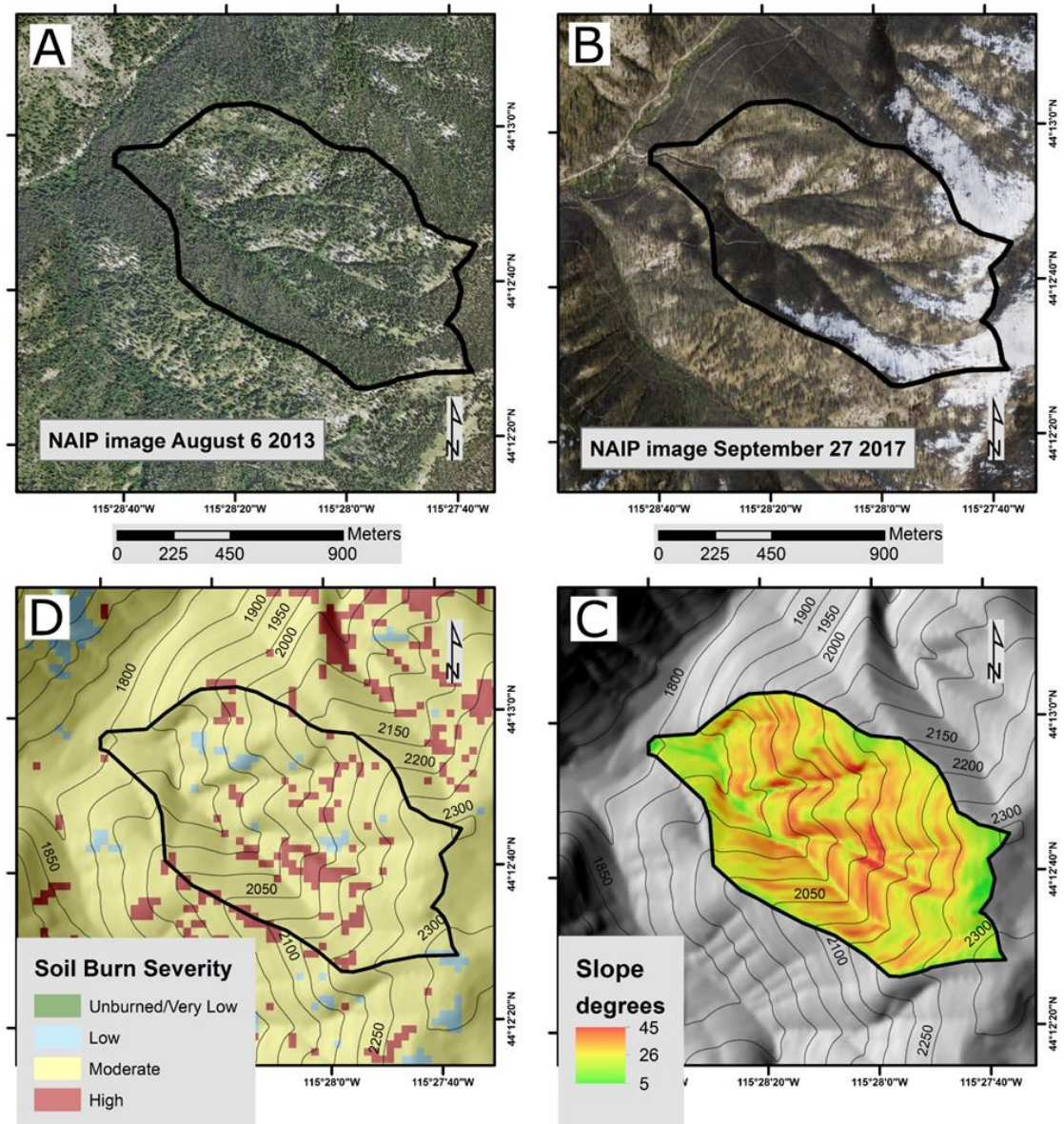


Figure 1.2: A) National Agricultural Image Program (NAIP) image of study site from 2013 (pre-fire). B) NAIP image of study site from 2017 (post-fire and post-debris-flow). C) Slope map of study area. 50 m contours for scale. D) Soil Burn Severity map from USFS Burned Area Emergency Response (BAER). 50 m contours for scale.

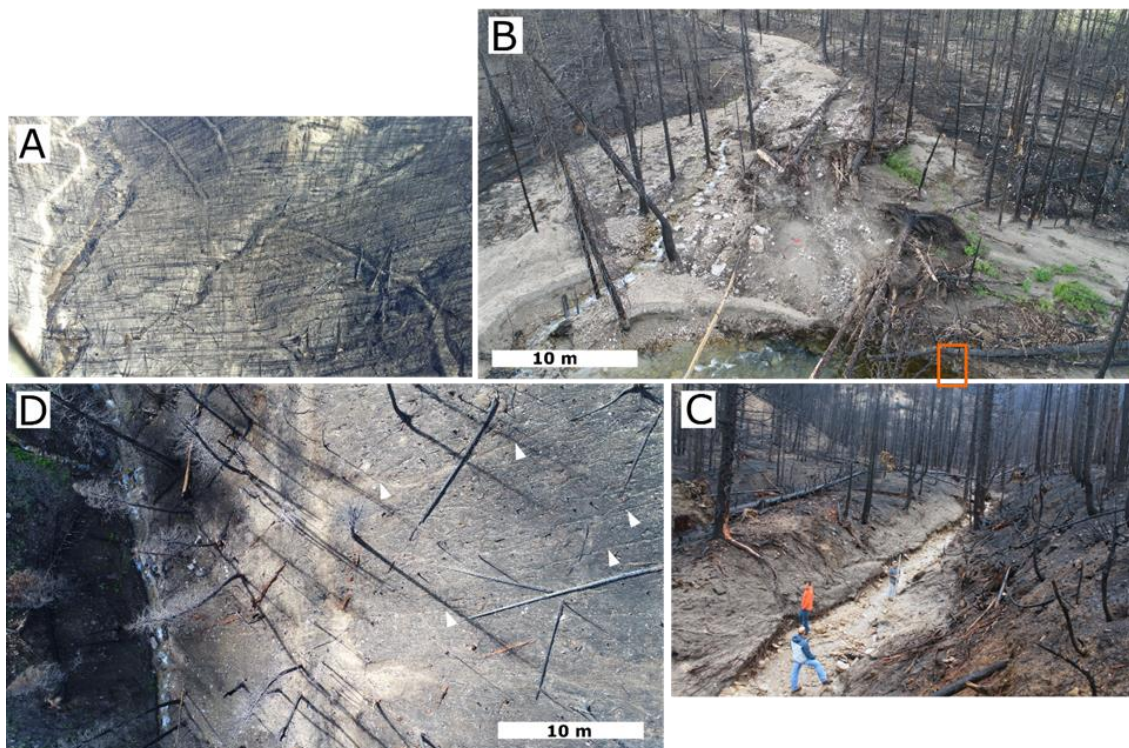


Figure 1.3: A) Image of study catchment outlet post-fire and pre-debris-flow, taken from USFS helicopter. B) UAV image of debris-flow fan deposit. Orange rectangle marks approximate location of described and dated stratigraphy (Fig 4). C) Image of scoured channel from first visit to site, 9 days after debris-flow. Note mud lines, scarred trees and roots, and abrupt channel margins. D) UAV image of rilling on hillslope, arrows highlight individual rills.

Methods

Deposit Stratigraphy, Radiocarbon Ages, and Deposit Volumes

To place the modern debris-flow deposit within a Holocene context we described and dated ~2 m of alluvial fan deposit stratigraphy recording the study catchment history. The described catchment-outlet alluvial fan stratigraphy was exposed along a cutbank by the incision of Clear Creek through the modern and prior fan deposits (Figure 1.4). We radiocarbon dated charcoal fragments from 3 of the 6 described stratigraphic units at the University of Arizona Accelerator Mass Spectrometry Lab. The radiocarbon ages (^{14}C year BP \pm 1-sigma) were converted to calibrated years before present (cal year BP, where

present is 1950) using OxCal v4.3.2 and the IntCal13 atmospheric curve (Reimer et al., 2013). Calibrated age ranges are reported at 95% confidence (2-sigma).

We estimated the deposit volume from the 2016 post-fire debris-flow and compared it to separate measurements of channel debris-flow scour and hillslope rill erosion. The eroded volume methods are described in subsequent sections. We also estimated the volume of previous debris-flow deposits preserved in alluvial fan stratigraphy at the catchment outlet. We estimated the modern deposit volume, including portions removed downstream, using the extent of the deposit mapped from orthorectified UAV images, 12 measured depths where deposits were exposed, and 10 estimated depths where we judged deposition to have occurred but later removed downstream by spring runoff in Clear Creek. We created an interpolated surface from the measured and estimated depths using inverse distance weighting (IDW) with a 0.5 m resolution grid of the mapped deposit extent, then summed the grid cell volumes for a total volume of the modern deposit. IDW was selected for interpolation by visual inspection of the results; it provided deposit depths that were representative of debris-flow and alluvial fan deposition.

We estimated the volume of prior deposits by taking the volume of an oblique pyramid on its side: $\frac{1}{3} b * h$. The base (b) was equal to the deposit length measured along Clear Creek multiplied by the depths associated with radiocarbon ages from the described stratigraphic section. The pyramid's height (h) was equal to the distance from the modern fan's apex to the opposite bank of Clear Creek. We assigned 20% error to our modern and paleo deposit volume estimates (e.g. Meyer et al., 2001; Santi et al., 2008; Moody and Martin, 2009). The volume of a pyramid does not capture the nuances of all

debris-flow dominated fans, but at this site we consider it an acceptable, first order approximation of paleo deposit volumes.

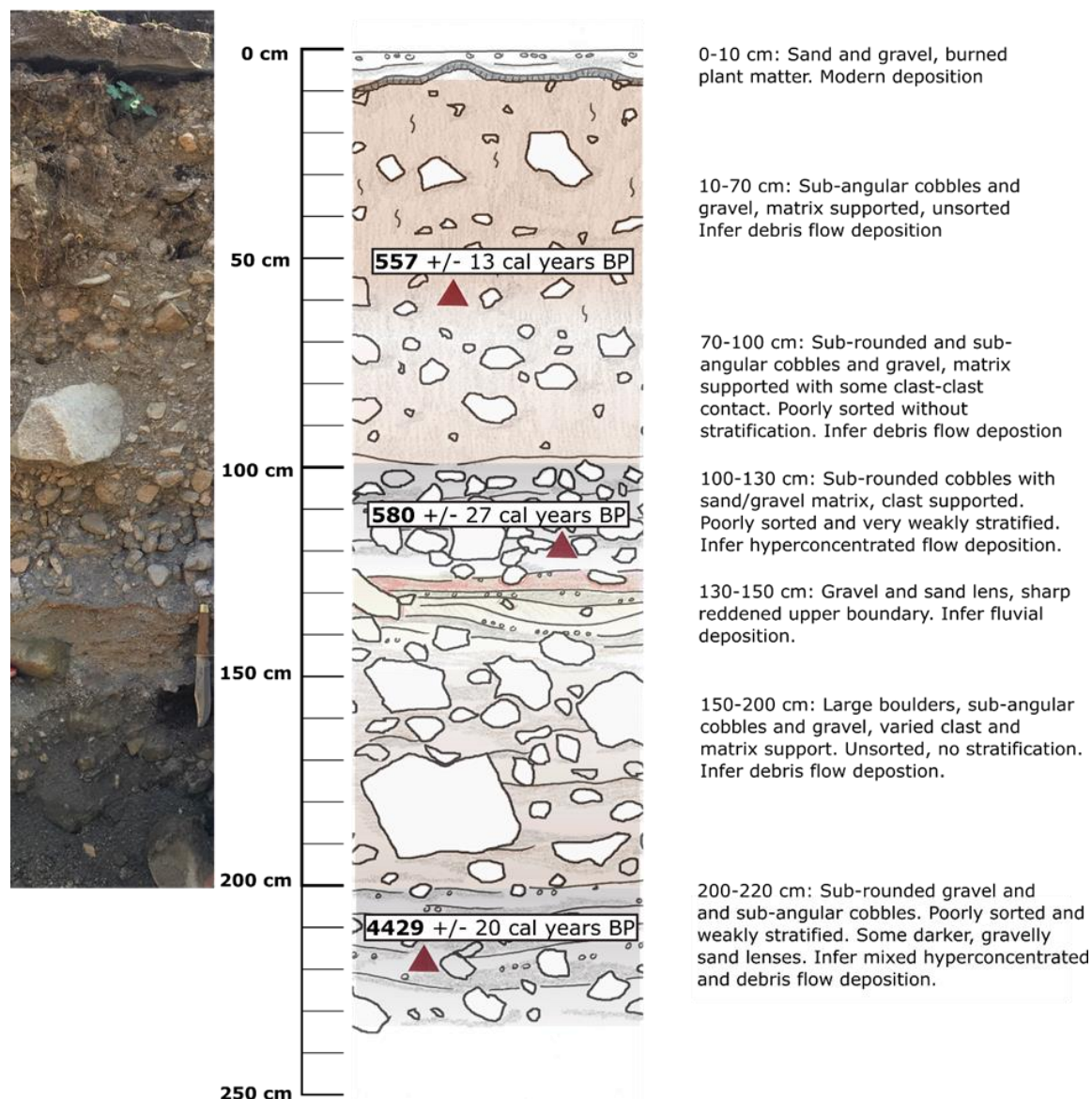


Figure 1.4: Fan deposit stratigraphy. Photo at left is 1 m upstream of described and dated section. At right, thicknesses and descriptions for units. Depths of dated charcoal fragments are shown by red triangles. In the field, we separated depths 10-130 cm into 3 units. Ages suggest they are from a single event. All deposits are fire-related except 130-150 cm depth.

Erosion Rates and Sediment Yields

We converted our deposit volumes to sediment yield (mass/area) and catchment-averaged erosion rate (depth/time) to allow comparisons with other post-fire erosion studies. We determined a catchment-averaged erosion rate (mm/Ka or mm/year) by dividing the deposit volume by the catchment area and the associated age. We propagated the 20% deposit volume error and the calibrated 2-sigma age ranges when calculating the catchment-averaged erosion rates. We converted our deposit volumes to sediment yield, in t/ha, using a bulk density of 1500 kg/m^3 and the catchment area (Kirchner et al., 2001; Meyer et al., 2001). There are potential bulk density changes between eroded material and deposits, so the assumed bulk density of 1500 kg/m^3 should be considered a tool for comparison and not necessarily as an absolute conversion from volume to mass. Furthermore, the erosion rates and sediment yields we calculated represent minimum values because they pertain only to deposits preserved at one site on the alluvial fan.

Hillslopes and Rill Eroded Volume

We did not explicitly measure interrill erosion but noted and observed geomorphic indicators of interrill erosion processes across the study catchment. We also made 20 m transects (n=15) parallel to contours and recorded the number of rills and their widths and depths. Transect locations include a range of slopes (14-37 degrees), aspects (N- and S-facing), and landscape positions (Figure 1.5). When soils were dry we observed a hydrophobic layer (e.g. DeBano, 2000) at the transition between gray, burned soil and unburned, tan mineral soil (~2 cm depth) in several locations, but we did not attempt to determine the spatial variations in soil hydrophobicity.

We used the rill dimensions recorded along hillslope transects and Monte Carlo simulation to quantify the volume of sediment eroded by rilling in the entire catchment. This approach requires two assumptions: 1) our transects sufficiently represent the variability in rilling across the catchment; and 2) the mean rill dimensions and counts come from an underlying normal distribution. Eighty percent of the paired width and depth values from the individual rills (n=175) were randomly sampled in Matlab and the variation in the means were calculated using 1000 Monte Carlo simulations. We also randomly sampled 10 of 15 transects and calculated the variation in mean count (number of rills per 20 m transect) using 1000 Monte Carlo simulations. From these simulations, we calculated a total cross-sectional area eroded by rilling per 20 m transect by multiplying the overall mean rill width and depth by the overall mean rill count. We converted the eroded cross-sectional area to a volume of erosion per transect by assuming 20 m rill lengths, then normalized it to an eroded depth per unit area. Note that the choice of assumed rill length does not affect the depth per unit area. We multiplied the eroded depth per unit area by the total area impacted by rilling to calculate the volume of rill erosion within the entire catchment. We considered the catchment area impacted by rilling to include anywhere within the range of slopes sampled by our transects (14-37 degrees). From this, we removed prominent drainage divides using a 25 m buffer in ArcMap10, consistent with our observations of rill initiation locations in the field. We used the standard deviations in mean width, depth, and counts from the Monte Carlo simulations as uncertainty to calculate upper and lower bounds to the catchment-total rill erosion volume. The rill erosion volume we measured in summer 2017 is primarily from the October 2016 precipitation but may also include minor erosion during snowmelt. We

simplify the measured rill eroded volume by considering it to represent one full year of erosion.

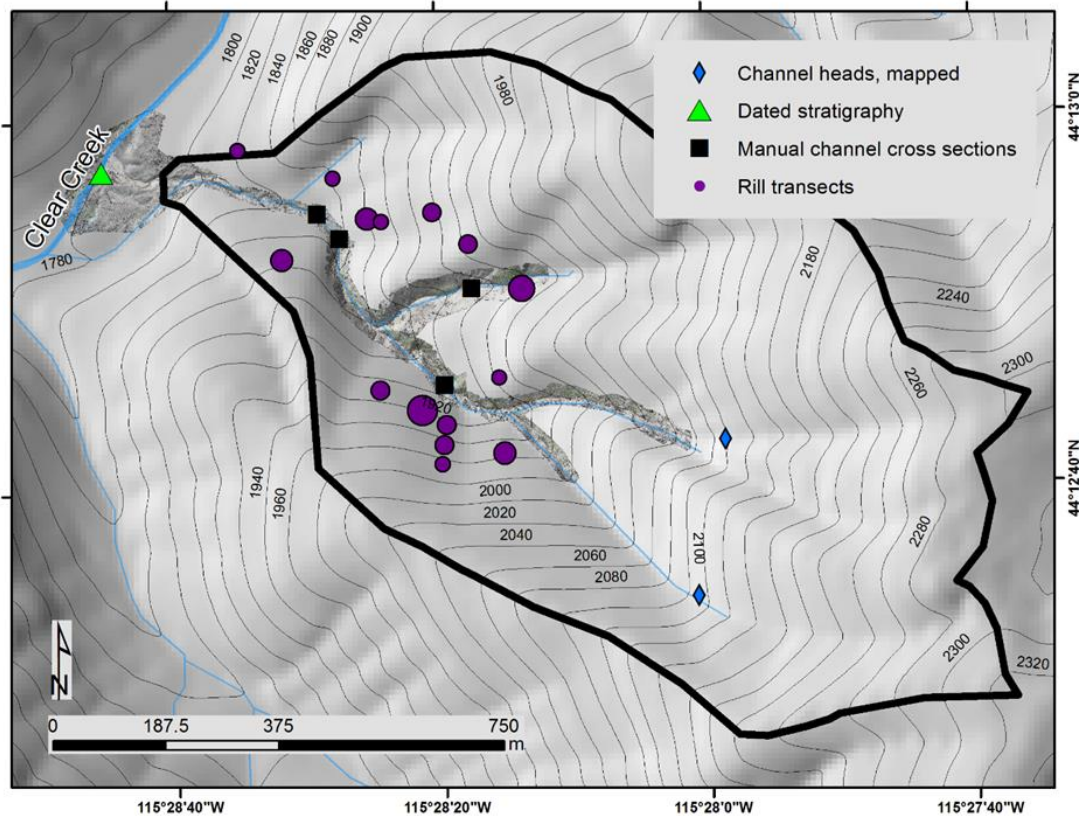


Figure 1.5: Study catchment detail. More detailed hillshade shows extent of SfM-derived 5 cm DEM. Green triangle is location of described and dated stratigraphic section (Fig 4). Black squares are locations of manually-surveyed channel cross-sections. Purple circles are locations of hillslope transects (n=15) scaled by the relative magnitude of rill erosion at each. Transects sample a range of slopes (14-37 degrees) and a variety of landscape positions. Blue diamonds mark channel head locations mapped in the field. 20 m contours shown for scale.

Calculation of Minimum Channel Erosion Volume

To calculate a minimum volume of the channel scoured by the 2016 debris-flow we made cross-sections (n=4) using a tape and stadia rod. The eroded area of each channel cross-section was multiplied by the distance between cross-sections for each section, then summed. We attributed the 20% error for surveyed erosion and deposition

cited by others to this minimum eroded volume (e.g. Meyer et al., 2001; Santi et al., 2008; Moody and Martin, 2009). We also used the manual channel cross-sections to help assess error within the SfM model.

Structure from Motion Methods

While the manual channel cross-sections provide a minimum estimate of channel erosion, we sought to derive more explicit spatial information about the landscape and erosion processes by collecting high-resolution topography. We chose to apply UAV-based SfM to derive cm-resolution topography of the eroded channel in our steep, 1 km² study catchment. After snowmelt in June 2017, we installed rebar (n=20) in stable and distributed hillslope and channel locations to serve as GCPs and recorded their locations with a TopCon HiperV real-time kinematic global positioning system (RTK-GPS). Points were post-processed to 0.01 m accuracy (<https://www.ngs.noaa.gov/OPUS/>, accessed September 2017) (Table 1). Orange bucket lids with centered holes were placed over each GCP rebar to serve as visual targets in UAV imagery. We conducted a total of 6 flights with a DJI Phantom 4 Pro UAV, covering 0.1 km² of the debris-flow fan deposit, the primary channel, and the main tributaries with overlapping 20 megapixel images (Figure 1.6). Camera focus was automatic and focal length was fixed, while image orientations and UAV positions were controlled manually. Images (n=837) were acquired mostly at nadir at flying altitudes ranging from 5-50 m (average 30 m). Some oblique views were included to reduce distortion in the processed point cloud (James and Robson, 2014). We prioritized overcast and early morning flight times to minimize contrast and shadows (James and Robson, 2014; Mosbrucker et al., 2017).

We used Agisoft Photoscan Pro (<http://www.agisoft.com/>) to process the images into a point cloud and assign absolute locations of the GCPs projected to Universal Transverse Mercator Zone 11 North. The raw point cloud had 122 million points, each with an x,y,z position and a r,g,b value. The UAV images, original point cloud, and derived DEM are available on OpenTopography (<http://opentopo.sdsc.edu/dataspace/dataset?opentopoID=OTDS.012019.32611.1>). We used CloudCompare (<https://www.danielgm.net/cc/>) for further analyses of the point cloud and to create DEMs. We cleaned the point cloud by manually removing noise points and those >1 m above the surface. Next, we subsampled the point cloud using 2.5 cm minimum spacing between points (62 million points remaining) and created a 5 cm resolution DEM of the post-erosion topography.

Table 1.1: Summary of ground control points (GCPs), their RTK-GPS accuracy, and Agisoft-processed SfM root-mean-square error (RMSE). The 0.076 m (7.6 cm) total error includes all 20 available GCPs. For our SfM error analysis and volume uncertainty scenario 2 we randomly selected 10 GCPs to serve as control points, calculated the error, and repeated 3 times, resulting in 6.6 cm overall RMSE.

Ground control point name	RTK-GPS horz accuracy (m)	RTK-GPS vert accuracy (m)	GCP accuracy carried into Agisoft (m)	Error (m)	X error (m)	Y error (m)	Z error (m)
102	0.005	0.005	0.005	0.0694	-0.0075	0.0661	0.0198
104	0.005	0.005	0.005	0.1051	0.0668	0.0804	-0.0112
109	0.004	0.006	0.006	0.0080	-0.0031	-0.0013	0.0072
112	0.004	0.007	0.007	0.0848	-0.0752	-0.0267	-0.0287
113	0.004	0.006	0.006	0.1030	0.0794	0.0656	-0.0002
114	0.004	0.007	0.007	0.0947	0.0282	0.0702	-0.0569

119	0.004	0.008	0.008	0.0631	0.0509	0.0040	0.0372
123	0.004	0.005	0.005	0.0034	-0.0026	-0.0021	-0.0004
124	0.004	0.006	0.006	0.0077	0.0072	0.0023	0.0013
125	0.006	0.009	0.009	0.0191	-0.0184	0.0043	0.0029
126	0.004	0.009	0.009	0.0495	0.0169	0.0343	-0.0314
127	0.004	0.009	0.008	0.0201	0.0053	-0.0160	0.0110
128	0.004	0.008	0.008	0.0218	0.0181	0.0110	0.0054
129	0.004	0.008	0.008	0.0320	-0.0172	-0.0244	-0.0117
130	0.004	0.008	0.008	0.0172	-0.0068	0.0121	0.0102
131	0.003	0.006	0.006	0.0856	0.0195	-0.0559	0.0618
132	0.004	0.007	0.007	0.1065	-0.0765	-0.0526	0.0521
133	0.003	0.007	0.007	0.1077	-0.0619	-0.0877	0.0086
134	0.004	0.008	0.008	0.1375	-0.0817	-0.1103	-0.0082
135	0.003	0.007	0.007	0.1225	-0.0388	-0.1014	-0.0567
Total error, m				0.0761	0.0444	0.0544	0.0294
Standard deviation of error, m				0.0440	0.0453	0.0554	0.0302

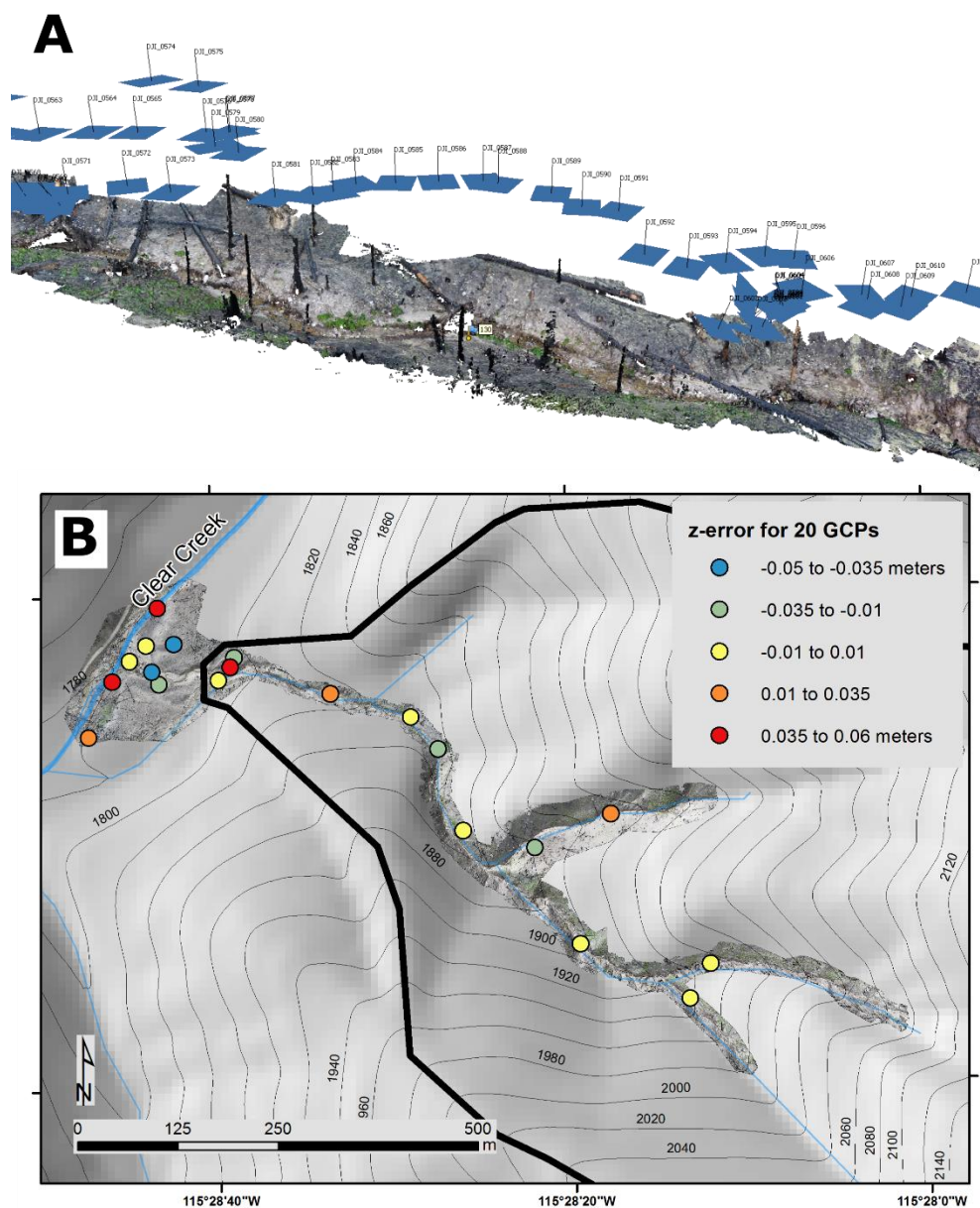


Figure 1.6: SfM methods and error assessment. A) Perspective view of point cloud section. Blue flag represents an RTK-GPS ground control point. Blue squares represent locations and orientations of UAV images. Nadir images were acquired from several altitudes, while some oblique images were collected to minimize distortion (e.g. James and Robson, 2014). Flow is from left to right in the image. B) Vertical RMSE for the processed point cloud compared to 20 RTK-GPS surveyed GCPs. A mix of positive (orange-red) and negative (blue-green) vertical errors indicates little systematic distortion of the analyzed DEM.

High-resolution pre-erosion topographic data was not available for our study site, but we needed a pre-erosion surface upon which to detect change and make calculations of channel eroded volume via a DEM of Difference (DoD) method. We obtained a DEM of the pre-erosion topography by removing the eroded portions and creating a synthetic surface derived from the surveyed, post-erosion point cloud (Figure 1.7A-E). We used the prominent, rectangular signature of debris-flow scour as a guide when removing eroded portions. In CloudCompare, we calculated contour lines at 10 cm intervals to highlight the abrupt scour margins (Figure 1.7B). We used the contours, in conjunction with the color and form of the SfM-derived point cloud, to manually remove scoured points. We fit a surface to the remaining non-scoured points using Delaunay triangulation (Figure 1.7C), enabling us to create a 5 cm resolution DEM of the synthetic, pre-erosion surface. Outside of the scoured channel the synthetic, pre-erosion point cloud and the SfM-derived, post-erosion point cloud are identical.

We created a DEM of Difference (DoD) to measure the volume of sediment eroded from the channel by debris-flow scour. We used Geomorphic Change Detection v7.3 software (Wheaton et al., 2010; <http://gcd.riverscapes.xyz/>) to compute the volume of erosion and incorporate our SfM volume error. All calculations were done using 5 cm resolution DEMs which we ensured were concurrent and orthogonal (Passalacqua et al., 2015). The GCD program incorporates user-specified error surfaces to calculate the DoD and outputs values of erosion or deposition for each grid cell, as well as tabular and graphical summaries. We did not incorporate spatially-variable error estimates (Schaffrath et al., 2015). The pre-erosion surface we created results in a generally flat-bottomed valley and therefore over-estimates the volume of erosion in certain sections.

To account for a more realistic pre-erosion valley bottom we subtracted 25% from our calculated volume. This assumption is simple but subtracting a triangle (25%) from the rectangular channel cross-section mimics a generic pre-erosion valley geometry (Figure 1.7D). Similar approaches have been used (i.e. Meyer et al., 2001; Istanbuluoglu et al., 2003; Gabet and Bookter, 2008; Gartner et al., 2008; Santi et al., 2008; Nyman et al., 2015) when estimating the pre-erosion geometry of gullies. The volume of channel erosion we measured in Summer 2017 is primarily from the October 2016 debris-flow but may also include minor erosion during snowmelt. We simplify the measured channel eroded volume by considering it to represent one full year of erosion.

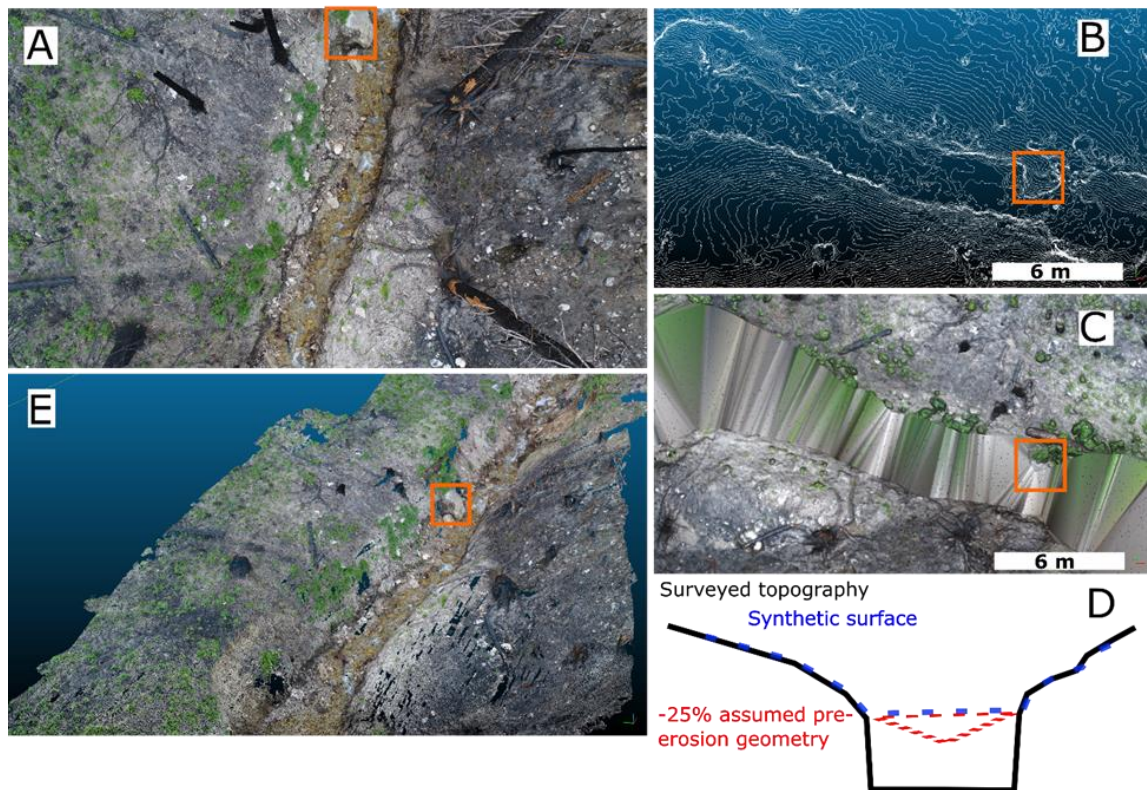


Figure 1.7: A) UAV detail image of channel eroded by debris-flow. Orange boxes are in same location to aid comparison. B) 10 cm contour intervals highlight abrupt channel margin. C) Synthetic, pre-erosion surface created by removing “scour” points. D) Diagram of assumption correcting total calculated volume for a generic, pre-erosion geometry. E) Point cloud perspective view of same channel segment, showing detailed topographic form and appearance of SfM point cloud.

Structure from Motion Error Analysis

We used 2 approaches to assess error within our SfM model. First, we calculated the vertical root mean square error (RMSE) and mean average error (MAE) between manual channel cross-sections (n=4) and corresponding topographic profiles extracted from the point cloud (z-coord only). We ignored measurement error within the manual channel cross-sections. There is also the possibility of slight misalignment of the SfM point cloud coordinates with the local coordinate system used for the manual cross-sections. In our second approach, we considered the maximum error in horizontal (x,y coord) or vertical (z-coord) directions from the post-processed RTK-GPS ground control points and carried these into the SfM model. Using a random number generator, we chose 10 out of the available 20 GCPs to serve as check points. We calculated the RMSE (x,y,z coords) between the RTK-GPS GCP locations and the SfM model GCP locations, then averaged the results of 3 trials. The resulting overall RMSE accounts for both the RTK-GPS error and the SfM model error in all three dimensions.

We used the 2 SfM error assessments to build 3 scenarios for budgeting error when calculating the debris-flow eroded volume by DoD. The error scenarios were implemented in GCD as part of our DEM of Difference calculation. In the first, most conservative scenario, we used a uniform minimum level of detection (LOD) equal to the RMSE calculated between manual cross-sections and the SfM model (16 cm). The resulting error was 19% of the calculated volume. In the second scenario we assigned the overall RMSE (6.6 cm) as the spatially uniform error for the pre-erosion surface and no error (0 cm) for the post-erosion surface. The resulting propagated error was 8% of the calculated volume. We justify this low error because both pre- and post- DEMs are

created from the same SfM model and therefore share the exact same reference system, ground control points, extents, resolution, and accuracy. When comparing other high-resolution topographic datasets (e.g. TLS post- to Airborne Laser Scanning (ALS) pre-), there can be significant uncertainty due to instrument error, georeferencing, and gridding operations (e.g. DeLong et al., 2012). In our situation, the pre-erosion and post-erosion DEMs are derived from the same point cloud and propagating the error from just the pre-erosion DEM is supported. In the final scenario we calculated a probabilistic error budget (0.8 confidence level) using 10 cm spatially uniform error for the surveyed, post-erosion topography and no error (0 cm) for the synthetic, pre-erosion topography. We chose 10 cm to split the difference between the first scenario, which we consider overly-conservative, and the second scenario, which is a minimum representation of error. Using this final scenario, error was 12% of the calculated volume. Based on our analyses we judged this final scenario to be the most suitable error budget and use it for subsequent results and interpretations.

When we returned to the study site in August 2018 low vegetation was re-established across much of the landscape. Significant geomorphic changes were not visually apparent, and we did not observe evidence of extensive erosion since the prior summer. The scoured channel margins were less abrupt, and rills were less distinct or no longer apparent. We conducted two more UAV flights, using an automated flight path to collect 358 images from ~60 m altitude covering 8 of the same RTK-GPS surveyed GCPs. We processed the imagery similarly to the 2017 data into a point cloud with 56 million points. We tried several approaches to filter vegetation points but were not able to

produce a satisfactory ‘bare-earth’ DEM at comparable resolution upon which to detect changes from the 2017 survey.

Results

Channel Erosion

The volume eroded from the channel by debris-flow scour was $3467 \pm 422 \text{ m}^3$ as derived from the DoD approach (Table 2). This represents ~75% of the total measured eroded volume (debris-flow + rills) or ~60% of the estimated deposit volume. The DoD change detection map reveals spatial variations in erosion at 5 cm resolution; the greatest scour depths occur downstream of bedrock knickpoints (Figure 1.8). Mean scour depth was 0.8 m and 77% of scour depths were between 0.25 and 1.5 m. The SfM survey did not extend to channel heads but we visited those locations in the field (Figure 1.5). The rectangular cross-section of the scoured channel persisted during our field work and cut into fresh bedrock in some reaches. We observed debris-flow signatures such as scarred trunks and clasts up to 0.5 m diameter deposited upstream of channel constrictions and obstructions in the upper reaches. We also observed small bank collapses and discontinuous sections of exposed bedrock extending nearly to the channel heads. Using the manual channel cross-sections the minimum volume eroded from the channel was $3300 \pm 660 \text{ m}^3$, or ~5% less than measured by our SfM method.

Table 1.2: Summary of eroded volumes and uncertainties. Values in bold used for analysis and discussion

Method/scenario	Volume eroded (m ³)	Volume uncertainty (m ³)	Volume uncertainty (%)
Channel erosion, manual cross-sections	3300	660	20%
Channel erosion by DoD, scenario 1 (minimum LOD)	3453	655	19%
Channel erosion by DoD, scenario 2 (propagated error)	3485	298	8%
Channel erosion by DoD, scenario 3 (0.8 probabilistic error)	3467	422	12%
Rill erosion by Monte Carlo, lower	811	-	-
Rill erosion by Monte Carlo, mean	1104	320	29%
Rill erosion by Monte Carlo, upper	1425	-	-

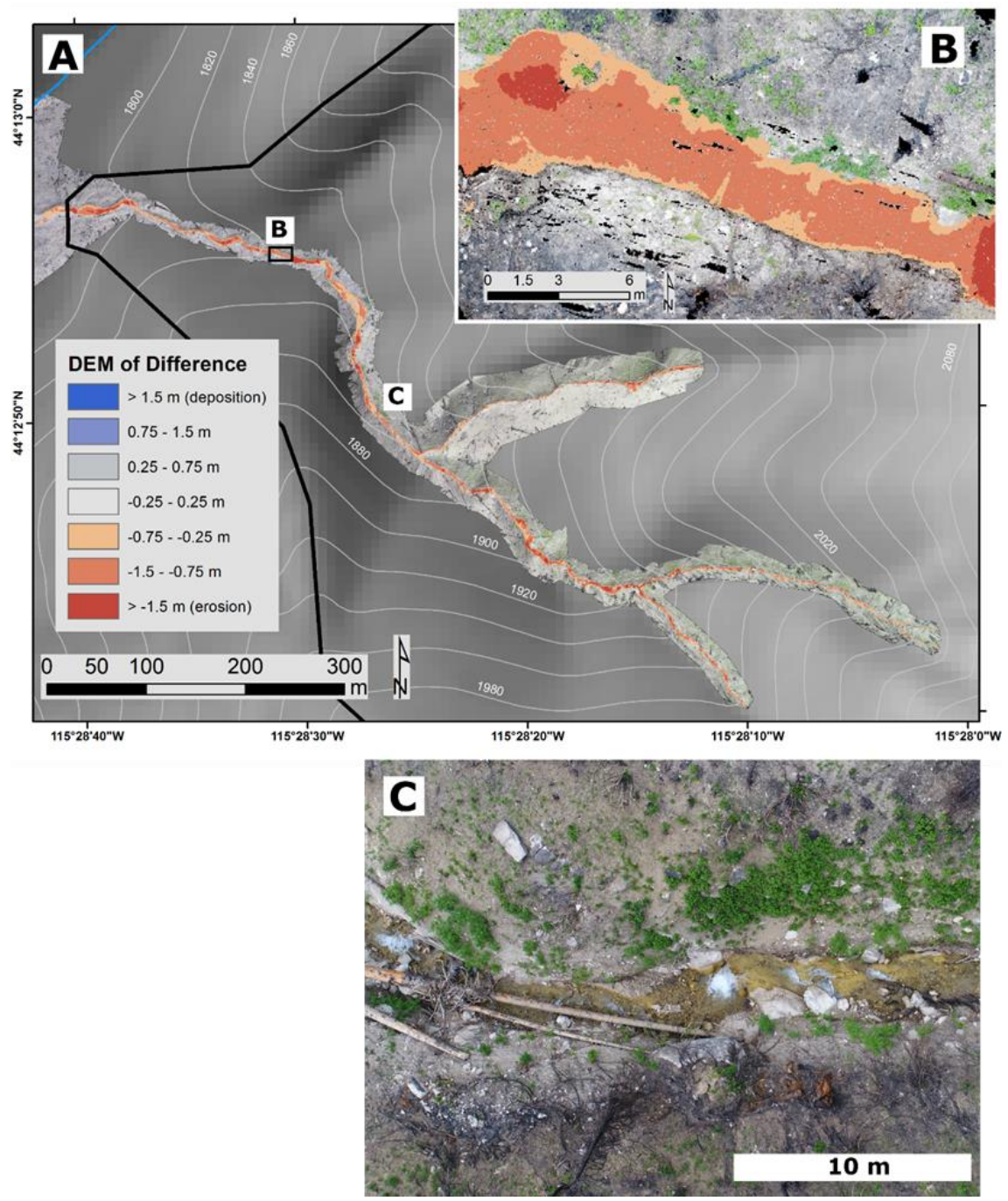


Figure 1.8: A) DEM of Difference for debris-flow channel scour. Red values indicate erosion and blue values indicate deposition. SfM topography extent is shown as hillshade. 20 m contour interval for scale. B) Detail of DoD corresponding to Figure 1.7. C) UAV image of section of channel scoured to bedrock by debris-flow. Flow is from right to left in all panels.

Structure from Motion Error

Both approaches we used to determine SfM error fit closely with previous assessments (Johnson et al., 2014; Lucieer et al., 2014). Mean SfM point cloud RMSE (z-coord) was 0.16 m (MAE 0.03 m) when compared to our manual channel cross-sections. SfM point cloud RMSE (x, y, z coords) was 0.076 m when compared to all 20 available RTK-GPS ground control points (Table 1) and 0.066 m using 3 trials of 10 random GCPs each.

Eroded Volumes from Hillslopes and Rills

Hillslope erosion by surface runoff contributed to debris-flow generation. We observed evidence of hillslope erosion by multiple processes. Curved flakes were spalled from granite outcrops and boulders. Burn marks on rocks (e.g. Smith et al., 2012) and pedestals below rootlets and small rocks (e.g. Nyman et al., 2011) indicated overland flow and raindrop impact had removed hillslope material (e.g. Kinnell, 2005). Overall, less ash was present on surfaces than during our first visit. The depth of material removed was <2 cm in most locations we observed, inferred to be a mixture of ash and mineral particles. We did not explicitly quantify erosion by interrill processes on hillslopes. Rilling throughout the catchment extended to within a few tens of meters of the drainage divides. Rill widths and depths were mostly cm- to dm-scale. Rill lengths were 10 - 100 m and often discontinuous. Burned-out roots were common and provided significant conduits into the subsurface. Finer-grained regolith occurred on north aspect hillslopes along with more distinct and more numerous rills. Transects sampled a range of slopes (14-37 degrees) and recorded significant variability in rill count and rill dimensions

(Figure 1.9). The rill dimension measurements and counts along our transects were not significantly correlated with slope or contributing area.

Hillslope erosion by rilling produced ~20% of the estimated total deposit volume. The volume of rill erosion within the entire study catchment was $1100 \pm 320 \text{ m}^3$ (29% uncertainty) by our Monte Carlo method, shown in Figure 1.9 and summarized in Table 2. Our rill eroded volume calculation is based on the catchment area represented by the range of slopes captured by our hillslope transects and excludes regions near drainage divides. Rilling impacted >80% of the catchment (770,000 of 955,000 m^2) with an average erosion depth of 1.4 mm/m^2 . We directly measured rill erosion and we use that magnitude in our discussion but recognize that our measured rill erosion represents a minimum value for hillslope erosion (rill + interrill processes). We note that concurrent interrill erosion does not impact the erosion magnitudes for the channel and rills that we did measure, nor does it increase the error associated with our catchment totals.

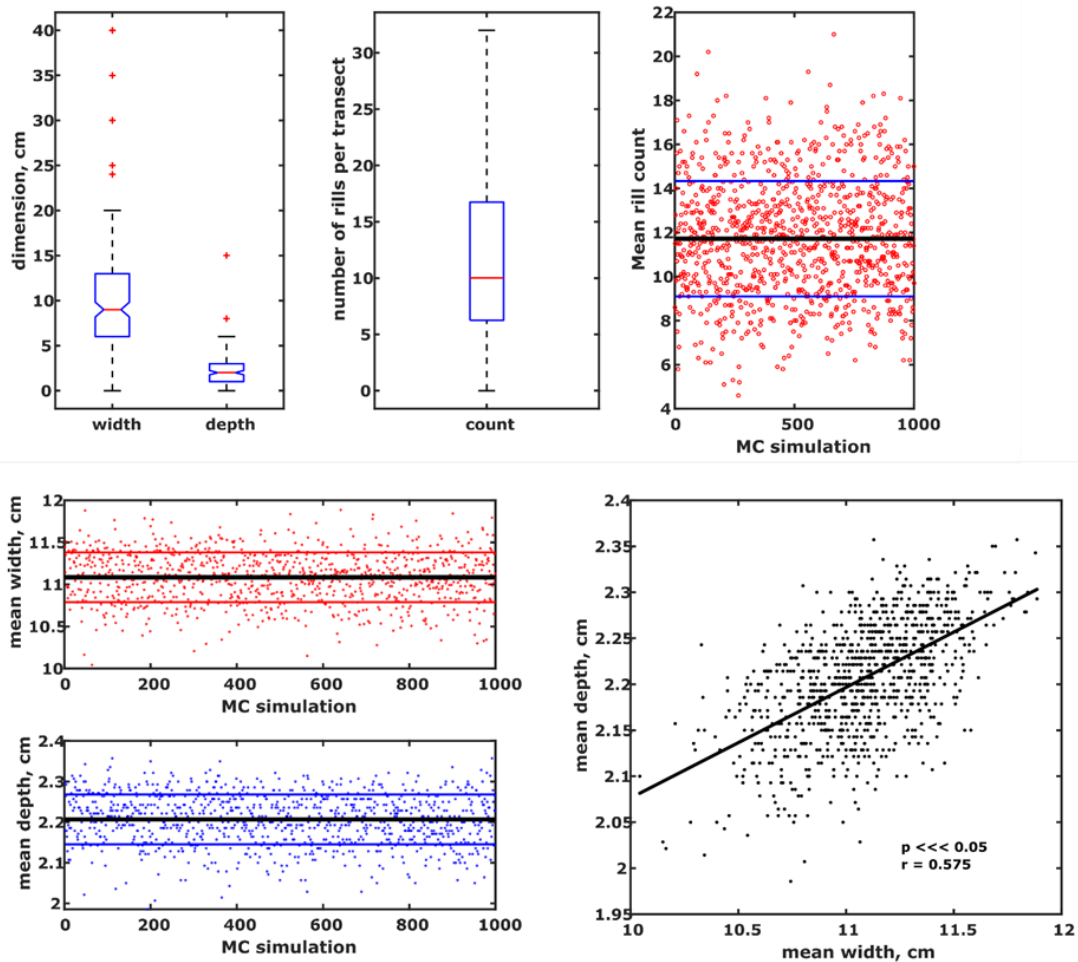


Figure 1.9: Upper left, Boxplots of rill dimensions from full dataset ($n=175$) and rill counts per transect ($n=15$). Upper right, Monte Carlo simulation results showing variation in mean rill count per transect. Lower left, Monte Carlo simulation results showing variation in mean rill width (red) and depth (blue) dimensions. Lower right, Mean rill depth plotted against mean rill width, with linear best fit shown, note x and y axis scales.

Deposit Stratigraphy, Radiocarbon Ages, and Deposit Volumes

Alluvial fan stratigraphic sequences at the study site outlet preserve ~4.5 Ka of fire-related deposition. At our sampling site where the stratigraphy was best exposed, we split the stratigraphic exposure into six units based on sedimentary characteristics and inferred depositional processes (Figure 1.4) and three dated charcoal fragments (Table 3). Samples 4-2 and 4-4 likely record the same fire-related debris-flow event at ~560 cal yr BP. Taken together with the stratigraphy and estimated deposit volumes, these ages indicate three significant fire-related debris-flow events every ~5 Ka and a recurrence interval (of deposition, not fire) of ~1.6 Ka. We acknowledge that there are likely depositional events preserved elsewhere on the alluvial fan that are not represented by our ages from the described stratigraphic section.

Individually, all three deposits have very similar magnitudes. The volume of the modern deposit was $5716 \pm 1143 \text{ m}^3$ using interpolated depths (Table 3). The inferred volumes of the ~560 cal year BP and ~4420 cal year BP deposits are ~6,300 and ~10,000 m^3 , respectively. We determined the volume of the 2 prior units based on the depths of dated charcoal samples and the stratigraphic descriptions. When calculating erosion rates and sediment yields, we considered the deposit volumes to include overlying deposits (e.g. volume of ~4420 cal BP deposit includes ~560 cal BP and modern deposits). This averages the deposition of sediment over longer timescales and provides a better representation of the overall erosional response of this basin to fire since the mid-Holocene.

Table 1.3: Radiocarbon dates from charcoal fragments preserved in stratigraphy at study catchment outlet.

Sample name (lab sample number)	Sample depth (m)	14C age, year BP (1-sigma)	Calibrated age, year BP (2-sigma)
4-2 (X32824)	0.6	601 (18)	557 (13)
4-4 (X32826)	1.2	628 (19)	580 (27)
4-6 (X32825)	2.2	3970 (21)	4429 (20)

Erosion Rates and Sediment Yields

The catchment-averaged erosion from the 2016 event is similar to the overall erosion rate since the mid-Holocene at this site (Table 4). The catchment-averaged erosion magnitude for the 2016 event was 6 mm (± 1 mm) while the erosion rate since ~4420 cal year BP has been 5 (± 1) mm/Ka. The increased sediment yield and erosion rate over the last 600 years reflects two debris-flow events and are therefore higher than the 4.5 Ka average. We consider the erosion and sediment yield in the year following fire to be equivalent to the measured October 2016 event magnitudes for our discussion. When partitioned by process, modern debris-flow channel scour contributed 55 t/ha sediment yield or 3.7 mm of catchment-averaged erosion, while hillslope rilling alone contributed 17 t/ha or 1.2 mm of catchment-averaged erosion. The erosion rates and sediment yields we calculated represent minimum values because they do not include erosion that occurred but was not preserved in the stratigraphic record (e.g. material carried by streamflow into Clear Creek), or erosion that occurred but we did not directly measure (interrill magnitude).

Table 1.4: Estimated deposit volumes and conversions to catchment-averaged sediment yield and erosion rate. The deposit volumes represent single events based on stratigraphy and radiocarbon ages. The sediment yield and erosion rate are calculate including overlying deposits to represent longer-term averages.

Deposit age	Volume, m ³ (uncertainty)	Catchment-averaged sediment yield, t/ha/Ka (range)	Catchment-averaged erosion, mm/Ka (range)
modern (*1-year)	5716 (1143)	*90 (17)	*6 (1)
~560 cal year BP	6300 (1260)	336 (80)	22 (6)
~4420 cal year BP	10000 (2000)	78 (16)	5 (1)

Discussion

Precipitation Characterization and Context for Debris-flow Prediction

Local specific forcing data and detailed pre- and post-erosion topography are desirable to link precipitation to erosion processes (e.g. DeLong et al., 2018). However, in a large fire with high erosion potential in many basins, the allocation of equipment and focus must be balanced with access and hazards. While it is possible to single out small areas where post-fire erosion is anticipated, catchments will not produce debris-flows after every fire, as evidenced by this site’s charcoal record and by the absence of other debris-flows within the Clear Creek drainage. We lack local, high temporal resolution precipitation data and we were not able to acquire pre-erosion topography; a common and realistic situation. We took advantage of debris-flow occurrence in this representative catchment by using the rich topographic information provided by SfM to investigate our research questions.

We did not co-locate a rain gauge or other remote monitoring equipment at our study site. The precise, peak 15-minute intensity of the debris-flow triggering rainfall is

unknown, but from available hourly (~10mm/hr) and daily (~25 mm/24 hours) data we characterize the mesoscale precipitation from the October 2016 frontal storm as modest. That said, precipitation in mountainous areas can be highly spatially variable (e.g. Bales et al., 2006; Stratton et al., 2009), and given that this particular basin failed and adjacent similar basins did not, one possibility is this basin received higher rainfall. Brogan et al. (2017) report an environment where mesoscale precipitation resulted in greater geomorphic change than convective precipitation via fluvial processes. However, Benavides-Solorio and Macdonald (2005) found that convective storms produce >90% of hillslope plot erosion, and Kampf et al. (2016) found average sediment yields doubled in convective versus mesoscale storms. Hillslope erosion processes vary with precipitation intensities (McGuire et al., 2016), but linking the contribution of each hillslope process to debris-flows generated by runoff under a wider range of conditions remains an important topic. The October 2016 debris-flow triggered by modest rainfall at our study site serves as a reminder that post-fire hazards are not limited to especially high-intensity convective precipitation.

We used the USGS post-fire debris-flow hazard model to provide additional context for our results. Using our estimated 2016 deposit volume (5700 m^3) as a parameter, the peak 15-minute precipitation intensity predicted by the USGS model is ~13.5 mm/hr. The model predicts a 50% likelihood of debris-flow occurrence in our study basin under ~17 mm/hr peak 15-minute rainfall and predicts a volume of 6695 m^3 (~17% greater than 2016 deposit volume). The total eroded volume we measured ($4600 \pm 740 \text{ m}^3$) and total deposited volume that we estimated ($5700 \pm 1140 \text{ m}^3$) fit the USGS model predictions moderately well considering the model's intended use and our

uncertainties. Further, the USGS model allows some quantitative characterization of the October 2016 event-triggering rainfall. At 16 mm/hr peak 15-minute rainfall (one of the design storm intensities used for preliminary assessment), the USGS model predicts 18 basins in the Clear Creek drainage to have higher probabilities of debris-flow occurrence than our study catchment. To date, ours is the only catchment in the Clear Creek basin that has produced a debris-flow. Eighty-five percent of runoff-generated debris-flows occur in the 1st year after fire, diminishing the likelihood of more debris-flows in the Clear Creek basin (Degraff et al., 2015). We infer that debris-flow occurrence in our study catchment reflects factors not entirely captured by the current USGS post-fire debris-flow hazard model because many other nearby basins had equal or higher probabilities but did not produce debris-flows under widespread but modest precipitation in October 2016. The study catchment produced a debris-flow ~600 years ago, so perhaps the time since the last channel-evacuating debris-flow, and accumulation of sediment on hillslopes and channels modifies the post-fire hazard in this setting.

Structure from Motion: Accuracy, Advantages, and Recommendations

There are a host of studies addressing the accuracy and precision of SfM, generally through comparison with TLS, ALS, or GPS reference data. Both approaches we used to quantify SfM error fit closely with prior work assessing SfM accuracy. Our overall SfM error as assessed against 20 RTK-GPS surveyed GCPs was 6.6 cm; very similar to Lucieer et al. (2014) who found 6 cm vertical error using a denser network of 39 RTK-GPS surveyed GCPs on a landslide in Tasmania. Other studies that assess SfM error using GPS report RMSE of 5-10 cm (Tamminga et al., 2015), a few decimeters (Javernick et al., 2014), and 5-13 cm (Smith et al., 2014). Several studies have compared

SfM data to TLS data as a reference and found 2-20 cm error (Cook, 2017; Johnson et al., 2014; Stumpf et al., 2015). Johnson et al. (2014) also compared SfM to ALS data as a reference and found error was <13 cm for 90% of points. Gillan et al. (2017) compared UAV-derived SfM measurements to manual erosion bridge measurements along topographic transects and calculated an RMSE of ~3 cm. Clapuyt et al. (2016) tested the reproducibility of SfM topographic datasets and found 6 cm MAE within their workflow. Our assessment of SfM error (16 cm using manual channel cross sections, 6.6 cm using RTK-GPS surveyed GCPs) fits closely with these studies and show that SfM is a viable, accurate method to quantify post-fire erosion volumes.

Continued work on georeferencing accuracy is critical to improving change detection using ultra-high resolution topography (e.g. Passalacqua et al., 2015; DeLong et al., 2018). Our results show that low error (6.6 cm) and very high spatial resolution (5 cm DEM) are possible when sub-centimeter RTK-GPS ground control is integrated into SfM surveys, even in a steep and challenging landscape. However, current SfM georeferencing accuracies are not adequate to detect changes of a few centimeters (i.e. rilling) continuously over a ~1 km² catchment using change detection techniques. Eltner et al. (2015) and Morgan et al. (2016) applied SfM to small hillslope plots and laboratory flumes, respectively, showing its promise for sub-cm level measurements. Glendell et al. (2017) used the iterative closest point (ICP) method to compare multi-temporal SfM models of upland features in England, but this approach is not appropriate where landscape change is widespread and where there are multiple best-fits for the ICP algorithm. SfM depends on image information, so variable lighting and image locations (among other factors) influence the resulting SfM model, even with well-constrained

GCP locations (Clapuyt et al., 2016). Regularizing UAV flight paths and image locations, as Goetz et al. (2018) have done, is an important methodological consideration for future change detection via SfM.

The ease of acquiring cm-resolution topography via UAV and SfM provided a logistic advantage over TLS at our study site. A comparable TLS point cloud extent would require many scan locations to accommodate the rugged topography and occlusion from standing burned trees. The orange bucket lids over rebar GCPs worked well for visibility in UAV imagery and in the field. In such a steep, rugged study site, setting up the GCP network and recording it with RTK-GPS took longer than executing the UAV flights. The directly georeferenced UAV-SfM options becoming available would have an advantage in particularly high-relief study sites (Carbonneau and Dietrich, 2017; Turner et al., 2014).

The regrowth of vegetation was significant 2 years post-fire, reducing the occurrence and magnitude of further erosion (i.e. Orem and Pelletier, 2015; Wagenbrenner and Robichaud, 2014). Additionally, the spatial coverage of new vegetation on the landscape precludes the use of SfM to derive cm-resolution topographic models for change detection. We were not able to produce a satisfactory “bare earth” model from 2018 at an equivalent resolution as the 2017 survey. The limitations of SfM, namely vegetation and georeferencing, must be considered when applied to geomorphic change detection.

Post-Fire Erosion Processes

The debris-flow scoured the channel to bedrock in multiple places, proving an effective tool for long-term geologic erosion and landscape denudation (Stock and

Dietrich, 2006). We did not observe any large colluvial failures as expected in a debris-flow triggered by saturation failure (i.e. Costa, 1984; Stock and Dietrich, 2006). Instead, widespread rilling and inferred extensive overland flow led to a runoff-generated debris-flow (e.g. Meyer and Wells, 1997; Cannon et al., 2001; Gabet and Bookter, 2008). As Kean et al. (2013) and Rengers et al. (2017) show, runoff-generated debris-flow initiation often requires sediment to be introduced to the channel, temporarily stored, and then fail. It was difficult to pinpoint specific initiation points in the field, but markers representative of debris-flows including small levees, inset deposits of large-caliber clasts, and scarred vegetation were present throughout the SfM-surveyed channel sections and >75% of the distance to channel heads. Widespread hillslope rilling, and inferred interrill erosion, provided the in-channel sediment necessary for debris-flow initiation.

In this setting, rilling contributed about 25% of the total measured erosion. Rill widths were more variable than rill depths and rills were twice as common on north aspects (Figure 1.10). Rills are transient and difficult to measure across continuous spatial extents. Our method addresses that by using a limited number of representative hillslope transects, randomly sampled and repeated many times with Monte Carlo simulation. We make two assumptions: 1) our transects adequately sampled the variability in rilling within the catchment, and 2) the sample means come from an underlying normal distribution, permitting us to use the standard deviations as uncertainty. An effort was made to sample a variety of locations and sample means often approach a normal distribution by the central limit theorem, thereby satisfying both assumptions. The range in sample mean rill width, depth, and number is much smaller than the range in all rill data, and subsequently provides a better constrained estimate of total rill erosion volume.

The range in sample means also defines the 29% volume uncertainty in our approach; a clear advantage over prior work that does not report uncertainty. Finally, Monte Carlo simulation highlights the difference between rilling on north and south aspects (Figure 1.10). Fitch and Meyer (2016) found north-facing basins experienced more post-fire erosion in the late-Holocene based on analyses of alluvial fan stratigraphy in the Jemez Mountains, but they do not split it into specific process differences. While not statistically significant, the north-facing aspects exhibit more numerous rills with smaller dimensions than the south-facing aspects. We attribute this difference to generally finer-grained regolith on north aspects as noted in the field, but further exploration is warranted. Rilling was not significantly correlated with slope, perhaps an effect of only making 15 transects and extracting their slopes from 10 m resolution elevation data. Moody and Martin (2009) report an “inability to link slopes to actual erosion sites” and did not correlate sediment yield with slope. Similarly, Perreault et al. (2017) found no strong correlations between terrain attributes (such as slope) and diffusive hillslope erosion and suggested that stochasticity may obscure predicted relationships.

Other indicators of interrill hillslope erosion processes were observed but not directly measured. These included raindrop induced impact and shallow overland flow (e.g. Kinnell, 2005) evidenced by burn marks on rocks, pedestals below rootlets, and pebble surface lag. Significant dry ravel or sediment wedges released by vegetation loss did not occur at our study site, contrasting with the supply-limited system of Dibiase and Lamb (2013). There was no occurrence of levee-lined “hillslope debris-flows” (Langhans et al., 2017).

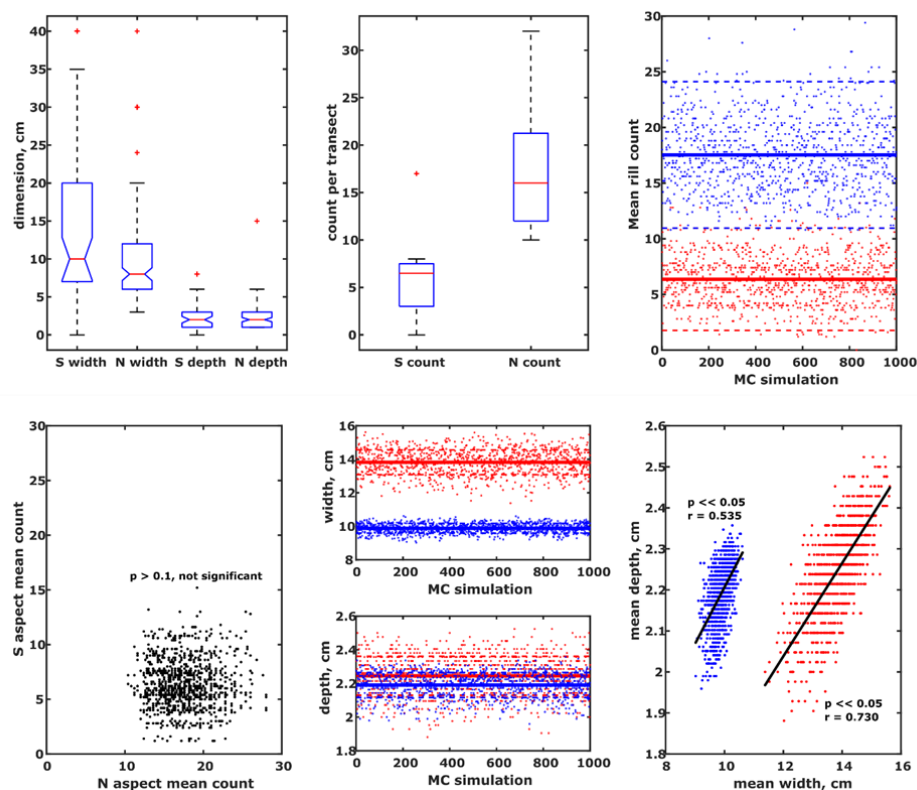


Figure 1.10: Upper left, Boxplots of rill dimensions separated by aspect, and boxplots of mean rill count per transect separated by aspect. Upper right: Monte Carlo results showing variation in mean rill counts on north aspects (blue) and South aspects (red). Lower left, S aspect mean rill counts plotted against N aspect mean rill counts, note x and y axis scales. While not statistically significant, north aspects had about three times as many rills as South aspects. Lower middle, Monte Carlo results showing variation in rill width and depth, separated by north aspect (blue) and South aspect (red). Lower right: Mean rill depth plotted against mean rill width, separated by north aspect (blue) and South aspect (red). Linear best fits shown in black, note x and y axis scales.

Partitioning of Erosion Processes

Our hillslope versus channel erosion partitions fall within literature values (Figure 1.11). We found 75% of total erosion came from debris-flow scour in the channel, while hillslope erosion from rilling alone produced about 25% of the total measured eroded volume. In a setting fairly similar to our own, Meyer and Wells (1997) recorded 70% of total eroded volume from channels and 30% from rilling. However, Santi et al. (2008) report only 3% of total eroded volume from rilling in 46 debris-flow producing basins. In

their review, Moody and Martin (2009) report a factor of 3 greater sediment eroded from channels than from hillslopes in the year following fire (240 t/ha vs 82 t/ha). Conversely, multiple TLS studies show hillslope erosion exceeds channel erosion (DeLong et al., 2018; Rengers et al., 2016; Staley et al., 2014). Rengers et al. (2016) found erosion from hillslopes was 3 times greater than from convergent, incipient channels at a 0.55 ha study site in Colorado. Staley et al. (2014) determined ~80% of total erosion came from hillslopes with contributing areas <40 m² in Southern California. In Arizona, overland flow and rilling produced 68% of total post-fire erosion while channels produced 32% (DeLong et al., 2018). Nyman et al. (2015) calculated ~50% of total erosion was contributed from hillslopes using average depths of erosion from quadrats and transects in two burned, ~0.5 km² basins in Australia. At the same sites, Smith et al. (2012) reported 22-74% hillslope contribution to total erosion using radionuclide tracers in debris-flow deposits. This range of values for channel versus hillslope contributions to total post-fire erosion is not surprising given the variety of geologic settings, rainfall regimes, and basin characteristics. Additionally, each study uses different methods; where the TLS studies focus on small areas of relatively large change and the channel survey methods likely underestimate hillslope components (DeLong et al., 2018). The partitioning of erosion processes in our 1 km² study catchment (75% channel, 25% rilling) provides additional information on how drainage area influences erosion process-dominance. In the small catchments (a few hectares) examined using cm-resolution TLS data by Staley et al. (2014), Rengers et al. (2015), and DeLong et al. (2018), hillslope processes dominate total erosion primarily because the drainage areas are small. On the other hand, the compiled values from Moody and Martin (2009) include a range of larger

drainage areas (a few sq km) and subsequently channel erosion processes dominate total erosion. Other studies have examined relationships between drainage area and erosional processes (e.g. Montgomery and Foufoula-Georgiou, 1993; Moody and Kinner, 2006; Reneau et al., 2007; Scott et al., 1998; Stock and Dietrich, 2006; Wagenbrenner and Robichaud, 2014). However, more work is needed to 1) examine how fire alters relationships between erosional processes and drainage area, and 2) integrate high-resolution topography into a wider range of drainage areas.

Our measured volume of erosion (debris-flow + rills) was $\sim 4600 (\pm 740) \text{ m}^3$ while our estimated deposit volume was $5700 (\pm 1140) \text{ m}^3$. The eroded and deposited volumes overlap within error. However, we noted widespread evidence of interrill hillslope erosion. Several possibilities exist: 1) “missing” portion of deposit volume ($\sim 1100 \text{ m}^3$, or $\sim 20\%$ of total deposit) represents erosion by rainsplash, overland flow, and other interrill hillslope processes, 2) fine-grained material removed by interrill processes was carried downstream and not preserved in deposit, 3) material removed was mostly organic matter or ash rather than mineral clasts, 4) Potential bulk density differences between eroded and deposited material preclude the total eroded volume from equaling the total deposited volume. Considering our observations of interrill processes the first possibility is very likely but we cannot accurately quantify the extent or magnitude of interrill erosion across a 1 km^2 catchment given current measurement uncertainties and the other possibilities mentioned.

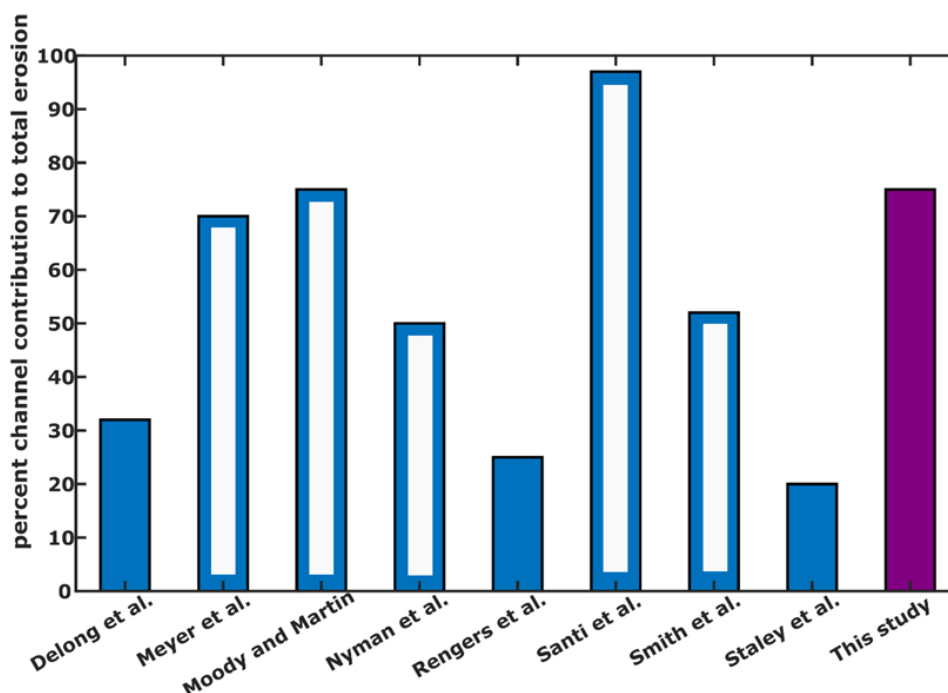


Figure 1.11: Comparison of post-fire studies reporting contribution from channel erosion processes to total erosion. Channel processes include debris-flow, hyperconcentrated flow, and streamflow. Solid columns are from high-resolution topography and single catchments. Hollow columns are from other methods or averages from multiple catchments. Catchment sizes are 0.075 km² (DeLong), 0.5 km² (Meyer), various (Moody and Martin), 0.1-2.2 km² (Nyman), 0.005 km² (Rengers), 0.5-5 km² (Santi), 0.07-0.2 km² (Smith), 0.01 km² (Staley), and 0.95 km² (this study).

Modern and Holocene Erosion Rate and Sediment Yield Comparison

Our basin produced a total sediment yield of 90 t/ha (from estimated deposit volume) in the first year after fire; 17 t/ha (from measured rill volume) came from rilling alone. Meyer et al. (2001) describe two nearby, ~0.5 km² basins (one unburned) that produced 4 times greater sediment yields (~420 t/ha) resulting from 7 cm of rain on rapidly-melting snowpack, contrasting with the more modest precipitation that drove erosion at our study site. In the Middle Fork Salmon River watershed, Riley (2012) shows sediment yields of 1.8-740 t/ha from several burned, debris-flow producing basins.

Sediment yields from hillslope erosion on burned plots in Colorado are 10-12 t/ha per year (Benavides-Solorio and MacDonald, 2005; Schmeer et al., 2018). The average value for post-fire hillslope erosion across the Western US is 82 t/ha/year (Moody and Martin, 2009). In a coarse-scale modeling study, Miller et al. (2011) predict 2 t/ha/year for hillslope erosion in the intermountain West; more than 7 times less than what we measured with rilling alone. Using the ~35,000 km² Salmon River basin in Idaho as their domain, Gould et al. (2016) model an increase of 31 t/ha/year sediment yield under future climate scenarios linked to increases in fire frequency and severity. However, neither study includes mass wasting processes (debris-flows) in their models, which integrate over large watersheds and dominate the sediment yield and erosion rate over Ka timescales (Kirchner et al., 2001).

A 4500-year record of fire-related erosion at our study site is preserved in fan stratigraphy (Figure 1.4). Attributing a percentage of erosion to fire is complicated by potential reworking or removal of older deposits by Clear Creek, but 90% of deposition is fire-related (2.0 of 2.2 m) using the available stratigraphy. Over the last 4.5 Ka, three significant events deposited ~6-10,000 m³ each. These similar magnitudes are logically controlled by basin size, morphology, and bedrock composition, among other quasi-static factors. The debris-flow magnitudes are perhaps also influenced by sediment availability via weathering and soil production (e.g. Heimsath et al., 1997; Dibiase and Lamb, 2013; Eppes and Keanini, 2017), vegetation and climate changes (e.g. Pierce et al., 2004, 2011), and other factors varying over Ka timescales. Schumm's (1973) concept of complex response and geomorphic thresholds modifies these static and varying factors. Parsing out

the role of each would require information on debris-flow magnitudes from a wider range of spatial and temporal settings.

We calculated $78 (\pm 16)$ t/ha/Ka for the sediment yield since ~ 4420 cal year BP and $90 (\pm 17)$ t/ha in the modern event. Put simply, the sediment yield from 2016 erosion alone more than satisfies the average sediment yield over the last 4.4 Ka at this site. Nearby, Meyer et al. (2001) found an average sediment yield of ~ 160 t/ha/Ka between 7.4 and 6.6 Ka from alluvial fan records; our modern yield accounts for $>55\%$ of that in a single event. Kirchner et al. (2001) calculated sediment yields and denudation rates for 32 basins in Idaho ranging from 0.2-35,000 km² using ¹⁰Be concentrations in alluvial sediments. Averaged over 5-27 Ka, sediment yields were 550-2600 t/ha/Ka and denudation rates were ~ 20 -100 mm/Ka (Figure 1.12). Kirchner et al. (2001) compared their long-term values to measurements of sediment flux in streams and concluded that 70-97% of sediment is delivered in infrequent, large-magnitude events, i.e. extreme floods and following wildfire. Riley (2012) attributed 40-70% of the 35,000 km² Salmon River basin sediment yield over the last 6 Ka to post-fire debris-flows in the tributary 7500 km² Middle Fork Salmon River basin. Therefore, we argue that post-fire erosion, while brief and separated by long quiescent periods, dominates the long-term erosion signal in the Idaho Batholith and elsewhere.

Looking outside of the Idaho Batholith, Orem and Pelletier (2016) used a suite of approaches to show $>90\%$ of the million-year erosion rate is a result of post-fire erosion in Valles Caldera, NM (Figure 1.12). They found mean post-fire erosion rates exceed 1 mm / year, while long-term landscape denudation rates are 0.1 to 0.01 mm / yr (10-100 mm/Ka) (Orem and Pelletier, 2016). Our catchment-averaged erosion rate for the first

year post-fire was 6 mm/yr, and our long-term rate was 5mm/Ka; the same order of magnitude as Orem and Pelletier's (2016) estimates. In the Chiricahua Mountains in Arizona, 22 mm of catchment-averaged erosion in a 7.5 ha catchment from a 10-yr recurrence interval convective storm drastically exceeds the (not specifically fire-related) millennial-scale erosion rate of ~ 0.04 mm/yr from the nearby Pinaleno Mountains (Jungers and Heimsath, 2016; DeLong et al., 2018). In addition to these examples, numerous modern studies have measured post-fire erosion rates and magnitudes that greatly exceed background erosion (e.g. Moody et al., 2013). Our study corroborates prior work describing the critical impact of post-fire erosion over Holocene and Quaternary timescales.

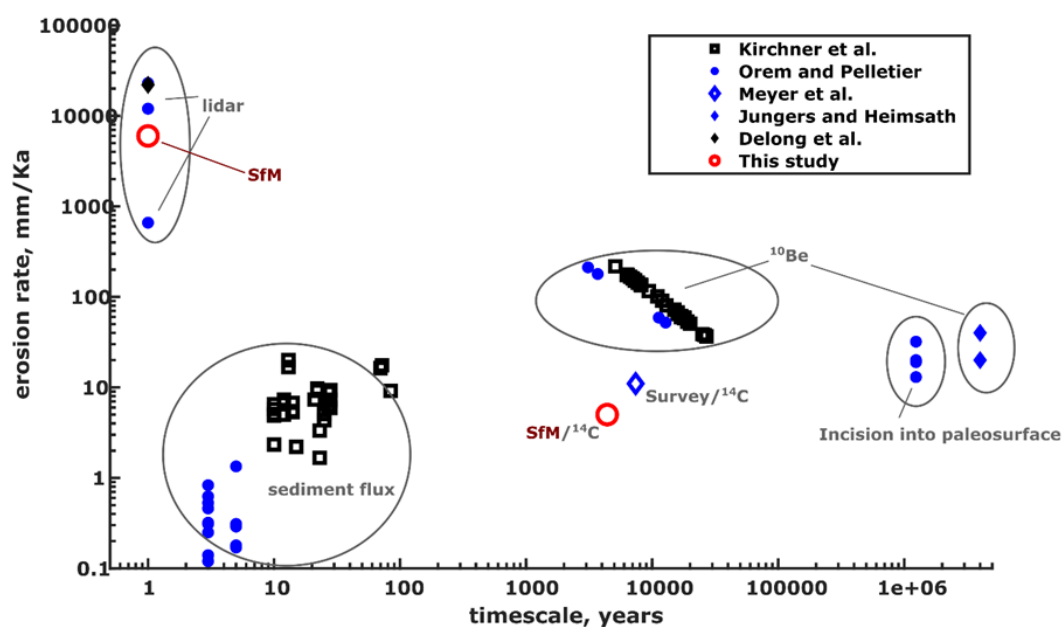


Figure 1.12: Plot of erosion rates versus timescale of measurement from selected studies in discussion. Open symbols are data from Idaho, including this study shown in red. Closed symbols are from SW USA. Measurements of erosion rates are from a variety of methods and catchment sizes. Adapted from Kirchner et al., 2001 and Orem and Pelletier, 2016.

Conclusion

Hillslope and channel erosion processes interact to produce ubiquitous erosion after wildfire in steep terrain. However, measuring each process is difficult at the scale of a typical catchment and few studies include Holocene magnitudes of post-fire erosion.

This study presents methods for partitioning post-fire rill and channel erosion processes that are flexible and robust. Importantly, we show that insights into erosional processes, sediment volumes, and their uncertainties, can be made across a representative, 1 km² catchment without detailed pre-erosion topography. We derived 5 cm resolution topography from SfM and adapted change detection techniques to show that the volume of debris-flow scour ($3500 \pm 420 \text{ m}^3$) contributed ~75% of the total measured eroded volume and ~60% of the estimated deposit volume. SfM is capable of accuracies <10 cm and is an appropriate tool for investigating post-fire erosion at cm-resolution, especially when coupled with UAV technology. Through Monte Carlo simulation using hillslope transect data, we showed that another ~25% ($1100 \pm 320 \text{ m}^3$) of the total eroded volume was contributed by rilling alone and clearly defined our uncertainty. Quantifying these two processes elucidates the overall role of channel and rill post-fire erosion for this typical Idaho Batholith catchment. Our hillslope rilling versus channel erosion partitions fall between values reported from other settings. Additionally, although this debris-flow was triggered by a low intensity precipitation event, the estimated deposit volume aligns fairly closely with the USGS post-fire debris-flow hazards model. Our approaches are relevant across smaller and larger catchment scales as climate change leads to more frequent and more severe fires in the near future.

We also confirm the overwhelming importance of post-fire erosion to long-term erosion rates and sediment yields by dating charcoal fragments preserved in stratigraphy. The modern post-fire erosion rate of 6 mm/year dominates the average erosion rate of 5 mm/Ka since the mid-Holocene at this site and agrees with other work from a range of settings. Expanding our temporal knowledge of post-fire erosion beyond the modern, such as we have done, is vital to better understand landscape evolution and to better prepare for impacts of erosion following fires on communities.

AN ISSUE OF SCALE: CONTRIBUTING AREA AND POST-FIRE EROSION

Abstract

At catchment outlets, the impacts of post-fire erosion on communities, infrastructure, and ecosystems are being highlighted and augmented by climate change. In steep, burned catchments, sediment is mobilized from hillslopes by multiple erosional processes; the basin-scale post-fire erosional response is ultimately controlled by a complex combination of basin characteristics (e.g. slope angle), sediment availability, precipitation variables, and the interaction and integration of channel networks and hillslopes. We use a 0.95 km² catchment burned in the 2016 Pioneer Fire in Idaho to quantify an important spatial threshold separating hillslope and channel erosion processes. Modest precipitation produced widespread rilling and a runoff-generated debris flow in the study catchment. We measure channel erosion by debris flow scour using 5 cm resolution Structure from Motion topography and hillslope erosion by rilling using transect data and explore their relationship at varying sub-basin sizes. We document the decreasing importance of hillslope processes to total eroded volumes as drainage area increases. In this setting, there is approximate parity between hillslope and channel eroded volumes at a drainage area of 0.2 km² (20 ha): channel erosion dominates the overall signal for contributing areas greater than 0.2 km² and hillslope erosion dominates the contribution of sediment for contributing areas smaller than this threshold. At drainage areas from 0.2-0.95 km², hillslope-channel connectivity increases and channel networks facilitate more efficient erosion. We compare the experimental results

from our study catchment to values from the post-fire literature, confirming the shift from hillslope-dominance to channel-dominance as drainage basin areas increases. Our sub-basin analyses show sediment yield increases with drainage area while other studies show the inverse, reflecting a variety of influences. Among these influences are the diverse geographic and geologic settings, the precipitation values, and the burn severity. Furthermore, the selection of field sites, the mode of measurement, and the timescale of measurement affect the reported sediment yield to drainage area relationship. Investigations into spatial thresholds separating hillslope and channel process-dominance, especially when coupled with high resolution topography, will help to quantify the landscape reaction to wildfire in other settings.

Introduction

Erosional processes in burned landscapes produce rapid and dramatic landscape changes which impact communities, infrastructure, and ecosystems. However, the delivery of sediment from hillslopes to basin mouths, where most homes, roads and other infrastructure are located depends on the connectivity of hillslopes and channels.

Connectivity is a continuum representing how efficiently material is transferred between landscape components (Grant et al., 2017; Wohl et al., 2018). Connectivity includes two concepts that vary in time and space: structural connectivity and functional connectivity (Wohl et al., 2018). Functional connectivity refers to the processes responsible for fluxes, while structural connectivity (system configuration) influences their boundaries and magnitudes. Changes to structural and functional connectivity are often non-linear and based on thresholds (Wohl et al., 2018).

Significant work has been devoted to thresholds across many systems, including Schumm's (1973) concept of complex response. For example, sediment flux is controlled by a critical gradient threshold (Roering et al., 1999), landscape dissection and channel initiation are controlled by a slope-area threshold (Montgomery and Dietrich, 1992; Montgomery and Foufoula-Georgiou, 1993), thresholds influence the occurrence of distinct hillslope processes (Dietrich et al., 1992), link river incision to tectonic uplift (Snyder et al., 2000), and couple hillslopes to valleys incised by debris flows (Stock and Dietrich, 2006). The spatial threshold of 0.1-1 km² drainage area signifies a transition to fluvial processes in many settings (Stock and Dietrich, 2006).

In post-fire settings, debris flows are initiated above a precipitation intensity-duration threshold or when a critical channel stability threshold is reached (McGuire et al., 2017; Staley et al., 2017). Wildfire changes infiltration, friction, and shear stress, reducing the critical area required for channel initiation or promoting infiltration-excess overland flow (Moody and Kinner, 2006; McGuire et al., 2018).

Fire usually reduces critical area, impacting hillslope processes (e.g. rilling, dry ravel, raindrop impact, and sheetwash) and their connectivity to channels (Meyer and Wells, 1997; Cannon et al., 2001; Moody and Kinner, 2006; Reneau et al., 2007; Moody et al., 2013). Hillslope erosional processes can promote debris flows when they transport material downslope and rapidly introduce sediment to channels (Staley et al., 2014). Therefore, high connectivity implies hillslopes and channels are closely coupled, allowing efficient export of detached sediment to the channel network, while low connectivity implies inefficient sediment transport. Accordingly, there should be a spatial

threshold differentiating low-efficiency (primarily hillslope) erosion from high-efficiency (primarily channel) erosion for a particular post-fire landscape.

In recent decades, high resolution topography (HRT) has significantly enhanced our understanding of landscape change through its ability to detect connectivity pathways and quantify thresholds (Passalacqua et al., 2015; Wohl et al., 2018). We define HRT as having 1 m or finer spatial resolution (e.g. Airborne Laser Swath Mapping (ALSM), Terrestrial Laser Scanning (TLS), and Structure from Motion Multi View Stereo (SfM-MVS, simplified to SfM hereafter). Moody et al. (2013) call for quantitative metrics to describe post-fire erosion processes and thresholds. Here, we investigate one post-fire threshold using SfM-derived HRT and hillslope transects.

This study intends to evaluate how post-fire hillslope and channel erosion vary with drainage area. Specifically, we demonstrate the drainage area threshold separating dominantly hillslope erosion from dominantly channel erosion for a 0.95 km² burned catchment in Idaho and relate it to connectivity. To do so, we produce and analyze a dataset of channel erosion by debris flow scour and hillslope erosion by rilling across multiple sub-basin sizes. Further, we ask how hillslope contributions to total erosion and sediment yield evolve with increasing drainage area, and we compare our observations to relevant literature.

Study Site, Debris Flow Occurrence, and Field Observations

Our study catchment is a 0.95 km² headwater catchment burned at moderate to high intensities in the ~750 km² 2016 Pioneer Fire in Idaho, USA (Figure 2.1A). The study catchment ranges in elevation from 1770-2320 m with 26° average slopes (45° max), receives ~100 cm of precipitation per year, and is underlain by weathered

Cretaceous biotite-granodiorite. Slopes are mostly soil-mantled and planar, becoming less steep near drainage divides. Valleys are v-shaped with a main channel and several tributaries supporting ephemeral flow. Pre-fire vegetation included Douglas Fir (*Pseudotsuga menziesii*) and Lodgepole Pine (*Pinus contorta*) and was last logged around 1960 (D. Brown, personal communication, 2018). Remnants of burned trees are mostly <1 m diameter.

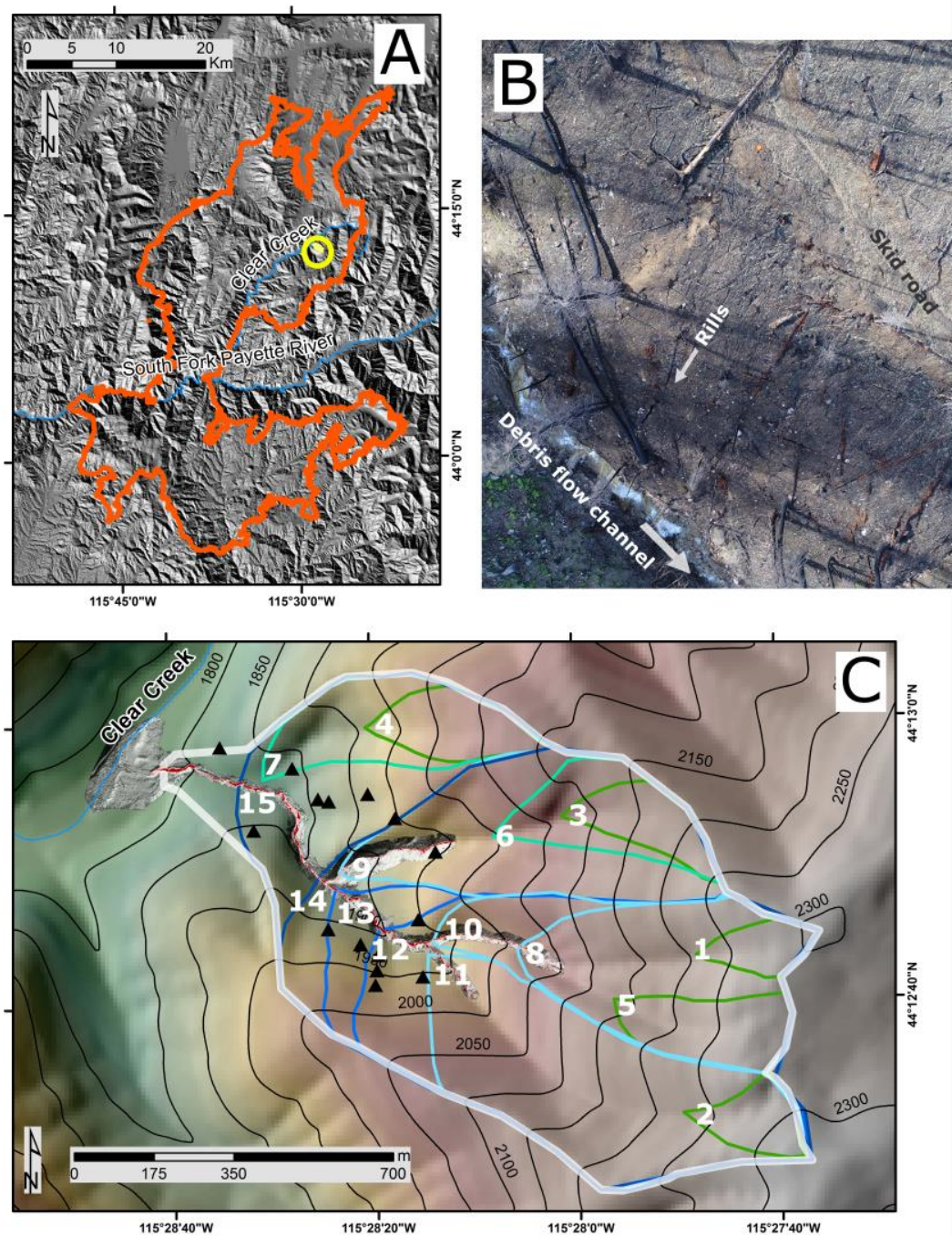


Figure 2.1: A) Area map of 2016 Pioneer Fire perimeter (orange) in Idaho. Yellow circle is study catchment location. Study catchment contributes to Clear Creek. B) UAS (aerial) image of rills on planar hillslopes connecting to scoured debris flow channel. Arrows give direction of flow. C) Detail map of study catchment. 0.95 km² full extent outlined in gray. Extent of SfM 5 cm resolution DEM shown as hillshade. Red shading shows channel scour measured with DoD. Black triangles show locations of hillslope transect used to derive rill erosion volumes. Analyzed sub-basins are outlined. Labels at sub-basin outlets correspond to Table 2.1. 50 m contours for scale.

The catchment was burned around August 30, 2016. A debris flow was triggered on October 15, 2016 with the catchment receiving 25 mm of rain in 24 hours with an estimated peak 15-minute intensity of 10 mm/hr (<http://prism.oregonstate.edu/explorer/>, accessed September 2018; <https://wcc.sc.egov.usda.gov/nwcc/site?sitenum=312>, accessed September 2018). Erosion response to this modest precipitation included widespread hillslope rilling leading to a runoff-generated debris flow. A large volume of sediment and large woody debris was delivered to the catchment outlet fan and impinged on Clear Creek.

Rilling was pervasive across the catchment, with rill heads located a few tens of meters from drainage divides. Rills on planar slopes were parallel and often discontinuous with lengths 10-100 m (Figure 2.1B). Rills coalesced into shallow gullies where topography was convergent. Burned out root casts were common and provided conduits into the subsurface. Rills were more common in the finer-grained regolith of north facing slopes. Besides hillslope rilling, burn marks on rocks and pedestals below rootlets and pebbles indicated raindrop impact and sheetwash had removed surface material, and flakes were spalled from granite boulders.

The scoured debris flow channel had a rectangular cross-section. We observed debris flow markers such as scarred trunks, cut roots, matted vegetation, mudlines, and large-caliber clasts deposited upstream of channel obstructions. The primary channel and tributaries were scoured to fresh bedrock in multiple locations. Channel margins were directly adjacent to steep hillslopes without any floodplain or break in slope.

Methods

In order to explore how hillslope and channel erosion process-dominance evolves with varying drainage area, we first quantified channel scour by debris flow and hillslope erosion by rilling across the entire 0.95 km² study catchment. We then subdivided the study catchment into 15 sub-basins and attributed corresponding values for rill erosion from hillslope transects and channel erosion from HRT.

We quantified and mapped the channel eroded volume using a 5 cm resolution DEM created with SfM. In Summer 2017, we collected overlapping images (n=837) of the trunk channel and tributaries using an unmanned aerial vehicle (UAS), then processed the photos into a point cloud using Agisoft Photoscan Professional. Ground control points (n=20) were surveyed with a real-time kinematic GPS unit, post processed to ~1 cm accuracy. The point cloud is available at:

<http://opentopo.sdsc.edu/dataspace/dataset?opentopoID=OTDS.012019.32611.1>. We gridded the point cloud (~900 pts/m²) into a 5 cm resolution DEM using CloudCompare (<https://www.danielgm.net/cc/>), preserving rich detail of the channel bed, banks, and margins. We differenced elevations from the surveyed, 5 cm post-erosion DEM from a synthetic pre-erosion surface to create a DEM of Difference (DoD) (Wheaton et al., 2010). We then calculated the channel volume by taking the sum of the grid cell areas multiplied by their elevation differences. The DoD also provides a spatially-explicit representation of scour depths and channel erosion by debris flow (Figure 2.1C). The measured eroded volume represents the majority of observed channel erosion but does not extend entirely to the channel heads. Further methodological details are provided in Chapter 1.

We quantified the rill eroded volume using 15 representative hillslope transects across the study catchment. At each transect, we recorded the number, width, and depth of individual rills ($n=175$). Transects included planar, convergent, and divergent hillslopes at a range of slope angles and distances from drainage divides. We used random sampling and Monte Carlo simulation to calculate the mean rill dimensions and number of rills per transect, normalized to a depth per unit area, and then applied this erosion magnitude to the catchment area impacted by rilling (0.77 km^2 of 0.95 km^2 total). Further methodological details are provided in Chapter 1.

We defined 15 sub-basins of various sizes within the study catchment to compare the relative channel versus hillslope erosion volumes (Figure 2.1C). These sub-basins were delineated from 10 m resolution topographic data. For each sub-basin, we determined the corresponding channel eroded volume from the 5 cm DoD and the rill eroded volume from the depth per unit area multiplied by the sub-basin area impacted by rilling. If no channel erosion was measured in the sub-basin, we consider it to have eroded only by rilling. In this manner, we explore the evolution of channel and hillslope erosion as a function of sub-basin size within the larger study catchment.

We also evaluated how sediment yield (mass/area/time) varies with drainage area. We converted eroded volumes to sediment yield using a bulk density of 1500 kg/m^3 for both our sub-basin analysis and for comparison with relevant literature in our discussion.

Results

Rill erosion depth was 1.4 mm per unit area and produced an eroded volume of 1104 m^3 at the full 95 ha study catchment extent, producing 24% of the total eroded

volume. Mean channel scour depth from the DoD was 0.8 m and channel erosion by debris flow scour produced a volume of 3467 m³, or 76% of the total erosion.

Results from the 15 analyzed sub-basins are summarized in Table 2.1. For sub-basins with drainage areas below 10 ha erosion was entirely by hillslope rilling (Figure 2.2). At approximately 20 ha (0.2 km²) drainage area, channel erosion and hillslope erosion contributed equal volumes. In sub-basins of a few hectares, channels were not developed and erosion was entirely by hillslope processes. Around 10 ha drainage area, channels began to contribute erosion volume, and at 20 ha drainage area channel and hillslope volumes reached parity. For drainage areas above 20 ha up to the study catchment extent of 95 ha, channels produced the majority of eroded volume. Sediment yield increased as drainage area increased (Figure 2.3), while the percentage of total erosion attributed to rilling (hillslope erosion) decreased as the basin size increased (Figure 2.4).

Table 2.1: Study catchment sub-basin data used in figures 2.2, 2.3, 2.4

Basin name	Sub-basin area (ha)	Area impacted by rilling (ha)	Rill eroded volume (m3)	Channel eroded volume (m3)	Total eroded volume (m3)	Rill yield (t/ha)	Channel yield (t/ha)	Sub-basin total yield (t/ha)	Hillslope erosion % of total
1	2.1	1.5	20.4	0.0	20.4	14.7	0.0	14.7	100
2	2.7	2.2	31.2	0.0	31.2	17.6	0.0	17.6	100
3	3.4	3.1	42.8	0.0	42.8	18.7	0.0	18.7	100
4	4.1	3.9	55.1	0.0	55.1	20.3	0.0	20.3	100
5	5.0	3.3	45.8	0.0	45.8	13.7	0.0	13.7	100
6	7.0	5.7	80.4	0.0	80.4	17.4	0.0	17.4	100
7	8.9	8.3	116.2	0.0	116.2	19.5	0.0	19.5	100
8	17.0	12.1	169.0	79.5	248.5	14.9	7.0	21.9	68
9	19.5	15.7	219.2	314.2	533.4	16.9	24.2	41.1	41
10	20.4	14.4	200.9	302.6	503.5	14.8	22.3	37.1	40
11	22.9	19.1	267.1	204.2	471.2	17.5	13.3	30.8	57
12	48.6	37.9	531.1	970.3	1501.3	16.4	29.9	46.3	35
13	52.6	41.4	579.7	1402.7	1982.4	16.5	40.0	56.6	29
14	75.4	59.7	836.0	1852.5	2688.5	16.6	36.8	53.5	31
15	93.2	75.0	1049.7	2838.8	3888.5	16.9	45.7	62.6	27
16	95.5	77.0	1104.0	3467.0	4571.0	17.3	54.5	71.8	24

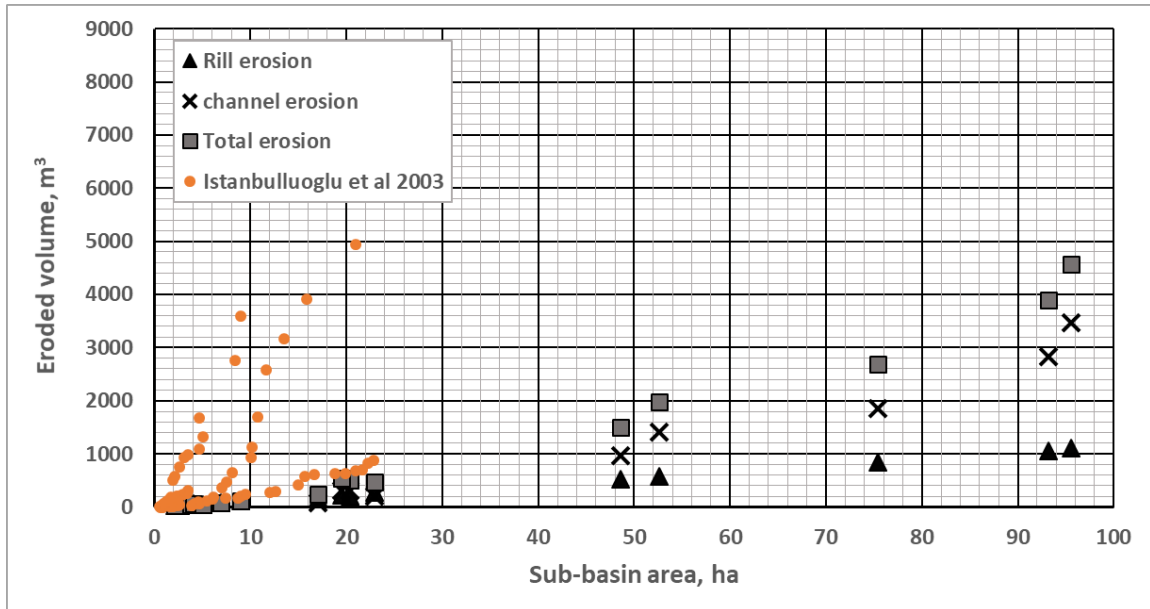


Figure 2.2: Eroded volumes from sub-basins within study catchment. Channel eroded volume surpasses hillslope eroded volume at a drainage area of about 20 hectares (0.2 km²). Channel erosion volumes also increase about three times faster than rill erosion volumes, reflecting increased integration and efficiency of channel networks. Total erosion volume (channel + rill) is shown in gray squares. Rill erosion volumes (triangles) are extrapolated from hillslope transect data and applied as a uniform 1.4 mm per unit area erosion where rilling was observed. Channel erosion volumes (X's) are from 5 cm resolution DEM of Difference derived from synthetic pre-erosion and surveyed post-erosion Structure from Motion survey. Orange circles are data from post-fire gully erosion, in similar Idaho Batholith terrain (Istanbulluoglu et al., 2003).

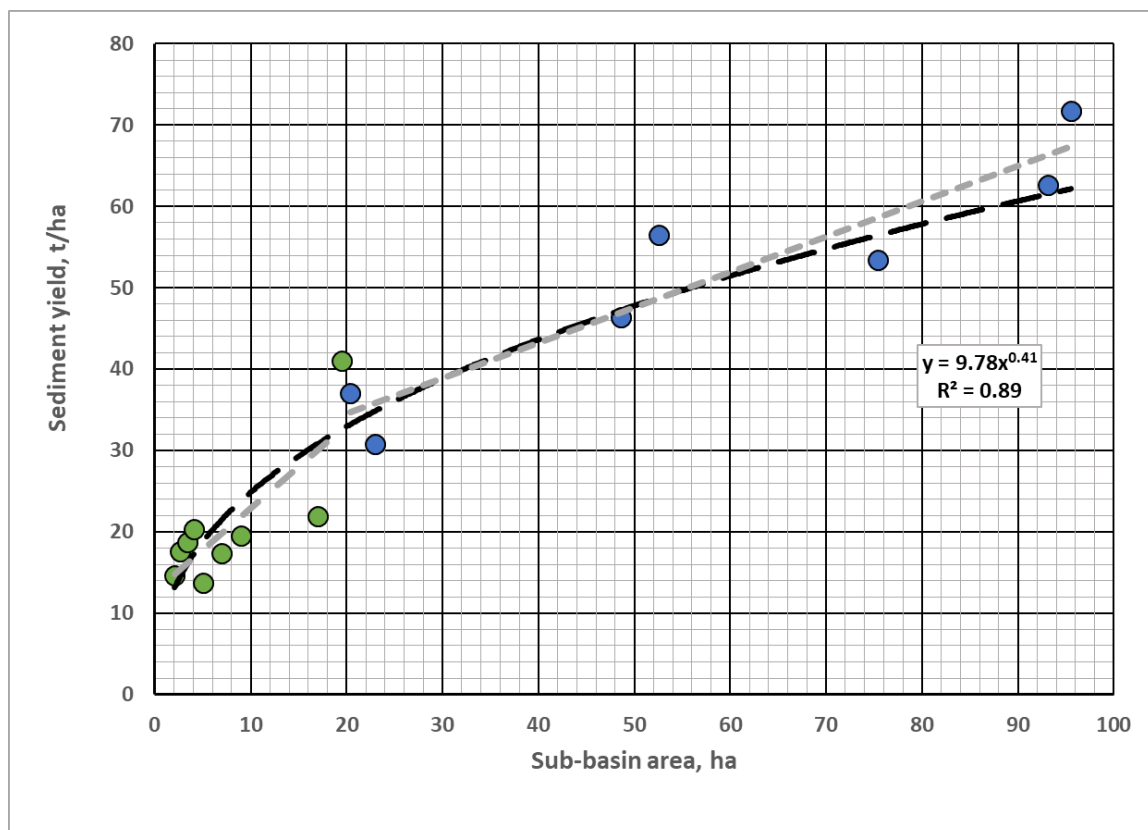


Figure 2.3: Sediment yield, in metric tons per hectare per year (mass/area/time) for sub-basins of varying size within the study catchment. Sediment yields increase as the scale of analysis increases, up to the 95 hectare study catchment size. Data from all drainage areas are fit with a power law function (black dashed line). Channel networks are not present at the smallest drainage areas. As drainage area increases, hillslopes are more closely coupled to channels and connectivity improves, allowing increased sediment yields. Green symbols represent contributing areas below 20 ha, where rill erosion contributes a majority of total erosion. Blue symbols represent contributing areas above 20 ha, where channel erosion contributes a majority of total erosion. Gray dashed lines are linear best fits above and below the 20 ha drainage area threshold, representing a change in process-dominance. A positive relationship between post-fire sediment yield and drainage area is shown in other studies, e.g. Gabet and Bookter, 2008; Moody and Martin, 2009; Pelletier and Orem, 2014. Sediment yields are converted from measured eroded volumes using a bulk density of 1500 kg/m³.

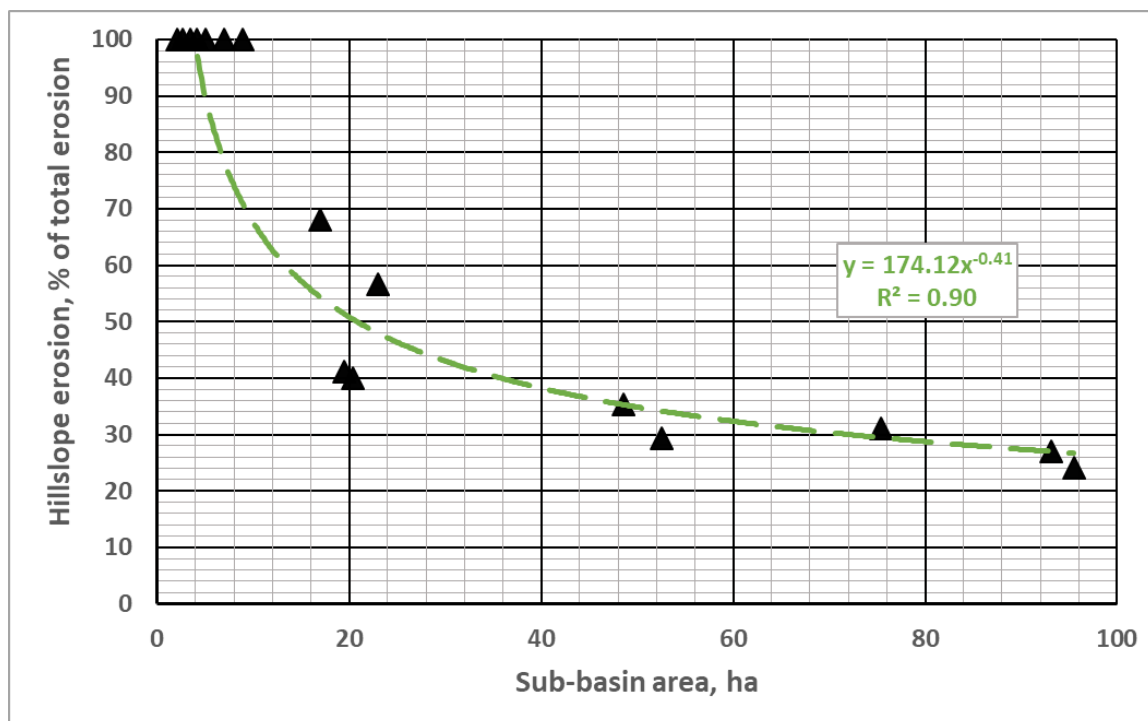


Figure 2.4: Percent contribution of hillslope erosion (rilling) to total erosion for varying size sub-basins within the study catchment. At small drainage areas, erosion is entirely by hillslope erosion. As the drainage area increases and channels are present, the relative contribution of hillslope erosion diminishes. In this setting, the threshold between hillslope-process dominance and channel-process dominance (purple shading) occurs at a drainage area of about 20 hectares (0.2 km²). Data are fit with a power law function (dashed line).

Discussion

Uncertainty and Assumptions:

Our quantification of channel eroded volume does not extend to channel heads. From our field observations we are confident the DoD captures the largest-magnitude channel erosion and most of the significant channel erosion. However, mapping the locations of more channel heads with imagery (e.g. from UAS) or in the field would provide a more complete picture of the hillslope-channel connectivity. HRT of the entire catchment would facilitate additional analyses at appropriate scales (Passalacqua et al., 2015). Our DoD has a total volume uncertainty of 12% as characterized in Chapter 1.

Our method to extrapolate the rill measurements from 15 transects to the entire watershed is predicated on the mean rill dimensions. Considering the rill erosion to be a spatially consistent depth per unit area simplifies the quantification of erosion attributed to rilling. Our statistical approach could be misleading because it is not a spatially explicit representation of the significant variability recorded by our hillslope transects. Intuitively, we would expect rill dimensions and the number of rills to increase downslope as contributing areas become larger and flow paths lengthen. However, for parallel rills on planar slopes, dimensions are consistent downslope and the contributing area per rill is moderated (Moody and Kinner, 2006). Additionally, in the field we observed that rills were commonly discontinuous; individual rills encountered surface depressions or roughness and disappeared, or initiated with minimal convergent area. Therefore, our constant 1.4 mm of rill erosion per unit area may sufficiently represent rill erosion for our study's purpose. Our total rill volume has an uncertainty of 29%.

For this discussion, we avoid point and plot measurements of hillslope erosion from the post-fire literature because contributing areas are often ambiguous. Instead, we focus on studies that clearly define the basin area, the measurement method, and report sediment yield in mass/area/time. The sediment yields we report from our study catchment (t/ha/yr) are minimum values because our channel and rill eroded volumes only measured one event. Special attention is brought to studies that implement HRT to partition hillslope erosion magnitudes from channel erosion magnitudes.

Channel Erosion Outpaces Hillslope Erosion as Drainage Area Increases

We found that channel erosion volumes increase more quickly than rill erosion volumes with increasing drainage area (Figure 2.2). We attribute this relationship to increasing connectivity provided by the channel network at larger drainage areas. Interill erosion (which we did not measure) is dominated by rainfall, whereas runoff controls rill and channel erosion (Aksoy and Kavvas, 2005). Therefore, as contributing area increases the importance of runoff erosion also increases, promoting channel erosion (rather than hillslope erosion). Additionally, rill and channel erosion are reflective of structural and functional connectivity and are related and especially dynamic in post-fire scenarios (Wohl et al., 2018). Competent runoff is required to link hillslope rill erosion to channels (Wester et al., 2014). Additionally, fires remove riparian vegetation, further increasing hillslope-channel connectivity (Wester et al., 2014). Where drainage area is too small to support a channel, erosion by rilling has limited capacity to transport sediment. However, where channels are present and connected to the hillslopes, such as the steep-sided and narrow valleys at our study site, sediment produced from hillslopes is transported to the sub-basin outlet more efficiently. Additionally, runoff-generated debris flows increase in volume as they proceed downstream, either by the continued addition of hillslope material, the scouring of their channel, or both (Meyer and Wells, 1997; Cannon et al., 2001; Gabet and Bookter, 2008; Santi et al., 2008). Resultingly, the eroded volume to drainage area relationship becomes noticeably more positive for drainage areas that include channel processes. This result is broadly consistent with Moody and Martin (2009), who compiled studies of post-fire erosion across the western United States and

found channels contribute 75% (240 t/ha/yr average) of total erosion compared to 25% (82 t/ha/yr average) erosion contribution from hillslopes.

Conceptually, the outsized impact of channel erosion to total post-fire erosion is moderated over longer timescales. Low background rates of sediment transport on hillslopes integrate over long time intervals between fires (e.g. a few hundred years), to store considerable volumes of erodible material in channels. Increased surface runoff and peak discharges immediately after fire are able to evacuate this stored material, enabling removal of material derived from long-term hillslope processes and facilitate overall landscape-wide erosion.

Spatial Threshold at 20 ha Drainage Area

From our sub-basin data, we observe that a switch between hillslope-dominance and channel-dominance of total erosion occurs near 20 ha (0.2 km²) drainage area (Figures 2.2 and 2.4). We are not implying that 20 ha is the critical area for channel initiation (i.e. Montgomery and Foufoula-Georgiou, 1993). Other post-fire studies have quantified critical area; fire reduces the critical area required for channel initiation from 1 ha (unburned) to 0.2 ha in Colorado (Moody and Kinner, 2006), and a transition from hillslope to hollow occurs at 0.1 ha in Valles Caldera, New Mexico (Pelletier and Orem, 2014). Rather, the 20 ha drainage area threshold produces approximately equal eroded volumes from hillslope (rilling) and channel (debris flow scour) processes in this setting.

The 20 ha spatial threshold signifies strong connectivity between the detachment and transport of sediment on hillslopes and the channel network. For larger drainage areas, channels efficiently transport sediment as well as contribute erosion. For smaller drainage areas, hillslopes are not tightly coupled to the channel network and sediment

flux is dampened. Investigating this spatial threshold in other burned settings may help constrain this value for varied hydro-geomorphic regimes. Over long time scales, hillslope to valley coupling is moderated by fire frequency, rainfall, vegetation, and soil production (Roering and Gerber, 2005).

Inconsistent Sediment Yield and Drainage Area Relationship

For our analyzed sub-basins, total eroded volume (Figure 2.2) and sediment yield (Figure 2.3) increase as the drainage area increases. Cannon et al. (1998), Gabet and Bookter (2008), and Pelletier and Orem (2014) also report volume increasing with drainage area, although each uses a different type of function to represent the relationship. Similarly, Moody and Martin (2009) give the summary that post-fire sediment yield increases with spatial scale from hillslopes to channel networks. “When hillslope processes dominate channel processes, sediment yield decreases as drainage area increases. When channel processes dominate hillslope processes, sediment yield increases as drainage area increases. The latter is the case after wildfires.” (Moody and Martin, 2009). Hillslope and channel landscape compartments and erosional process are fundamentally related: burned hillslopes produce surface runoff, but concentrated flow (channels) produce more sediment (Macdonald and Robichaud, 2010). In other words, channel erosion cannot occur without runoff generated on hillslopes.

However, most studies report an inverse relationship between sediment yield and drainage area in burned and unburned setting (Shakesby and Doerr, 2006; Macdonald and Robichaud, 2010). Scott et al. (1998) found higher soil losses at midslope plots than measured at the catchment scale, with sediment delivery ratios (SDR) from 0.08-0.5. Wagenbrenner and Robichaud (2014) report SDR and sediment yield decreased

significantly as the catchment size increased using bedload measurements from several sites and scales. A compilation of post-fire literature values bears this out, showing a decline in sediment yield for increasing drainage areas (Table 2.2 and Figure 2.5). These data are scattered due to an array of methods, settings, and erosion processes, but a trend is recognizable. HRT post-fire studies show the same trend of decreasing sediment yield with increasing drainage area. A constant sediment yield for various drainage areas may imply landscape equilibrium (Reneau and Dietrich, 1991).

Table 2.2: Literature sediment yield and drainage area data used in figures 2.5 and 2.7

High resolution topography only			
Study	Basin size, ha	Sediment yield, t/ha	Hillslope erosion % of total
This study	95.5	72	24
DeLong et al., 2018	7.5	118	68
DeLong et al., 2018	2.6	340	68
Renger et al., 2016	0.6	394	87
Orem and Pelletier, 2015	136	121	-
Orem and Pelletier, 2015	132	61	-
Staley et al., 2014	1	384	93
Literature post-fire erosion values			
Study	Basin size, ha	Sediment yield, t/ha	Hillslope erosion % of total

Gabet and Bookter, 2008	30	29	-
Gabet and Bookter, 2008	15	134	-
Gabet and Bookter, 2008	23	187	-
Gabet and Bookter, 2008	27	62	-
Gabet and Bookter, 2008	8	239	-
Gabet and Bookter, 2008	76	72	-
Meyer and Wells, 1997	159	109	30
Meyer et al., 2001	49	442	51
Nyman et al., 2011	70	120	72
Nyman et al., 2011	12	270	65
Nyman et al., 2011	30	150	35
Nyman et al., 2015	33	148	18
Nyman et al., 2015	72	132	20
Nyman et al., 2015	65	116	43
Nyman et al., 2015	36	113	48
Nyman et al., 2015	100	186	55

Nyman et al., 2015	12	251	43
Nyman et al., 2015	120	147	41
Nyman et al., 2015	220	294	33
Nyman et al., 2015	23	158	58
Nyman et al., 2015	8	151	62
Pelletier and Orem, 2014	10	15	-
Pelletier and Orem, 2014	100	15	-
Santi et al., 2008	125	75	3

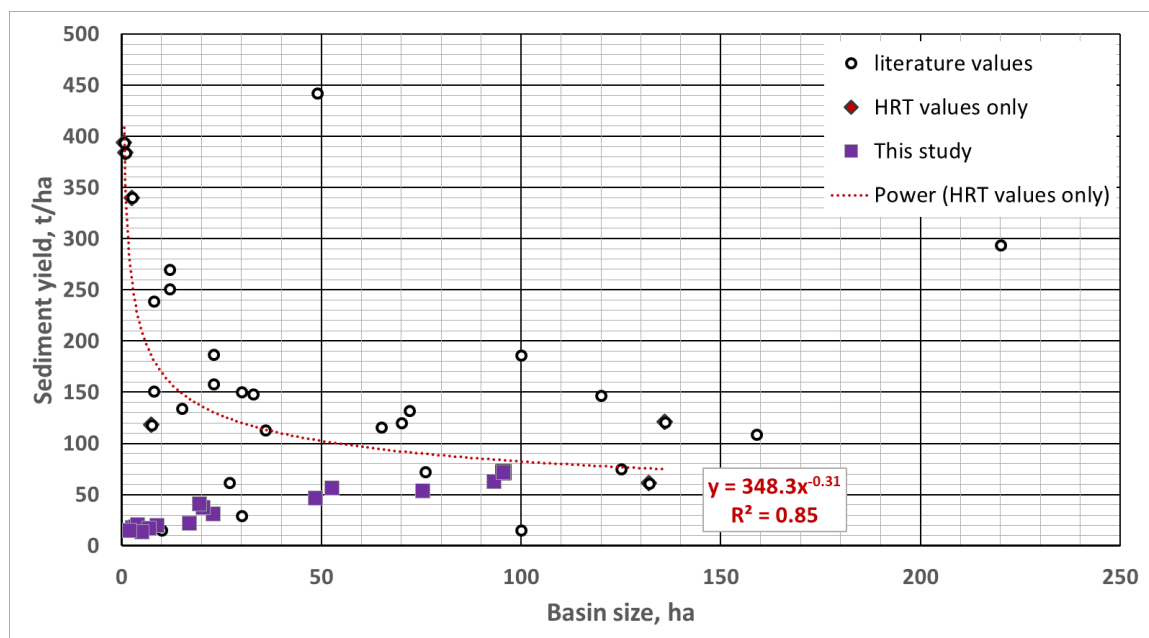


Figure 2.5: Post-fire erosion literature values for sediment yield plotted against basin size. Sediment yield (t/ha) decreases as drainage area increases. A common explanation for this negative relationship is increased opportunities for sediment storage or deposition in larger catchments (Lane et al., 1997; Scott et al., 1998; Shakesby and Doerr, 2006; Wagenbrenner and Robichaud, 2014). However, this result seems at odds with data from sub-basins within our study catchment (Figure 2.3). Open circle symbols are measurements from multiple methods where basin sizes were clearly reported. Filled red diamond symbols are measurements from high-resolution topography (HRT) methods, this study is shown with purple squares. The HRT data are fit with a power law function (dotted line).

A common explanation for reduced sediment yields in larger catchments is that they have greater opportunities to store sediment (Scott et al., 1998; Aksoy and Kavvas, 2005; Shakesby and Doerr, 2006). From a connectivity standpoint, higher-order drainages have greater ability to dampen signals (Wohl et al., 2018). Additionally, measurement techniques over large spatial extents (including HRT) are not sensitive to small changes and therefore may not record the sediment yield signal.

So, why does our sub-basin analysis show a positive sediment yield to drainage area relationship and most literature the opposite? Undoubtedly there are localized differences: Wagenbrenner and Robichaud (2014) noted that sediment yield did not

decrease with contributing area at their Hayman site, which has gus hillslopes similar to those in our study catchment. Process differences also impact sediment yields at varying scales, such as soil detachment at the hillslope scale, bank erosion at the sub-basin scale, and runoff amount at the watershed scale (Lane et al., 1997). Hillslope and channel sediment yields from disparate landscapes must be compared with caution (Moody and Martin, 2009). Moody et al. (2013) remind us that “results cannot be scaled up or down unless the dominant process is known to have the same temporal and spatial scales.” Hillslope and channel landscape compartments and erosional process are fundamentally related: burned hillslopes produce surface runoff, but concentrated flow in channels produce more sediment (Macdonald and Robichaud, 2010). In other words, channel erosion cannot occur without runoff generated on hillslopes. Lastly, sediment yield is inherited from large-scale questions in sedimentary research. It can be a misleading metric for post-fire erosion processes because of their intermittency (Figure 2.6), (Swanson, 1981; Moody et al., 2013).

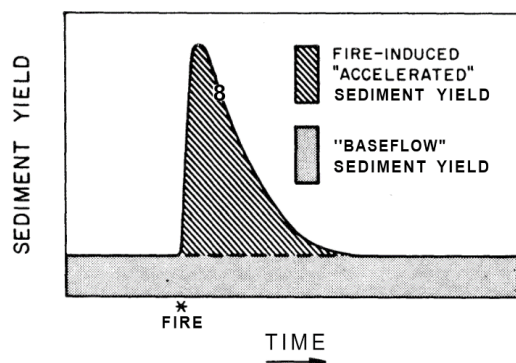


Figure 2.6: Conceptual diagram from Swanson (1981) illustrating the intermittent nature of post-fire sediment yields.

Hillslope Contribution as a Function of Drainage Area

Our sub-basin analysis shows the contribution from hillslopes as a percentage of total erosion decreases as the drainage area increases (Figure 2.4), consistent with other post-fire literature. Relatively few studies partition total erosion into hillslope and channel components. However, those that do show that hillslopes contribute less to total erosion as drainage area increases (Figure 2.7).

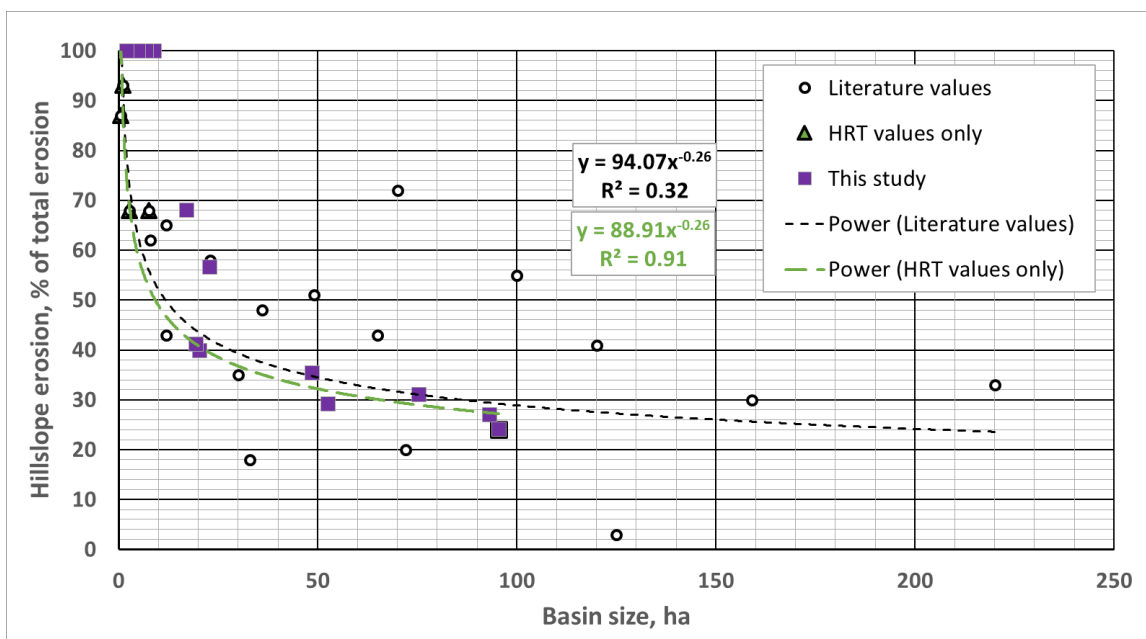


Figure 2.7: Post-fire literature values for the percent contribution of hillslope erosion to total erosion for varying basin sizes. At small drainage areas, hillslope processes contribute all or most erosion. As drainage area increases, channel processes become more dominant. Open circle symbols are measurements from multiple settings and methods where basin sizes were clearly reported. These data are fit with a power law function (black dashed line). Filled green triangle symbols are from high-resolution topography (HRT) methods, including this study shown with purple squares. HRT data are fit with a power law function (green dashed line). While taken from few data points, the similarity of fitted lines is encouraging. Variation in the literature values is reflective of diverse settings (geology, fire, precipitation, basin characteristics, etc) as well as multiple measurement methods.

Partitioning eroded volumes into channel and hillslope components is facilitated by HRT differencing. Multi-temporal surveys, especially those with cm-resolution from

TLS and SfM, diagnose the spatial signatures of erosion and relate quantified volumes to specific processes (e.g. (Staley et al., 2014; Rengers et al., 2016; DeLong et al., 2018)). However, these TLS surveys are focused on small study basins (0.5-7.5 ha) and consequently, hillslope processes dominate. Considering studies from a range of larger drainage areas, our experimental result of decreasing hillslope contribution to total erosion is confirmed. A power-law function produces a satisfactory fit to both our experimental data (Figure 2.4) and values from the literature (Figure 2.7), albeit with different exponents potentially reflecting the diversity of settings. Our interpretation is that this relationship illustrates increased sediment flux efficiency from channels and better connectivity for increasing drainage areas, rather than a relative reduction in hillslope erosion processes.

Conclusion

The connectivity of sediment fluxes from hillslopes to channels is a critical topic as post-fire erosion processes impact communities, infrastructure, and ecosystems. In all watersheds, hillslope surface area drastically exceeds channel surface area. Yet hillslope erosion processes (e.g. rilling) are very rarely quantified at appropriate spatial scales (i.e. a typical headwater catchment). Erosion in channels by concentrated flow cannot occur without runoff generated on hillslopes, but to date many post-fire domains lack volumetric and spatial comparisons between hillslope and channel sediment contributions. We sought to quantify a fundamental spatial threshold separating channel and hillslope processes. To do so, we made measurements of channel erosion by debris flow scour and hillslope erosion by rilling in a 0.95 km² Idaho catchment and compared their magnitudes at multiple sub-basin extents. We found channel eroded volume

increases faster than hillslope eroded volume as basin area increases, reflecting increased hillslope-channel connectivity and more efficient sediment transport through the channel network. In this setting, the hillslope-dominance to channel-dominance threshold exists at a drainage area of ~20 hectares. A positive relationship between sediment yield and basin size in our experimental data is not consistent with literature values, which indicate a generally inverse relationship between sediment yield and drainage area. Variability in these relationships is reflective of the measurement methods and the array of post-fire settings, among many factors. Our approach of dividing a larger watershed into sub-catchments of varying contributing areas is an efficient method to investigate post-fire erosion. Few post-fire erosion studies employ high-resolution topography to differentiate channel and hillslope erosion magnitudes, but those that do help elucidate important process-based changes and demonstrate how hillslope-channel coupling evolves with drainage area.

REFERENCES

- Abatzoglou JT, Williams AP, Turner MG. 2016. Impact of anthropogenic climate change on wildfire across western US forests. *PNAS* 113 : 11770–11775. DOI: 10.1073/pnas.1607171113
- Aksoy H, Kavvas ML. 2005. A review of hillslope and watershed scale erosion and sediment transport models. 247–271 pp. 30 December
- Bales RC, Molotch NP, Painter TH, Dettinger MD, Rice R, Dozier J. 2006. Mountain hydrology of the western United States. *Water Resources Research* 42 DOI: 10.1029/2005WR004387
- Benavides-Solorio JDD, MacDonald LH. 2005. Measurement and prediction of post-fire erosion at the hillslope scale, Colorado Front Range. *International Journal of Wildland Fire* DOI: 10.1071/WF05042
- Bigio E, Swetnam TW, Baisan CH. 2010. A comparison and integration of tree-ring and alluvial records of fire history at the Missionary Ridge Fire, Durango, Colorado, USA. *Holocene* 20 : 1047–1061. DOI: 10.1177/0959683610369502
- Brogan DJ, Nelson PA, MacDonald LH. 2017. Reconstructing extreme post-wildfire floods: a comparison of convective and mesoscale events. *Earth Surface Processes and Landforms* DOI: 10.1002/esp.4194
- Cannon SH, Gartner JE, Rupert MG, Michael JA, Rea AH, Parrett C. 2010. Predicting the probability and volume of postwildfire debris flows in the intermountain western United States. *Bulletin of the Geological Society of America* DOI: 10.1130/B26459.1
- Cannon SH, Kirkham RM, Parise M. 2001. Wildfire-related debris-flow initiation processes, Storm King Mountain, Colorado. *Geomorphology* 39 : 171–188. DOI: 10.1016/S0169-555X(00)00108-2

- Cannon SH, Powers PS, Savage WZ. 1998. Fire-related hyperconcentrated and debris flows on Storm King Mountain, Glenwood Springs, Colorado, USA. *Environmental Geology* DOI: 10.1007/s002540050307
- Carbonneau PE, Dietrich JT. 2017. Cost-effective non-metric photogrammetry from consumer-grade sUAS: implications for direct georeferencing of structure from motion photogrammetry. *Earth Surface Processes and Landforms* DOI: 10.1002/esp.4012
- Clapuyt F, Vanacker V, Van Oost K. 2016. Reproducibility of UAV-based earth topography reconstructions based on Structure-from-Motion algorithms. *Geomorphology* DOI: 10.1016/j.geomorph.2015.05.011
- Cook KL. 2017. An evaluation of the effectiveness of low-cost UAVs and structure from motion for geomorphic change detection. *Geomorphology* DOI: 10.1016/j.geomorph.2016.11.009
- Costa JE. 1984. Physical Geomorphology of Debris Flows. In *Developments and Applications of Geomorphology*, Costa JE and Fleisher PJ (eds). Springer: Berlin; 268–317.
- Cunliffe AM, Brazier RE, Anderson K. 2016. Ultra-fine grain landscape-scale quantification of dryland vegetation structure with drone-acquired structure-from-motion photogrammetry. *Remote Sensing of Environment* DOI: 10.1016/j.rse.2016.05.019
- Daly C, Neilson RP, Phillips DL. 1994. A Statistical-Topographic Model for Mapping Climatological Precipitation over Mountainous Terrain. *Journal of Applied Meteorology* 33 : 140–158.
- Debanò LF. 2000. The role of fire and soil heating on water repellency in wildland environments: A review. *Journal of Hydrology* 231–232 : 195–206. DOI: 10.1016/S0022-1694(00)00194-3
- Degraff J V, Cannon SH, Gartner JE. 2015. The Timing of Susceptibility to Post-Fire Debris Flows in the Western United States. *Environmental and Engineering Geoscience* 21 : 277–292.

- DeLong SB, Prentice CS, Hilley GE, Ebert Y. 2012. Multitemporal ALSM change detection, sediment delivery, and process mapping at an active earthflow. *Earth Surface Processes and Landforms* DOI: 10.1002/esp.2234
- DeLong SB, Youberg AM, DeLong WM, Murphy BP. 2018. Post-wildfire landscape change and erosional processes from repeat terrestrial lidar in a steep headwater catchment, Chiricahua Mountains, Arizona, USA. *Geomorphology* DOI: 10.1016/j.geomorph.2017.09.028
- Dibiase RA, Lamb MP. 2013. Vegetation and wildfire controls on sediment yield in bedrock landscapes. *Geophysical Research Letters* DOI: 10.1002/grl.50277
- Dietrich WE, Wilson CJ, Montgomery DR, McKean J, Bauer R. 1992. Erosion thresholds and land surface morphology. *Geology* DOI: 10.1130/0091-7613(1992)020<0675:ETALSM>2.3.CO;2
- Eltner A, Baumgart P, Maas HG, Faust D. 2015. Multi-temporal UAV data for automatic measurement of rill and interrill erosion on loess soil. *Earth Surface Processes and Landforms* DOI: 10.1002/esp.3673
- Eppes M-C, Keanini R. 2017. Mechanical Weathering and Rock Erosion by Climate-Dependent Subcritical Cracking. *Reviews of Geophysics* DOI: 10.1002/2017RG000557
- Fitch EP, Meyer GA. 2016. Temporal and spatial climatic controls on Holocene fire-related erosion and sedimentation, Jemez Mountains, New Mexico. *Quaternary Research (United States)* DOI: 10.1016/j.yqres.2015.11.008
- Gabet EJ, Bookter A. 2008. A morphometric analysis of gullies scoured by post-fire progressively bulked debris flows in southwest Montana, USA. *Geomorphology* DOI: 10.1016/j.geomorph.2007.03.016
- Gartner JE, Cannon SH, Santi PM, Dewolfe VG. 2008. Empirical models to predict the volumes of debris flows generated by recently burned basins in the western U.S. *Geomorphology* DOI: 10.1016/j.geomorph.2007.02.033
- Gillan JK, Karl JW, Elaksher A, Duniway MC. 2017. Fine-resolution repeat topographic surveying of dryland landscapes using UAS-based structure-from-motion

- photogrammetry: Assessing accuracy and precision against traditional ground-based erosion measurements. *Remote Sensing* DOI: 10.3390/rs9050437
- Glendell M et al. 2017. Testing the utility of structure-from-motion photogrammetry reconstructions using small unmanned aerial vehicles and ground photography to estimate the extent of upland soil erosion. *Earth Surface Processes and Landforms* 42 : 1860–1871. DOI: 10.1002/esp.4142
- Goetz J, Brenning A, Marcer M, Bodin X. 2018. Modeling the precision of structure-from-motion multi-view stereo digital elevation models from repeated close-range aerial surveys. *Remote Sensing of Environment* DOI: 10.1016/j.rse.2018.03.013
- Goode JR, Luce CH, Buffington JM. 2012. Enhanced sediment delivery in a changing climate in semi-arid mountain basins: Implications for water resource management and aquatic habitat in the northern Rocky Mountains. *Geomorphology* DOI: 10.1016/j.geomorph.2011.06.021
- Gould GK, Liu M, Barber ME, Cherkauer KA, Robichaud PR, Adam JC. 2016. The effects of climate change and extreme wildfire events on runoff erosion over a mountain watershed. *Journal of Hydrology* DOI: 10.1016/j.jhydrol.2016.02.025
- Grant GE, O'Connor J, Safran E. 2017. Excursions in fluvial (dis)continuity. *Geomorphology* 277 : 145–153. DOI: 10.1016/j.geomorph.2016.08.033
- Heimsath AM, Dietrich WE, Nishiizumi K, Finkel RC. 1997. The soil production function and landscape evolution. *Nature* 388 : 358–361.
- Istanbulluoglu E, Tarboton DG, Pack RT, Luce C. 2003. A sediment transport model for incision of gullies on steep topography. *Water Resources Research* DOI: 10.1029/2002WR001467
- James MR, Robson S. 2012. Straightforward reconstruction of 3D surfaces and topography with a camera: Accuracy and geoscience application. *Journal of Geophysical Research: Earth Surface* DOI: 10.1029/2011JF002289
- James MR, Robson S. 2014. Mitigating systematic error in topographic models derived from UAV and ground-based image networks. *Earth Surface Processes and Landforms* DOI: 10.1002/esp.3609

- James MR, Robson S, d'Oleire-Oltmanns S, Niethammer U. 2017. Optimising UAV topographic surveys processed with structure-from-motion: Ground control quality, quantity and bundle adjustment. *Geomorphology* DOI: 10.1016/j.geomorph.2016.11.021
- Javernick L, Brasington J, Caruso B. 2014. Modeling the topography of shallow braided rivers using Structure-from-Motion photogrammetry. *Geomorphology* DOI: 10.1016/j.geomorph.2014.01.006
- Johnson K, Nissen E, Saripalli S, Arrowsmith JR, McGarey P, Scharer K, Williams P, Blisniuk K. 2014. Rapid mapping of ultrafine fault zone topography with structure from motion. *Geosphere* DOI: 10.1130/GES01017.1
- Jungers MC, Heimsath AM. 2016. Post-tectonic landscape evolution of a coupled basin and range: Pinaleño Mountains and Safford Basin, southeastern Arizona. *Bulletin of the Geological Society of America* DOI: 10.1130/B31276.1
- Kampf SK, Brogan DJ, Schmeer S, MacDonald LH, Nelson PA. 2016. How do geomorphic effects of rainfall vary with storm type and spatial scale in a post-fire landscape? *Geomorphology* DOI: 10.1016/j.geomorph.2016.08.001
- Kean JW, Staley DM, Cannon SH. 2011. In situ measurements of post-fire debris flows in southern California: Comparisons of the timing and magnitude of 24 debris-flow events with rainfall and soil moisture conditions. *Journal of Geophysical Research: Earth Surface* DOI: 10.1029/2011JF002005
- Kiilsgaard TH, Stanford LR, Lewis RS. 2006. Geologic Map of the Deadwood River 30 x 60 minute Quadrangle, Idaho. Idaho Geological Survey Geologic Map 45
- Kinnell PIA. 2005. Raindrop-impact-induced erosion processes and prediction: A review. *Hydrological Processes* 19 : 2815–2844. DOI: 10.1002/hyp.5788
- Kirchner JW, Finkel RC, Riebe CS, Granger DE, Clayton JL, King JG, Megahan WF. 2001. Mountain erosion over 10 yr, 10 k.y., and 10 m.y. time scales. *Geology* 29 : 591–594.

- Lane LJ, Hernandez M, Nichols M. 1997. Processes controlling sediment yield from watersheds as functions of spatial scale. *Environmental Modelling and Software* DOI: 10.1016/S1364-8152(97)00027-3
- Langhans C, Nyman P, Noske PJ, Van der Sant RE, Lane PNJ, Sheridan GJ. 2017. Post-fire hillslope debris flows: Evidence of a distinct erosion process. *Geomorphology* DOI: 10.1016/j.geomorph.2017.06.008
- Leon JX, Roelfsema CM, Saunders MI, Phinn SR. 2015. Measuring coral reef terrain roughness using “Structure-from-Motion” close-range photogrammetry. *Geomorphology* 242 : 21–28. DOI: 10.1016/j.geomorph.2015.01.030
- Lucieer A, De Jong SM, Turner D. 2014. Mapping landslide displacements using Structure from Motion (SfM) and image correlation of multi-temporal UAV photography. *Progress in Physical Geography* 38 : 97–116. DOI: 10.1177/0309133313515293
- Macdonald L, Robichaud P. 2010. Post-fire Erosion and the Effectiveness of Emergency Rehabilitation Treatments over Time Runoff and Sediment Production at Various Scales in Dry Tropical Settings
<https://www.researchgate.net/publication/242664874>
- McGuire LA, Kean JW, Staley DM, Rengers FK, Wasklewicz TA. 2016. Constraining the relative importance of raindrop- and flow-driven sediment transport mechanisms in postwildfire environments and implications for recovery time scales. *Journal of Geophysical Research: Earth Surface* DOI: 10.1002/2016JF003867
- McGuire LA, Rengers FK, Kean JW, Staley DM. 2017. Debris flow initiation by runoff in a recently burned basin: Is grain-by-grain sediment bulking or en masse failure to blame? *Geophysical Research Letters* DOI: 10.1002/2017GL074243
- McGuire LA, Rengers FK, Kean JW, Staley DM, Mirus BB. 2018. Incorporating spatially heterogeneous infiltration capacity into hydrologic models with applications for simulating post-wildfire debris flow initiation. *Hydrological Processes* DOI: 10.1002/hyp.11458

- Meyer GA, Pierce JL. 2003. Climatic controls on fire-induced sediment pulses in Yellowstone National Park and central Idaho: A long-term perspective. *Forest Ecology and Management* 178 : 89–104. DOI: 10.1016/S0378-1127(03)00055-0
- Meyer GA, Pierce JL, Wood SH, Jull AJT. 2001. Fire, storms, and erosional events in the Idaho batholith. *Hydrological Processes* DOI: 10.1002/hyp.389
- Meyer GA, Wells SG. 1997. Fire-Related Sedimentation Events on Alluvial Fans, Yellowstone National Park, USA. *Journal of Sedimentary Research* 67 : 776–791.
- Miller ME, MacDonald LH, Robichaud PR, Elliot WJ. 2011. Predicting post-fire hillslope erosion in forest lands of the western United States. *International Journal of Wildland Fire* DOI: 10.1071/WF09142
- Mock CJ. 1996. Climatic Controls and Spatial Variations of Precipitation in the Western United States. *Journal of Climate* 9 : 1111–1125.
- Montgomery DR, Dietrich WE. 1992. Channel Initiation and the Problem of Landscape Scale
- Montgomery DR, Foufoula-Georgiou E. 1993. Channel Network Source Representation Using Digital Elevation Models. *WATER RESOURCES RESEARCH* 29 : 3925–3934.
- Moody JA, Kinner DA. 2006. Spatial structures of stream and hillslope drainage networks following gully erosion after wildfire. *Earth Surface Processes and Landforms* DOI: 10.1002/esp.1246
- Moody JA, Martin DA. 2009. Synthesis of sediment yields after wildland fire in different rainfall regimes in the western United States. *International Journal of Wildland Fire* DOI: 10.1071/WF07162
- Moody JA, Shakesby RA, Robichaud PR, Cannon SH, Martin DA. 2013. Current research issues related to post-wildfire runoff and erosion processes. *Earth-Science Reviews* DOI: 10.1016/j.earscirev.2013.03.004

- Morgan JA, Brogan DJ, Nelson PA. 2016. Application of Structure-from-Motion photogrammetry in laboratory flumes. *Geomorphology* DOI: 10.1016/j.geomorph.2016.10.021
- Mosbrucker AR, Major JJ, Spicer KR, Pitlick J. 2017. Camera system considerations for geomorphic applications of SfM photogrammetry. *Earth Surface Processes and Landforms* DOI: 10.1002/esp.4066
- Murphy BP, Yocom LL, Belmont P. 2018. Beyond the 1984 Perspective: Narrow Focus on Modern Wildfire Trends Underestimates Future Risks to Water Security. *Earth's Future* DOI: 10.1029/2018EF001006
- Nelson NA, Pierce J. 2010. Late-holocene relationships among fire, climate and vegetation in a forest-sagebrush ecotone of southwestern idaho, USA. *Holocene* 20 : 1179–1194. DOI: 10.1177/0959683610371992
- Nyman P, Sheridan GJ, Smith HG, Lane PNJ. 2011. Evidence of debris flow occurrence after wildfire in upland catchments of south-east Australia. *Geomorphology* DOI: 10.1016/j.geomorph.2010.10.016
- Nyman P, Smith HG, Sherwin CB, Langhans C, Lane PNJ, Sheridan GJ. 2015. Predicting sediment delivery from debris flows after wildfire. *Geomorphology* DOI: 10.1016/j.geomorph.2015.08.023
- Orem CA, Pelletier JD. 2015. Quantifying the time scale of elevated geomorphic response following wildfires using multi-temporal LiDAR data: An example from the Las Conchas fire, Jemez Mountains, New Mexico. *Geomorphology* DOI: 10.1016/j.geomorph.2015.01.006
- Orem CA, Pelletier JD. 2016. The predominance of post-wildfire erosion in the long-term denudation of the Valles Caldera, New Mexico. *Journal of Geophysical Research F: Earth Surface* DOI: 10.1002/2015JF003663
- Passalacqua P et al. 2015. Analyzing high resolution topography for advancing the understanding of mass and energy transfer through landscapes: A review. *Earth-Science Reviews* 148 : 174–193. DOI: 10.1016/j.earscirev.2015.05.012

- Pelletier JD, Orem CA. 2014. How do sediment yields from post-wildfire debris-laden flows depend on terrain slope, soil burn severity class, and drainage basin area? Insights from airborne-LiDAR change detection. *Earth Surface Processes and Landforms* DOI: 10.1002/esp.3570
- Perreault LM, Yager EM, Aalto R. 2017. Effects of gradient, distance, curvature and aspect on steep burned and unburned hillslope soil erosion and deposition. *Earth Surface Processes and Landforms* DOI: 10.1002/esp.4067
- Pierce J, Meyer GA, Jull AT. 2004. Fire-induced erosion and millennial-scale climate change in northern ponderosa pine forests. *Nature* 432 : 87–90.
- Pierce JL, Meyer GA, Rittenour T. 2011. The relation of Holocene fluvial terraces to changes in climate and sediment supply, South Fork Payette River, Idaho. *Quaternary Science Reviews* DOI: 10.1016/j.quascirev.2010.11.013
- Pierson FB, Moffet CA, Williams CJ, Hardegree SP, Clark PE. 2009. Prescribed-fire effects on rill and interrill runoff and erosion in a mountainous sagebrush landscape. *Earth Surface Processes and Landforms* DOI: 10.1002/esp.1703
- Reimer PJ et al. 2013. IntCal13 and Marine13 Radiocarbon Age Calibration Curves 0–50,000 Years cal BP. *Radiocarbon* DOI: 10.2458/azu_js_rc.55.16947
- Reneau SL, Dietrich WE. 1991. Erosion rates in the southern oregon coast range: Evidence for an equilibrium between hillslope erosion and sediment yield. *Earth Surface Processes and Landforms* DOI: 10.1002/esp.3290160405
- Reneau SL, Katzman D, Kuyumjian GA, Lavine A, Malmon D V. 2007. Sediment delivery after a wildfire. *Geology* 35 : 151–154. DOI: 10.1130/G23288A.1
- Rengers FK, Tucker GE, Moody JA, Ebel BA. 2016. Illuminating wildfire erosion and deposition patterns with repeat terrestrial lidar. *Journal of Geophysical Research* 121 : 588–608. DOI: 10.1002/2015JF003600
- Riley K, Pierce J, Meyer GA. 2015. Vegetative and climactic controls on Holocene wildfire and erosion recorded in alluvial fans of the Middle Fork Salmon River, Idaho. *The Holocene* 25 : 857–871. DOI: 10.1177/0959683615571423

- Riley KE. 2012. A 14,000-Year Record of Wildfire and Alluvial Fan Deposition Reveals Relationships Among Fire, Climate, Vegetation, and Sediment Yields in the Middle Fork Salmon River, Idaho, Boise State University
- Roering JJ, Gerber M. 2005. Fire and the evolution of steep, soil-mantled landscapes. *Geology* DOI: 10.1130/G21260.1
- Roering JJ, Kirchner JW, Dietrich WE. 1999. Evidence for nonlinear, diffusive sediment transport on hillslopes and implications for landscape morphology. *Water Resources Research* DOI: 10.1029/1998WR900090
- Sankey JB, Germino MJ, Glenn NF. 2009. Aeolian sediment transport following wildfire in sagebrush steppe. *Journal of Arid Environments* 73 : 912–919. DOI: 10.1016/j.jaridenv.2009.03.016
- Sankey JB, Kreitler J, Hawbaker TJ, McVay JL, Miller ME, Mueller ER, Vaillant NM, Lowe SE, Sankey TT. 2017. Climate, wildfire, and erosion ensemble foretells more sediment in western USA watersheds. *Geophysical Research Letters* DOI: 10.1002/2017GL073979
- Santi PM, deWolfe VG, Higgins JD, Cannon SH, Gartner JE. 2008. Sources of debris flow material in burned areas. *Geomorphology* DOI: 10.1016/j.geomorph.2007.02.022
- Schaffrath KR, Belmont P, Wheaton JM. 2015. Landscape-scale geomorphic change detection: Quantifying spatially variable uncertainty and circumventing legacy data issues. *Geomorphology* DOI: 10.1016/j.geomorph.2015.09.020
- Schmeer SR, Kampf SK, MacDonald LH, Hewitt J, Wilson C. 2018. Empirical models of annual post-fire erosion on mulched and unmulched hillslopes. *Catena* DOI: 10.1016/j.catena.2017.12.029
- Schumm SA. 1973. Geomorphic thresholds and complex response of drainage systems. *Fluvial Geomorphology* 6 : 69–85.
- Scott D, Versfeld DB, Lesch W. 1998. Erosion and sediment yield in relation to afforestation and fire in the mountains of the western cape province, south africa. *South African Geographical Journal* DOI: 10.1080/03736245.1998.9713644

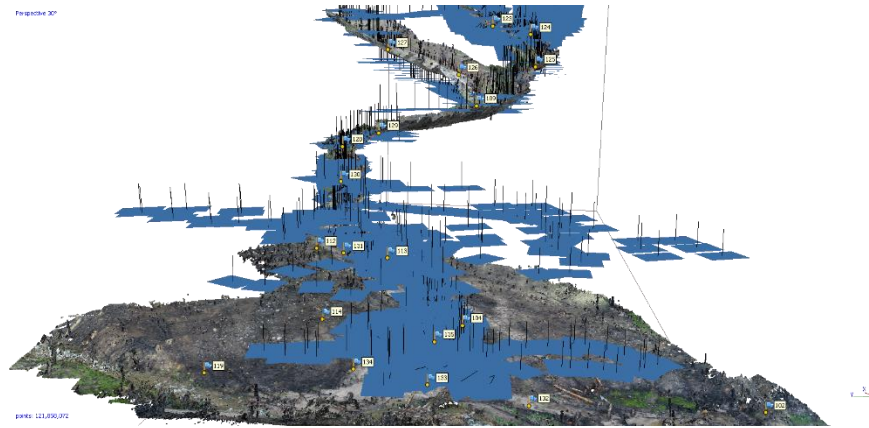
- Shakesby RA, Doerr SH. 2006. Wildfire as a hydrological and geomorphological agent. *Earth-Science Reviews* DOI: 10.1016/j.earscirev.2005.10.006
- Smith HG, Sheridan GJ, Nyman P, Child DP, Lane PNJ, Hotchkis MAC, Jacobsen GE. 2012. Quantifying sources of fine sediment supplied to post-fire debris flows using fallout radionuclide tracers. *Geomorphology* DOI: 10.1016/j.geomorph.2011.11.005
- Smith MW, Carrivick JL, Hooke J, Kirkby MJ. 2014. Reconstructing flash flood magnitudes using “Structure-from-Motion”: A rapid assessment tool. *Journal of Hydrology* DOI: 10.1016/j.jhydrol.2014.09.078
- Snyder NP, Whipple KX, Tucker GE, Merritts DJ. 2000. Landscape response to tectonic forcing: Digital elevation model analysis of stream profiles in the Mendocino triple junction region, northern California. *Geological Society of America Bulletin* 112 : 1250–1263. DOI: [https://doi.org/10.1130/0016-7606\(2000\)112<1250:LRTTFD>2.0.CO;2](https://doi.org/10.1130/0016-7606(2000)112<1250:LRTTFD>2.0.CO;2)
- Staley DM, Negri JA, Kean JW, Laber JL, Tillery AC, Youberg AM. 2017. Prediction of spatially explicit rainfall intensity–duration thresholds for post-fire debris-flow generation in the western United States. *Geomorphology* DOI: 10.1016/j.geomorph.2016.10.019
- Staley DM, Negri JA, Kean JW, Laber JM, Tillery AC, Youberg AM, Kimball SM. 2016. Updated Logistic Regression Equations for the Calculation of Post-Fire Debris-Flow Likelihood in the Western United States . Reston, Virginia
- Staley DM, Wasklewicz TA, Kean JW. 2014. Characterizing the primary material sources and dominant erosional processes for post-fire debris-flow initiation in a headwater basin using multi-temporal terrestrial laser scanning data. *Geomorphology* DOI: 10.1016/j.geomorph.2014.02.015
- Stock JD, Dietrich WE. 2006. Erosion of steepland valleys by debris flows. *Bulletin of the Geological Society of America* DOI: 10.1130/B25902.1
- Stratton BT, Sridhar V, Gribb MM, McNamara JP, Narasimhan B. 2009. Modeling the spatially varying water balance processes in a Semiarid Mountainous Watershed

- of Idaho. *Journal of the American Water Resources Association* 45 : 1390–1408.
DOI: 10.1111/j.1752-1688.2009.00371.x
- Stumpf A, Malet JP, Allemand P, Pierrot-Deseilligny M, Skupinski G. 2015. Ground-based multi-view photogrammetry for the monitoring of landslide deformation and erosion. *Geomorphology* DOI: 10.1016/j.geomorph.2014.10.039
- Swanson FJ. 1981. FIRE AND GEOMORPHIC PROCESSES
- Tamminga AD, Eaton BC, Hugenholtz CH. 2015. UAS-based remote sensing of fluvial change following an extreme flood event. *Earth Surface Processes and Landforms* DOI: 10.1002/esp.3728
- Turner D, Lucieer A, Wallace L. 2014. Direct georeferencing of ultrahigh-resolution UAV imagery. *IEEE Transactions on Geoscience and Remote Sensing* DOI: 10.1109/TGRS.2013.2265295
- Wagenbrenner JW, Robichaud PR. 2014. Post-fire bedload sediment delivery across spatial scales in the interior western United States. *Earth Surface Processes and Landforms* DOI: 10.1002/esp.3488
- Weppner KN, Pierce JL, Betancourt JL. 2013. Holocene fire occurrence and alluvial responses at the leading edge of pinyon-juniper migration in the Northern Great Basin, USA. *Quaternary Research (United States)* 80 : 143–157. DOI: 10.1016/j.yqres.2013.06.004
- Wester T, Wasklewicz T, Staley D. 2014. Functional and structural connectivity within a recently burned drainage basin. *Geomorphology* DOI: 10.1016/j.geomorph.2013.10.011
- Westoby MJ, Brasington J, Glasser NF, Hambrey MJ, Reynolds JM. 2012. “Structure-from-Motion” photogrammetry: A low-cost, effective tool for geoscience applications. *Geomorphology* DOI: 10.1016/j.geomorph.2012.08.021
- Wheaton JM, Brasington J, Darby SE, Sear DA. 2010. Accounting for uncertainty in DEMs from repeat topographic surveys: Improved sediment budgets. *Earth Surface Processes and Landforms* DOI: 10.1002/esp.1886

Wohl E et al. 2018. Connectivity as an emergent property of geomorphic systems. *Earth Surface Processes and Landforms* DOI: 10.1002/esp.4434

APPENDIX A

Structure from Motion Methods



This is intended to be a user guide to apply Structure from Motion Multi View Stereo photogrammetry to geomorphologic investigations. It describes the general guidelines and specific approaches employed to conduct the survey, process imagery into a point cloud, and produce a DEM. The examples provide support for Nicholas Ellett's Master's thesis (2019, Boise State University). References are included where relevant or helpful.

Structure from Motion Background

Structure from Motion, Multi View Stereo photogrammetry (SfM hereafter) is a relatively new development in the field of geomorphology. SfM refers to the method of deriving high-resolution topographic data (a point cloud) from multiple overlapping images. SfM reconstructs the geometry of scene by matching and triangulating features from multiple images. There are no rigid requirements for camera specification or viewpoint geometry, as in traditional stereo-photogrammetry. An algorithm called Scale Invariant Feature Transform overcomes irregular changes in perspective and scale between images and simplifies SfM implementation (Johnson et al., 2014). The primary derivative product of SfM is a point cloud containing x,y,z and r,g,b values at each point,

which can be processed similar to lidar data. The point clouds can also be simplified into gridded digital elevation or digital surface models (DEM, DSM).

SfM is capable of point densities exceeding terrestrial laser scanning (lidar, TLS) at scales of a few hundred meters. Combining the SfM process with a flexible platform, such as an unmanned aerial vehicle (UAV), is particularly well-suited to geoscience investigations at sites up to kilometer-scale where vegetation is sparse or absent. SfM is also being used with satellite images to produce DEMs at global scales (<https://www.pgc.umn.edu/data/arcticdem/> and <https://www.pgc.umn.edu/data/rema/>).

For a short list of references discussing the concepts and applications of SfM we recommend: James and Robson, 2012; Westoby et al., 2012; Johnson et al., 2014; Lucieer et al., 2014; <https://kb.unavco.org/kb/article/structure-from-motion-sfm-introductory-guide-843.html>; Mosbrucker et al., 2017; and those mentioned elsewhere in this appendix.

Other required steps

- Establish a study area.
- Take UAV test for Federal Aviation Administration (FAA) “remote pilot” license.
- Practice UAV takeoff, flight, and landing in a variety of situations, become familiar with camera controls, memory card capacity, battery life, and other UAV operations.
- Install and practice with a flight planning app, if using.

SfM Survey Steps

1: Establish ground control points

Deriving a point cloud without ground control is possible using only the UAV-integrated GPS. However, for geomorphic change detections applications especially, acquiring the best possible ground control is paramount to georeferencing the derived

point cloud accurately. Using independent ground control points (GCPs) attaches the SfM point cloud to a real-world coordinate system, from which transformations can be made if needed. Additionally, the independent ground control points can provide a metric of accuracy or uncertainty for the SfM point cloud itself.

For the established study area, ground control points should be distributed in a variety of locations and extend beyond the edges of the area of interest. A grid pattern is not required. James et al. (2017) found ~50 m spacing between GCPs was best for their application at 2 cm desired spatial resolution. Goetz et al. (2018) report that DEM precision (repeatability) was poorer at locations >40 m from a GCP. However, the actual number of GCPs depends on the study's specific goals, the accuracy of the GCP recording, and the field setting.

For our post-fire erosion study, we placed a total of 35 GCPs in an irregularly-shaped 0.2 km² area. The specific locations were chosen in the field, mixed between hillslope, channel, and debris fan areas, and judged to be stable (so that repeat surveys could utilize them). 20 of these GCPs were covered by UAV imagery and available for georeferencing the point cloud. The GCPs consisted of ~40 cm lengths of rebar hammered into the surface. Orange bucket lids were placed over the protruding rebar for visibility in UAV images and during field work. The precise GCP location were then surveyed with a TopCon HiperV real time kinematic GPS unit. A base station is setup and begins logging information from multiple satellites for at least 2 hours. A rover device mounted on a 2 m pole is used to record the location of each GCP (centered on rebar). These data were post-processed using the National Geodetic Survey's Online User

Positioning Service, providing corrected coordinates in UTM Zone 11N with explicit horizontal and vertical accuracies for each GCP.

Another option which provides georeferencing without placing GCPs is the so-called direct georeferencing method. This involves a UAV with a higher-accuracy onboard GPS than common consumer models. An example is the ~\$7000 USD DJI Phantom Rtk, which when integrated with a base station claims centimeter accuracy. See Turner et al. (2014) and Carbonneau and Dietrich (2017) for examples of direct georeferencing.

2: Conduct flights and collect images

Multiple studies address the number and type of images required for optimal SfM processing; James and Robson (2014) and Mosbrucker et al. (2017) are recommended. In order for SfM to work, each point on the ground needs to be in multiple images. This is often referred to as overlap. Overlap should be at least 70%, with more overlap for complex terrain. Most images are acquired at nadir (camera facing straight down). However, a few convergent, oblique images improve the SfM model by minimizing ‘doming’ (James and Robson, 2014).

The flying height and the camera resolution control the ground sampling distance. A high altitude and a low resolution camera will result in a less dense point cloud and a less detailed DEM, but can cover large areas. Likewise, a low flying altitude and a high resolution camera will produce a very dense point cloud and cm-details in the DEM, but only over small areas. Each study will have different requirements to balance desired detail with areal coverage. A further consideration are restrictions on UAV flight altitude; the Federal Aviation Administration requires UAVs remain below 120 m altitude.

Another consideration when acquiring images are the lightning and weather conditions. Most small, consumer UAVs function fine in gentle breezes but high winds pose a hazard. Obviously rain and fog should be avoided. The lighting conditions are also important; SfM is limited to information in images to derive point cloud models. The camera focal length should be fixed. Gimbal-mounted cameras are designed to minimize blur in images. Camera exposure and focus can be controlled automatically; most modern digital cameras do this well. Early morning, evening, and overcast conditions provide uniform lighting, minimize shadows, and reduce contrast between bright and dim areas. A lossless file format (.RAW) is an option, but for our study the .JPG images were more than sufficient. These considerations improve the quality of the individual images and the resulting SfM model.

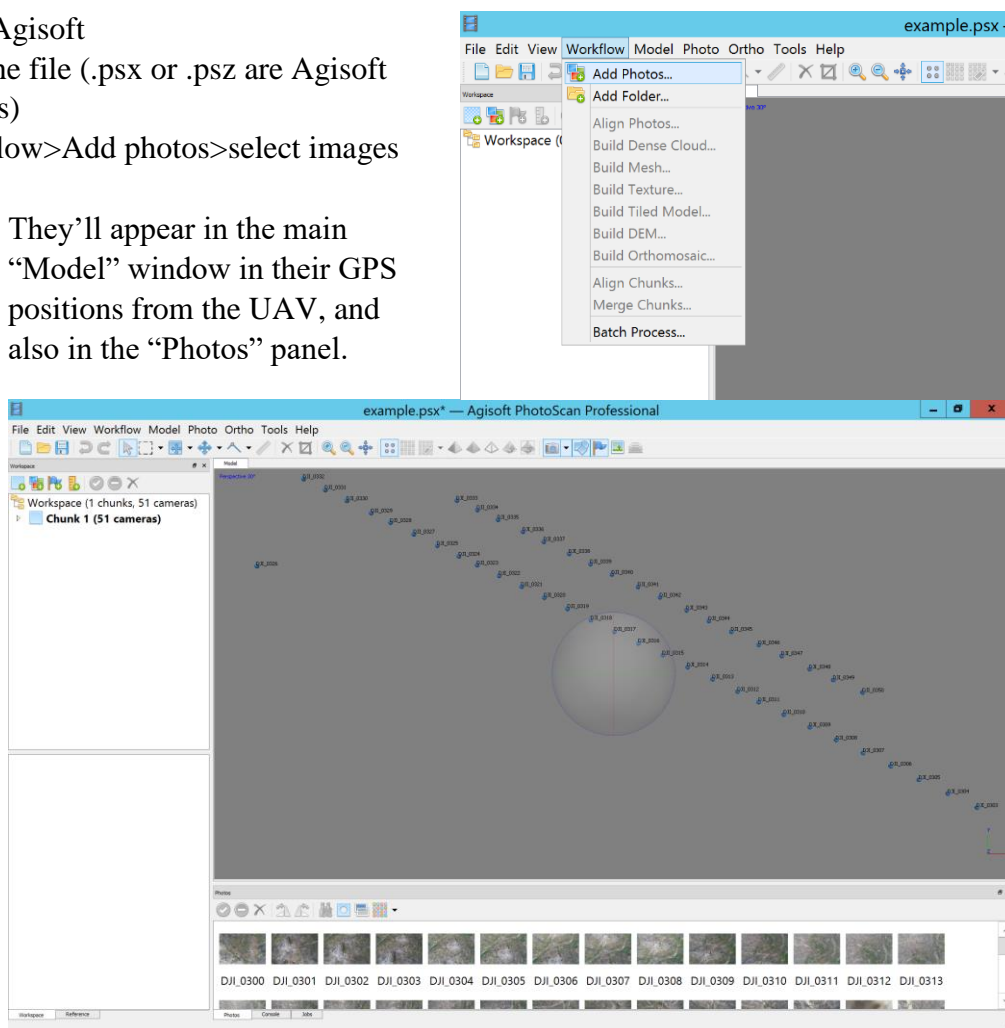
For our post-fire erosion study, we flew the UAV (DJI Phantom 4 Pro) at 20-30 m altitude and controlled it manually to avoid standing, dead trees. Most images were acquired at nadir, as suggested earlier. With the 20 megapixel camera this set up provided ground sampling distances of a few millimeters and a very dense point cloud. With ~15 minutes flight time per battery, we required 4 flights to cover the eroded channels and 2 flights to cover the debris fan deposit, a total of 0.2 km^2.

Several apps are available to plan UAV flights and can automate the process of takeoff, flying, and image collection at preset locations or time intervals, among other features. In a remote study area these require some pre-planning with an internet connection to set up the automated survey. We used one called MapPilot for iOS on a return visit to our study site in 2018; it worked well.

3: Process images using Agisoft Photoscan Professional

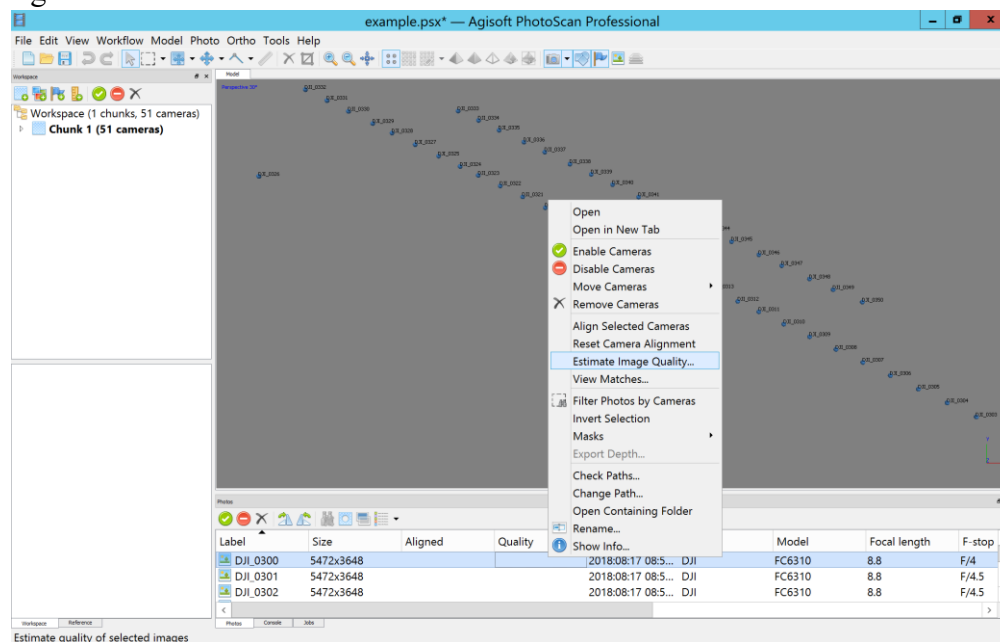
After images and GCPs are ready, they can be processed into a point cloud using the SfM workflow. Step by step instructions for Agisoft Photoscan Professional (soon to be Agisoft Metashape) follow. We also recommend this UNAVCO guide for another perspective: <https://kb.unavco.org/kb/article/structure-from-motion-sfm-agisoft-photoscan-processing-guide-848.html>

1. Open Agisoft
2. Save the file (.psx or .psz are Agisoft formats)
3. Workflow>Add photos>select images files
 - They'll appear in the main "Model" window in their GPS positions from the UAV, and also in the "Photos" panel.



4. In "Photo" panel, change view from icons to 'details'. Right click on an image and select 'estimate image quality' for all images. Sort the column from lowest to highest, remove images with quality <0.75 by selecting them and clicking the 'x' symbol, or

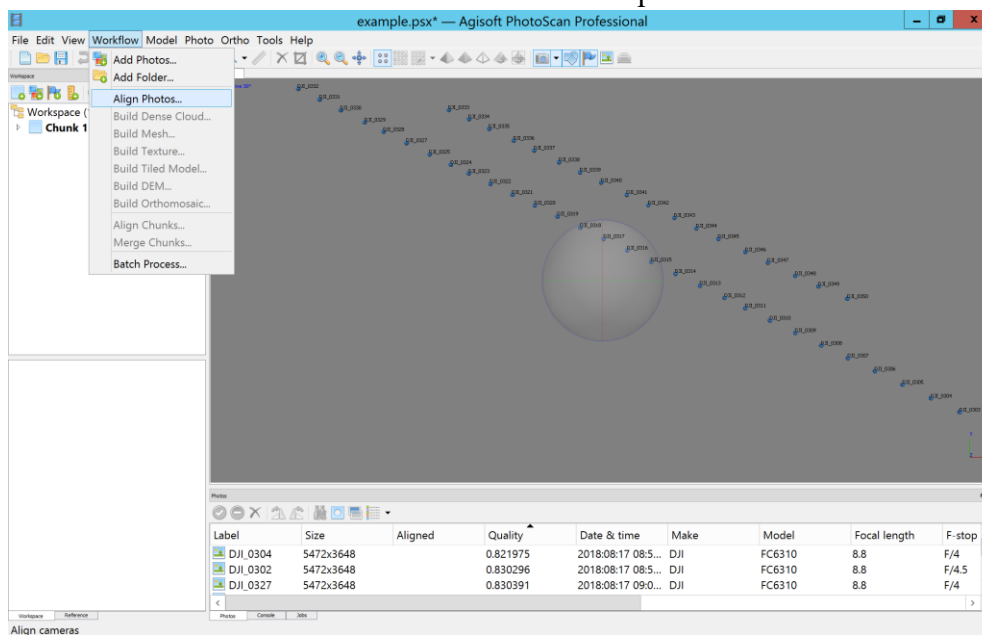
right click and select ‘remove camera’.



- These are usually blurry images. Double clicking on an image file will show the full image.

5. Workflow>Align Photos>Ok

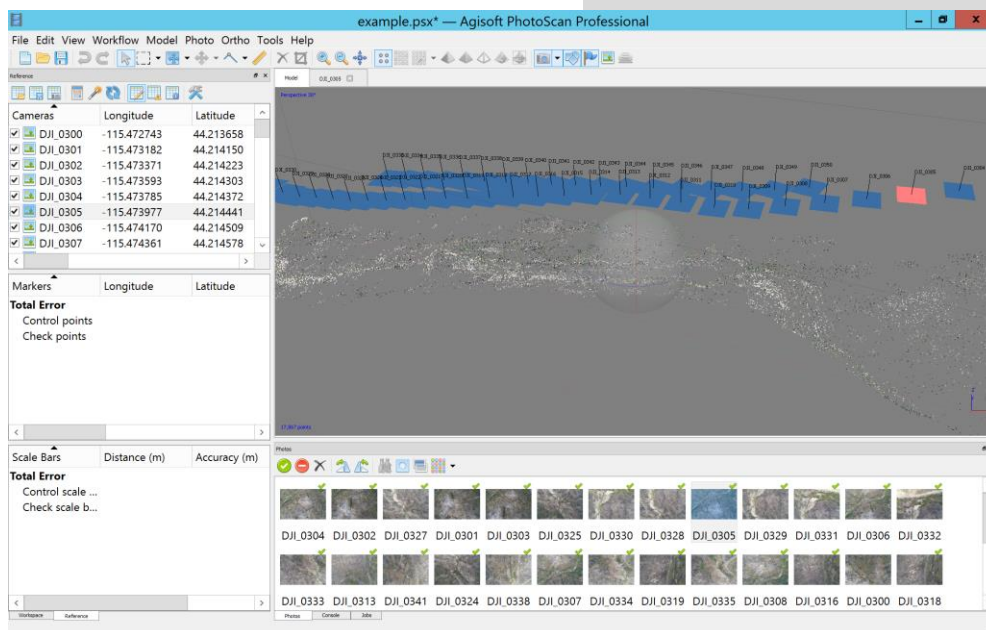
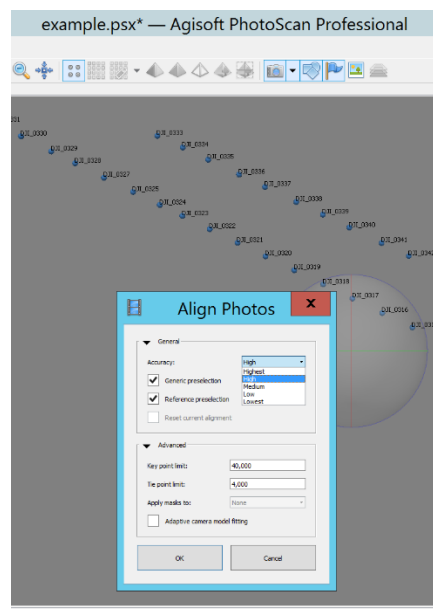
- This step creates the “sparse” point cloud. It uses a limited number of “tie points” to determine the relationship between those points in all images, and the relationship of the points to the locations images were taken from. This is one of the fundamental “Structure from Motion” processes.



- The accuracy refers to how the images are handled. “high” keeps images full size, “medium” reduces them by factor of 4, “low” reduces them another factor of 4. The full size images will take longer to process, so depending on

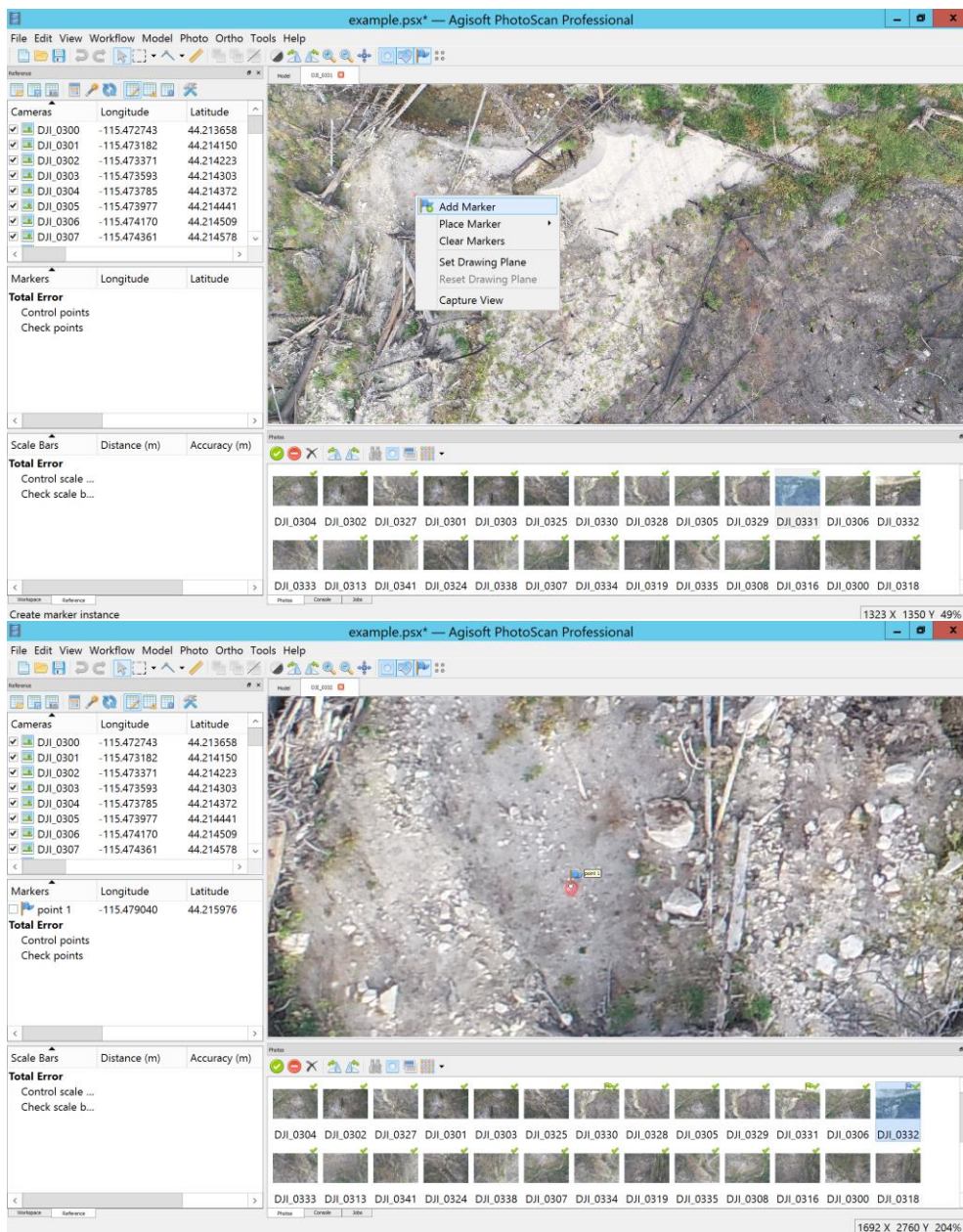
computer power, number of images, and project goals “medium” or “low” may be appropriate.

- We used “high” on the post-fire erosion project with good results
- Other parameters can be left as default
- After alignment completes, a point cloud will appear in the main “Model” window. It can be rotated, zoomed, etc. using mouse functions. The “Workspace” panel shows some details such as how many cameras (images) were aligned, and how many points are in the sparse point cloud.
- Save project.



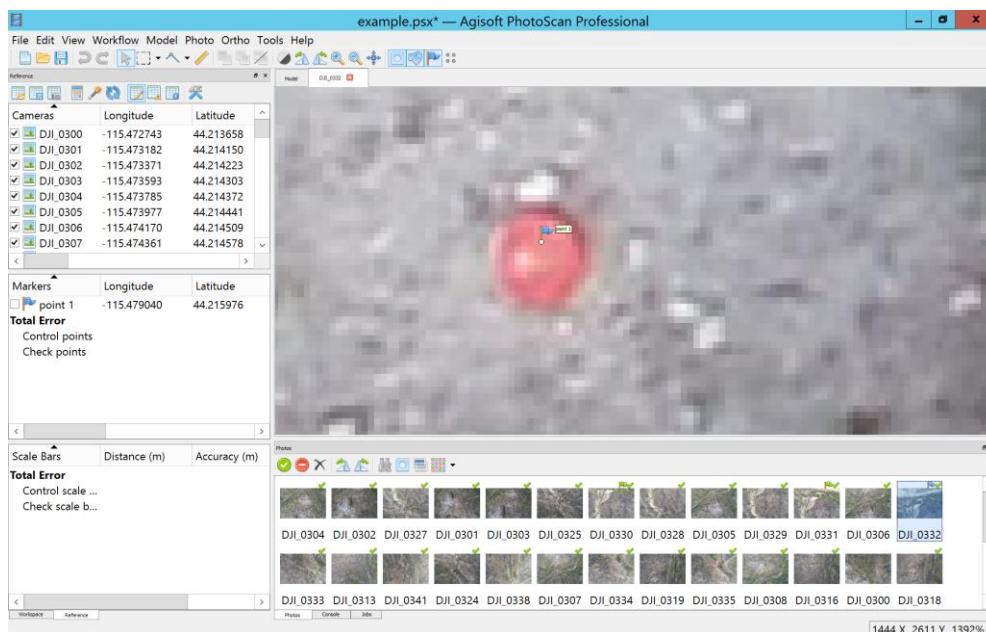
6. Assign GCP locations

- Double-click an image in the “Photos” panel that has a known GCP in it.
- Right click and select ‘Add marker’. Zoom in and adjust the flag position to be the exact center of the GCP target.

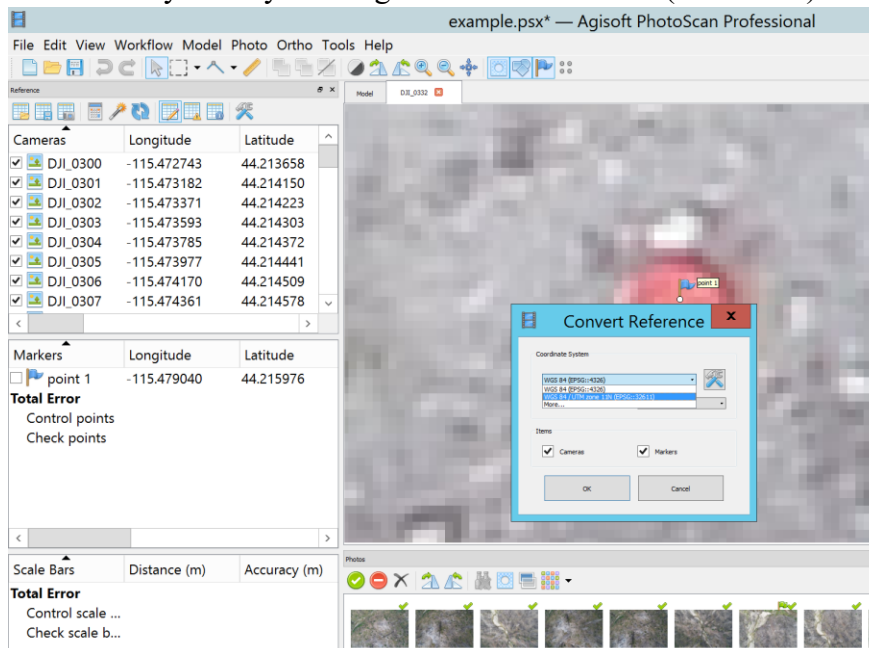


- Find that same GCP in another image, right click and select 'place marker 1'. Adjust the flag position to the exact center of the GCP.
- After this, Agisoft will find all images that contain that GCP and they will have blue flags in the "Photos" panel.
- Go through each image (with blue flag) individually and adjust the flag position to the exact center of the GCP, the flag will change to green. If the GCP is not in an image that has a blue flag, right click and select 'Remove

marker’.

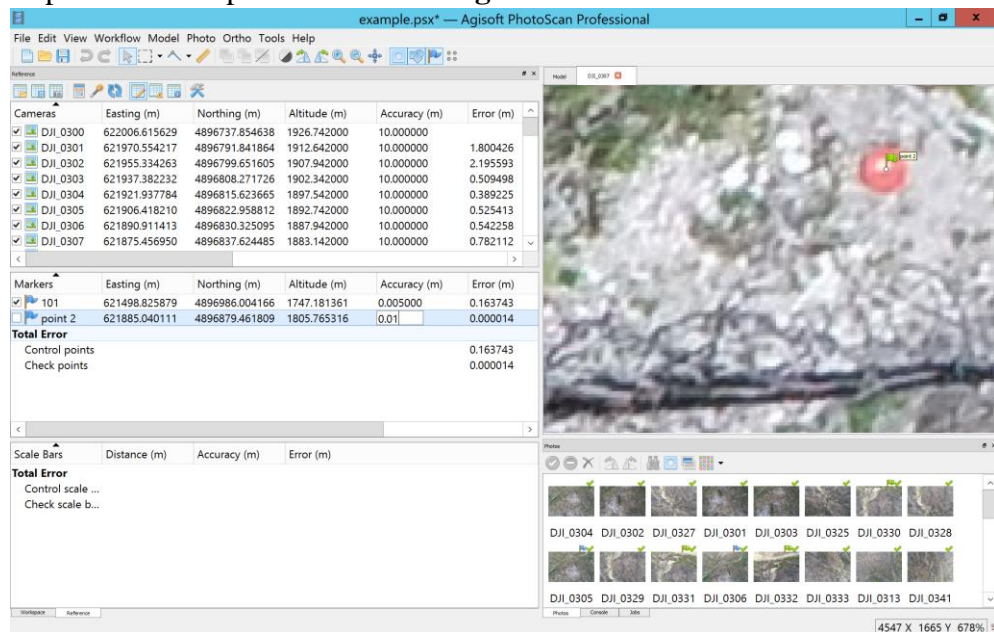


- Select the “Reference” tab (same panel as “Workspace”). It shows the UAV position information for each image (from UAV GPS, low accuracy) in the upper portion and the ‘markers’ in the lower portion.
- If needed, change the coordinate system from lat/lon to RTK GPS survey coordinate system by clicking the ‘calculator’ icon (“Convert”).

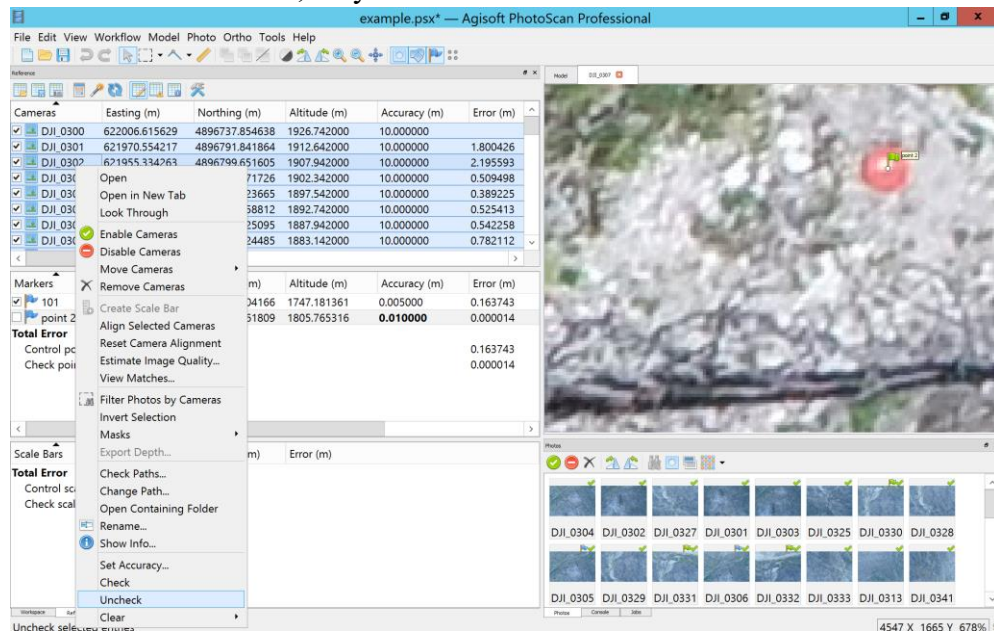


- Rename the markers to match RTK GPS data. Input the GCP coordinates, and the GCP error, from the RTK GPS post-processed data by clicking each field.

- Repeat above steps for **all remaining GCPs**.

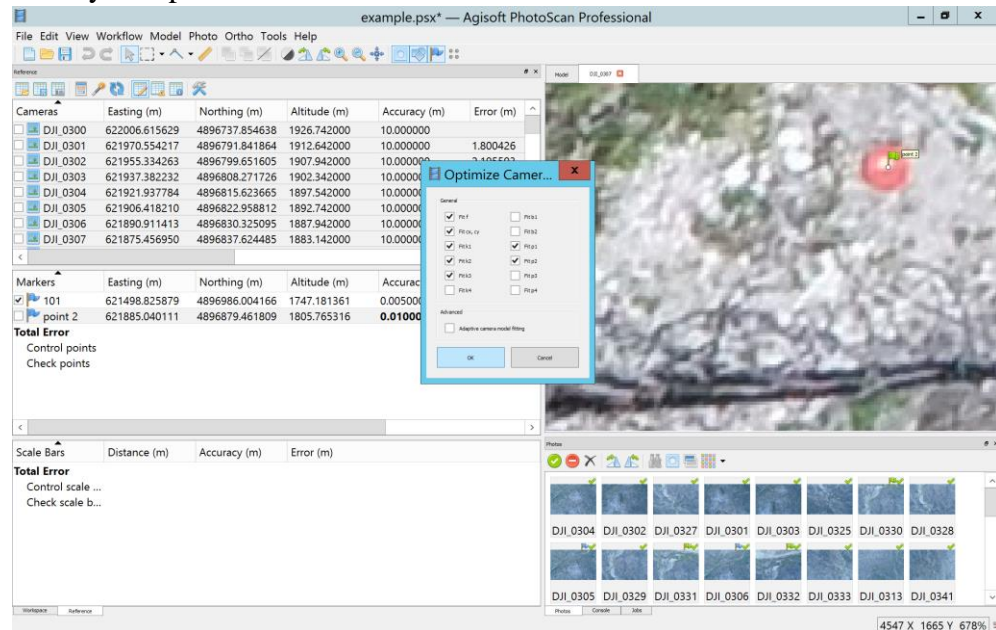


- In “Reference” tab, select all images, right click and select **‘unchecked’**. This allows Agisoft to consider only the higher-accuracy GCP locations for further steps, and ignore the lower-accuracy UAV GPS locations. Leaving the images checked will confuse Agisoft because it will try to rectify the UAV locations and the GCP locations; they aren’t the same.



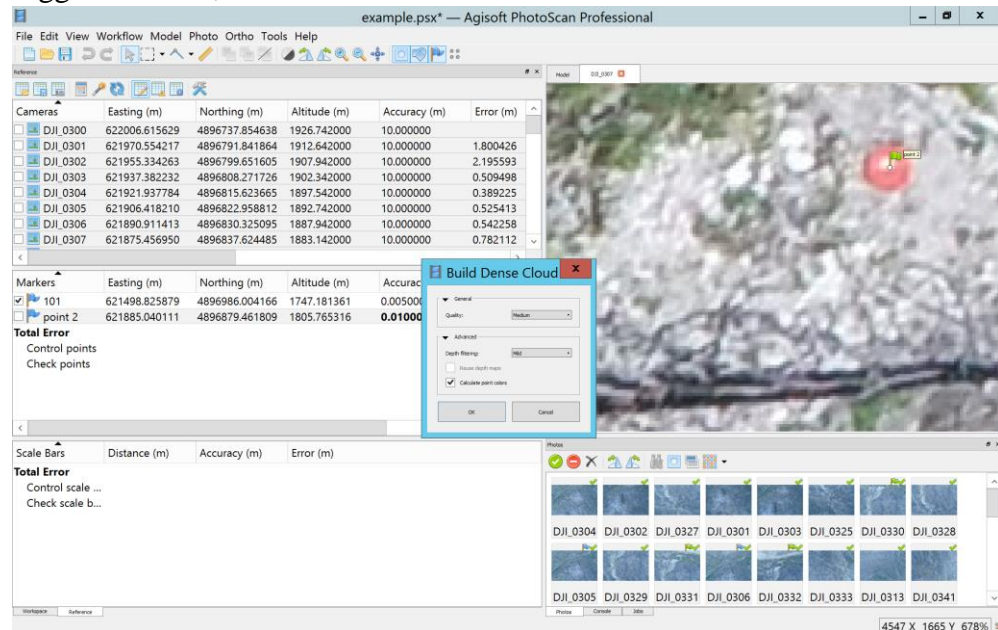
- Save project
7. In “Reference” tab, click the ‘wand’ icon to **“optimize”** the sparse point cloud.
 - This balances the rigid GCP locations with the estimated or aligned “tie points” and camera locations in the sparse cloud. The default parameters are

usually acceptable.

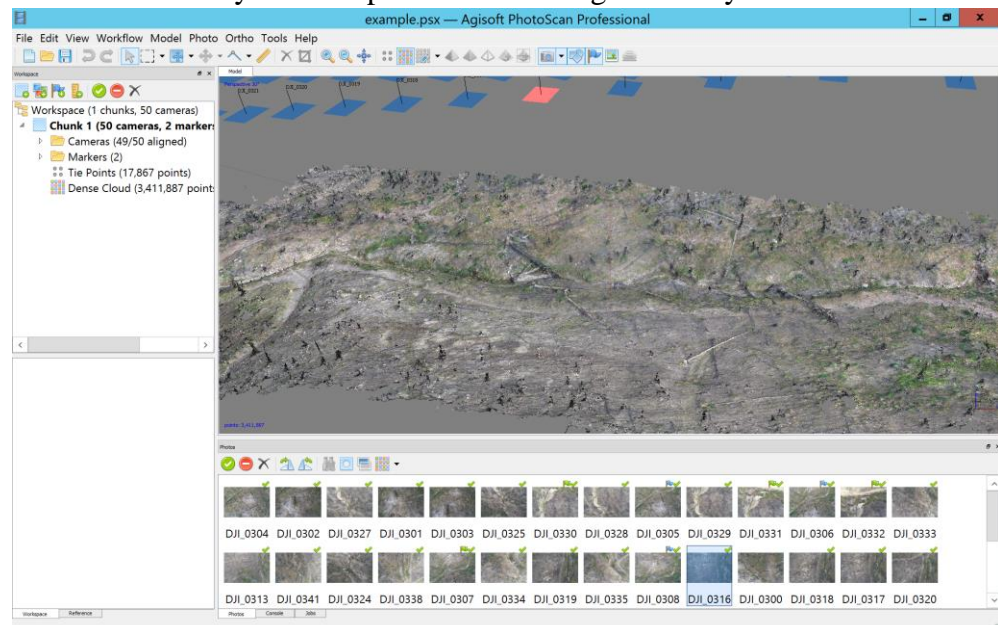


- An error for each GCP will be shown in the “Reference” tab, as well as an overall error, calculated as the RMSE between the known RTK GPS GCP location and the SfM model placement of that point.
 - If some ‘marker’ GCPs are unchecked, they provide an independent estimate of error (check points); only checked GCPs (control points) are used to georeference the SfM model.
 - Save project.
8. Workflow>Build Dense Cloud
- First, Resize the region of interest (bounding box) to ensure the entire sparse cloud is contained. Agisoft ignores areas outside that box.
 - Build Dense Cloud>Quality setting is similar to “Accuracy” parameter from the sparse cloud; the “high” setting preserves images full-size, but takes longer. “High” quality also tends to produce a noisy surface, whereas lower quality settings are often sufficiently dense but with a less noisy surface.
 - The Depth filtering setting adjust how Agisoft considers vertical deviations; “Aggressive” depth filtering removes high and low points and produces a smoother surface, good if small details don’t matter. “Mild” or “disabled” retains those vertical differences between points; good for small details and

rugged surfaces, but can contain a lot of noise.



- These parameters require some experimentation. They depend on camera quality and flying height, the landscape characteristics, processing power, and the purpose of the SfM model.
- We used “Medium” quality and “Moderate” depth filtering for our post-fire erosion study.
- When processing completes, the dense cloud will be visible by selecting the icon at the top of the “Model” window.
- It should be a very life-like point cloud. Navigation is by mouse functions.



- If it is excessively noisy, distorted, or otherwise not suitable, earlier settings will have to be changed and the dense cloud re-processed.

- Any changes to markers (GCPs), clicking “optimize” again, or any other changes will remove the dense cloud and it will have to be reprocessed.
- This is the final, georeferenced point cloud. The “Reference” tab Total Error is a measure of accuracy including GCP error and SfM model error.
- Save project.

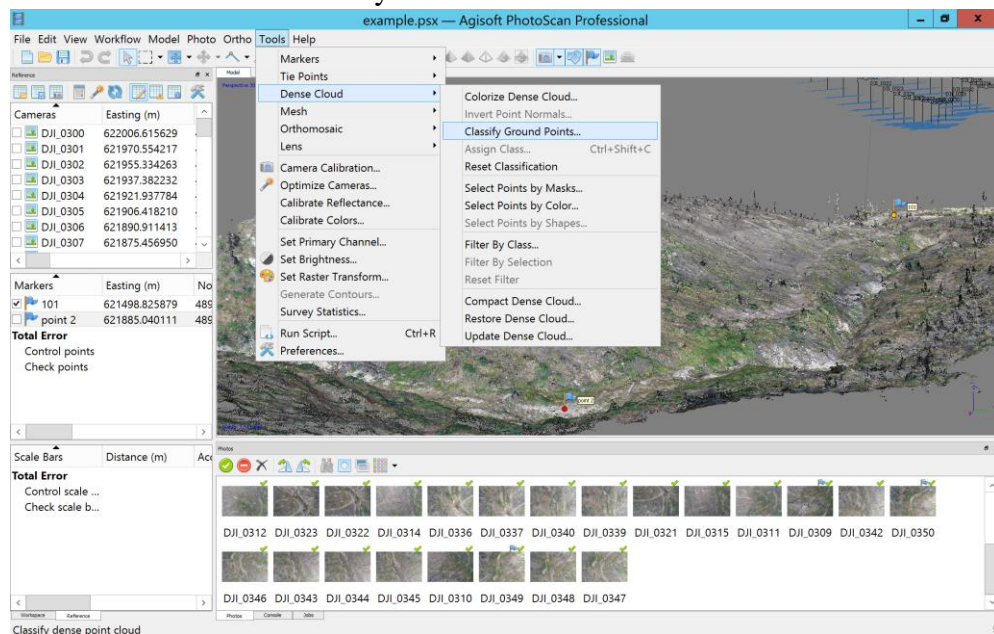
9. Export point cloud as .LAZ or .LAS file

- File>Export>Export points
- .LAS and .LAZ or standardized point cloud formats used by lidar.

Optional steps:

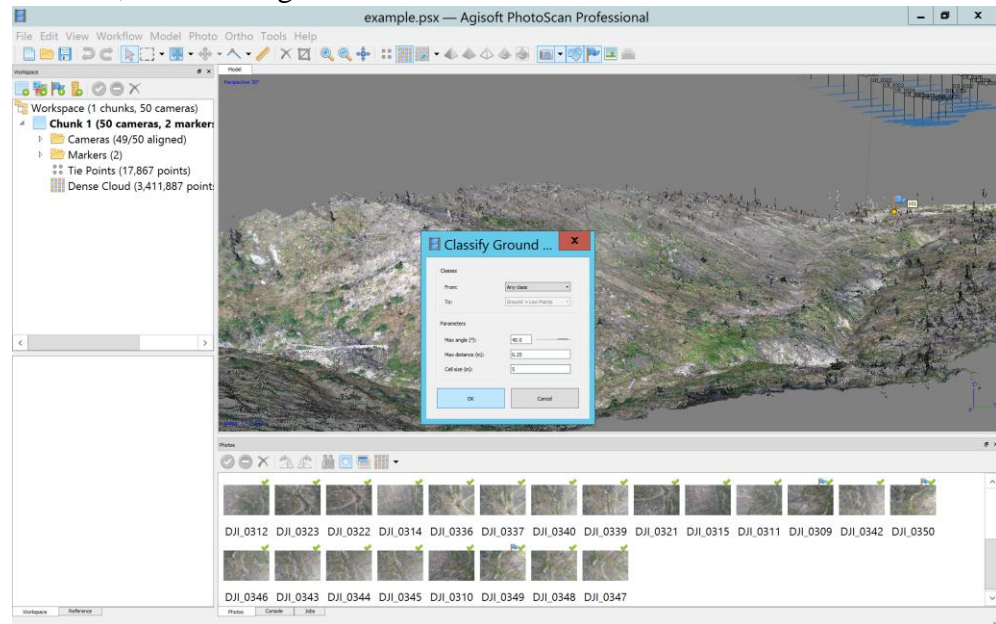
10. Classify dense point cloud

- Agisoft has a tool to classify the point cloud into “ground” and non-ground points, as is common for lidar data.
- Tools>Dense Cloud>Classify Ground Points

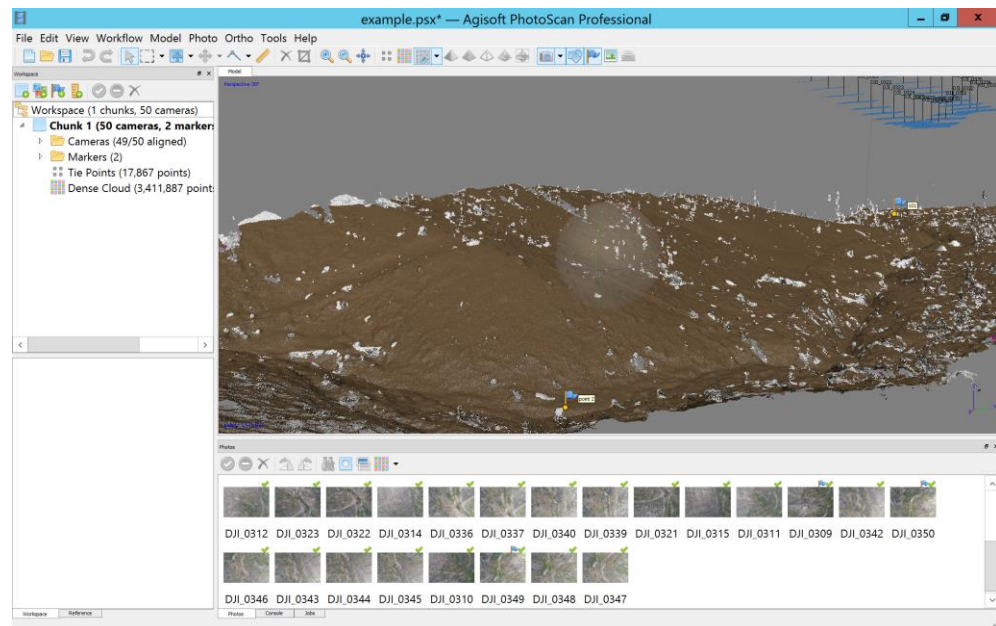


- Again, this requires some experimentation. Regions below the Max angle parameter will be considered for classification as ground points. The Max distance parameter is a threshold, below which points can be classified as ground. The Cell size parameter computes a surface using a neighborhood of

that size, the Max angle and Max distance are taken from that surface.



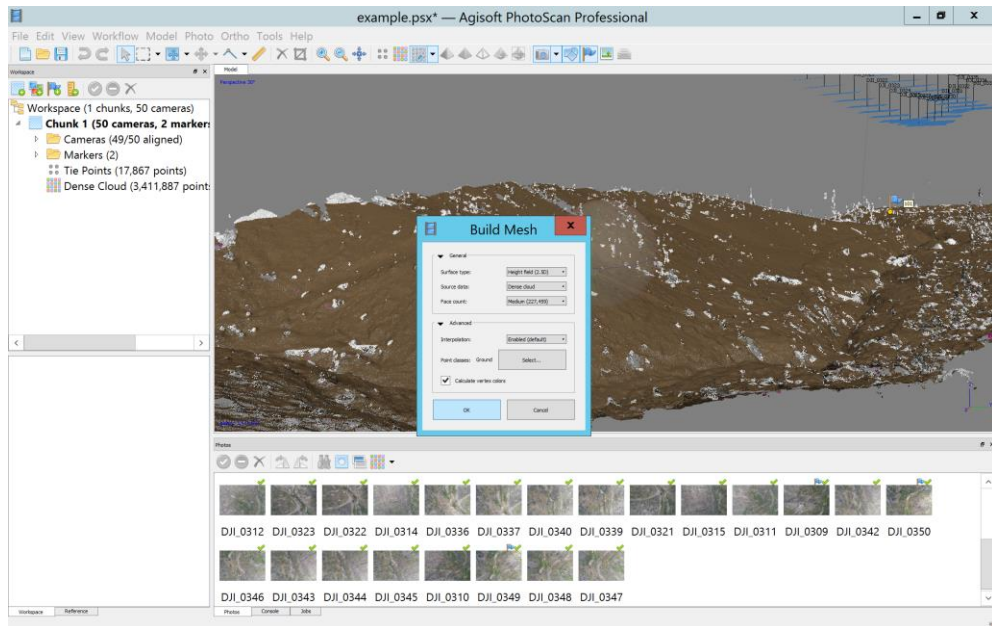
- View results by selecting the ‘greyed’ dense cloud icon above the main “Model” window.
- Brown points are classified as ground, grey is unclassified, and pink is low noise.



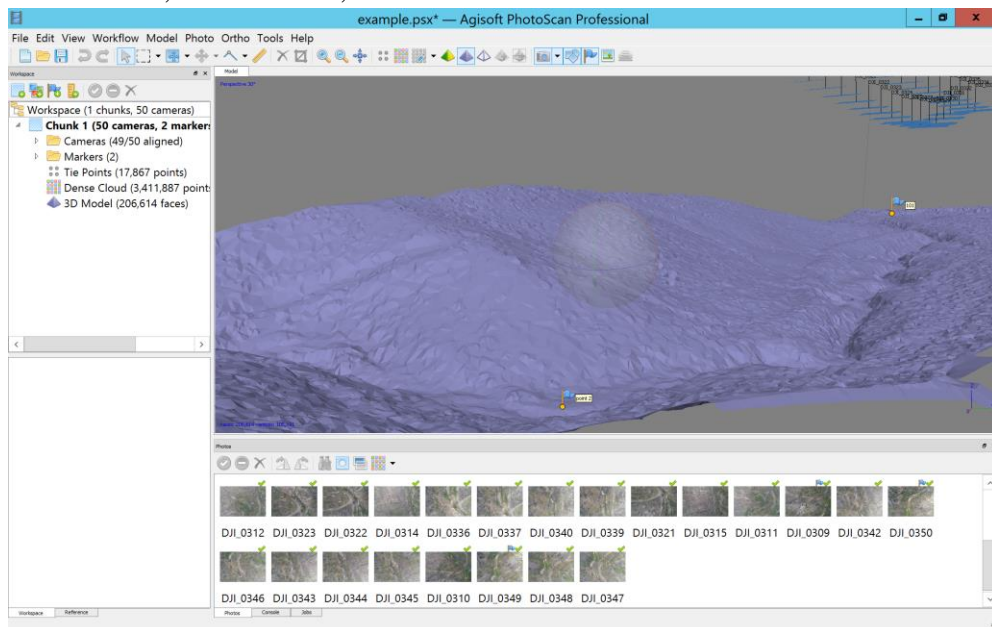
- If the classification is satisfactory, save the project and export the .LAZ again. It will now contain classified points viewable in other software.
- If the classification is unsatisfactory, go to Tools>Dense Cloud>Reset Classification, then repeat the “Classify ground points” step with different parameters.

11. Generate an orthomosaic

- Workflow>Build Mesh

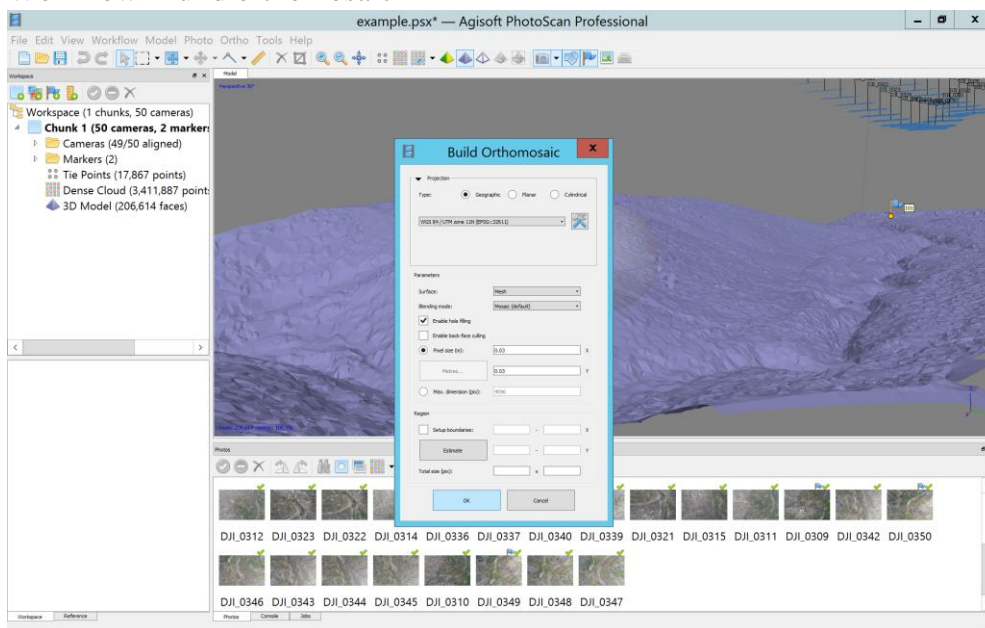


- Surface type is arbitrary if a very complex scene, select height field for most terrain types. Source data should be dense cloud for the most detail possible. Face count is the complexity of the mesh surface; default Medium is good. In ‘Advanced’, the mesh can be built from only ground-classified points, if desired for the purpose of project.
- Now three icons are enabled above the main “Model” window; for a colored mesh model, a solid mesh, or a wire mesh.



- Save project.
- Building the mesh is required before an orthomosaic or a DEM can be created in Agisoft.

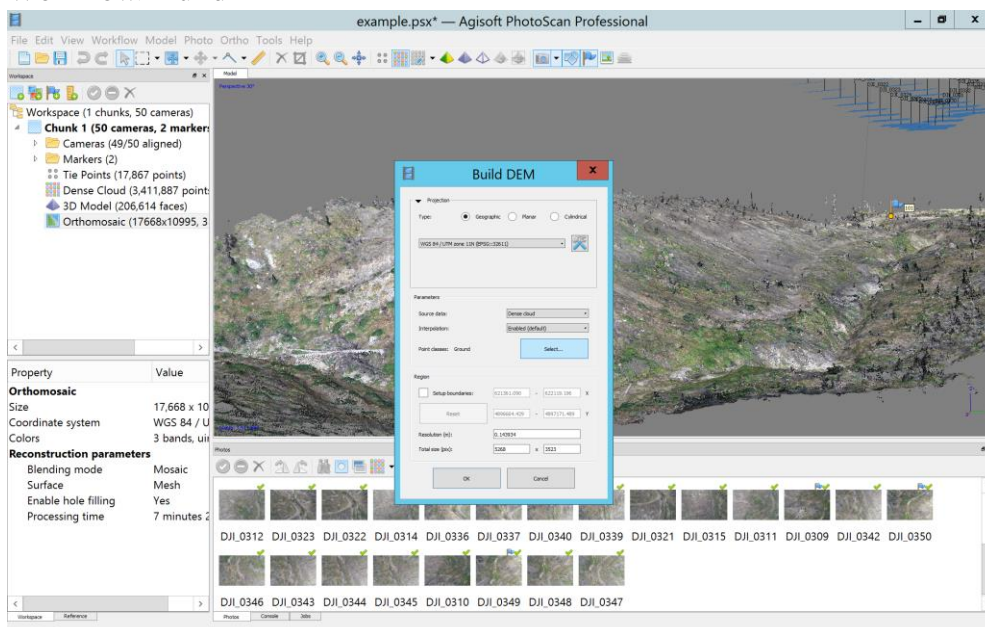
- Workflow>Build orthomosaic



- The default settings are usually good. Ensure the desired coordinate system is shown. The pixel size can be adjusted, as default Agisoft uses a very small pixel size (high resolution) based on the images themselves.
- After processing completes, save the project. The orthomosaic can be exported (as a GeoTIFF) for display or use in another program using File>Export>Export Orthomosaic.

12. Generate a DEM

- Workflow>Build DEM

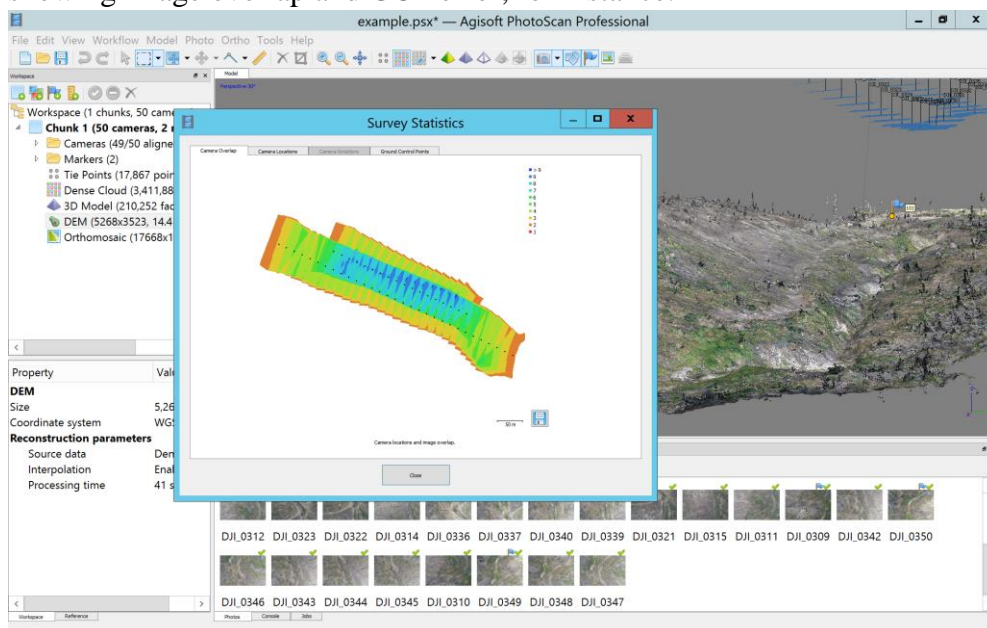


- Settings are similar to orthomosaic, above and defaults are usually good.

- Ensure coordinate system is correct. Choose Dense cloud as Source data. Choose Ground class only if desired for project.
- Save project. File>Export>Export DEM (as a GeoTIFF).

Other Agisoft functions:

- Export .kmz for Google Earth: File>Export>Export Orthomosaic>Export Google KMZ. Drag this into Google Earth to view high-resolution orthomosaic within the Google Earth context.
- Generate survey statistics: Tools>Survey Statistics. This creates a few figures showing image overlap and GCP error, for instance.



- Generate processing report: File>Export>Generate Report. This creates a PDF showing the complete processing parameters, calibration, error, and other factors. Several helpful figures are produced.

Example report

Processing Report
25 January 2019



Processing Parameters

General	
Cameras	50
Aligned cameras	49
Markers	2
Coordinate system	WGS 84 / UTM zone 11N (EPSG::32611)
Rotation angles	Yaw, Pitch, Roll
Point Cloud	
Points	17,867 of 18,769
RMS reprojection error	0.11316 (2.11164 pix)
Max reprojection error	0.340604 (30.512 pix)
Mean key point size	16.6923 pix
Point colors	3 bands, uint8
Key points	No
Average tie point multiplicity	2.46635
Alignment parameters	
Accuracy	Low
Generic preselection	Yes
Reference preselection	Yes
Key point limit	40,000
Tie point limit	4,000
Adaptive camera model fitting	No
Matching time	21 minutes 6 seconds
Alignment time	5 minutes 20 seconds
Dense Point Cloud	
Points	3,411,887
Point colors	3 bands, uint8
Reconstruction parameters	
...	1 ...

4. Further steps and analyses

Agisoft provides a great way to produce a point cloud and other products, and has more functionality than is discussed above. However, other programs can be advantageous; an Agisoft DEM could be exported to ArcMap and orthomosaics can be analyzed using ENVI.

For point cloud manipulation, analysis, and further processing we recommend CloudCompare (<https://www.danielgm.net/cc/>). This is an open-source program designed for point clouds. There is an active forum (<https://www.danielgm.net/cc/forum/>) and a helpful Wiki page for it (http://www.cloudcompare.org/doc/wiki/index.php?title=Main_Page). CloudCompare is user-friendly and exploration is encouraged. For our post-fire erosion study, we produced the raw point cloud in Agisoft and then used CloudCompare for extensive exploration, refinement, and processing. CloudCompare has more options to control DEM creation than Agisoft, and a suite of CloudCompare tools are available (and updated regularly) for advanced point cloud functions.

The CloudCompare functions we used for our post-fire erosion study included segmenting the point cloud, subsampling the point cloud (reduce point density to ease processing demand), generating statistics, calculating elevation contours, creating mesh surfaces, filtering noise points (Statistical Outlier Removal tool), filtering ground and non-ground classified points, and creating and exporting DEMs, among others.

APPENDIX B

Radiocarbon data



**THE UNIVERSITY
OF ARIZONA**

**UNIVERSITY OF ARIZONA
AMS LABORATORY**

RADIOCARBON ANALYTICAL REPORT

Ellett, N. (AA111128 - AA111130)

Order #2056

UNIVERSITY OF ARIZONA AMS LABORATORY

Ellett, N. (AA111128 - AA111130) – Radiocarbon Analytical Report

Summary Page

The following analytical report contains 14C analysis from the University of Arizona. This report contains:

1. Summary page, includes data qualifiers, non-conformances, and data summary (page 1)
2. Individual sample reports (pages 2-4)

Data Qualifiers: Fraction Modern Carbon and Radiocarbon Age were calculated as weighted averages of combined machine runs to reduce overall error. A small sample correction is applied to samples with a carbon mass less than 0.50 mg.

Non-Conformances: None.

Report generated by: Richard Cruz

Report Generation Date: 4/11/2018

Reviewer: Greg Hodgins

Date: 4/11/2018

Signature:


Data Summary

AA	lab #	sample ID	MATERIAL	MASS (mg)	d13C value	Fraction Modern	14C age BP
AA111128	X32824	4-2	charcoal	1.35	-23.5	0.9279 +- 0.0021	601 +- 18
AA111129	X32825	4-6	charcoal	1.89	-23.3	0.6100 +- 0.0016	3970 +- 21
AA111130	X32826	4-4	charcoal	1.93	-27.7	0.9248 +- 0.0022	628 +- 19

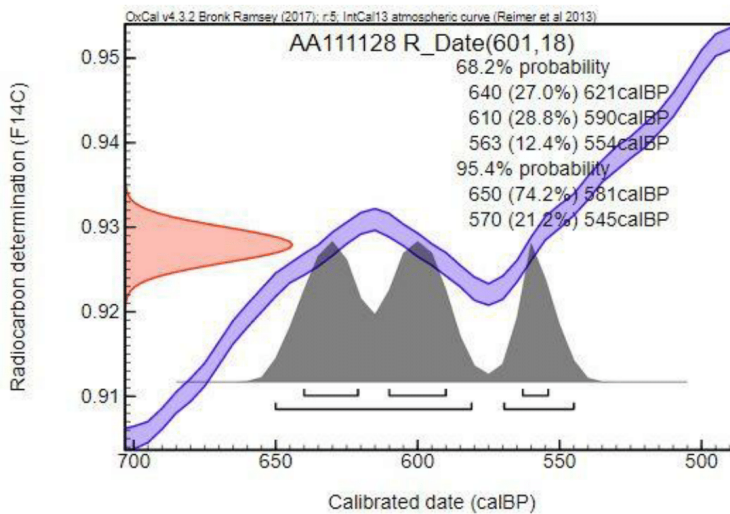
UNIVERSITY OF ARIZONA AMS LABORATORY

Ellett, N. (AA111128 - AA111130) – Radiocarbon Analytical Report

Data Report (1 of 3)

<i>User Information</i>	<i>Laboratory Information</i>
Submitter: Ellett, N.	AA-number: AA111128
User ID: 4-2	Laboratory number: X32824
Expected age: 2000 BP	Sample type: charcoal
Sample origin: Clear Creek, Idaho	Pretreatment: ABA
	Carbon yield: 57%
	Carbon mass: 1.35 mg

<i>Results</i>	
$\delta^{13}\text{C}$ ($\pm 0.1\%$, 1σ):	-23.5 ‰
Fraction of modern carbon ($\pm 1\sigma$):	0.9279 \pm 0.0021
Uncalibrated ^{14}C Age ($\pm 1\sigma$):	601 \pm 18 ^{14}C years BP
Calibration Program / Dataset:	OxCal 4.2 / IntCal13 atmospheric
Calendar Age Range (68%):	640 calBP to 554 calBP
Calendar Age Range (95%):	650 calBP to 545 calBP



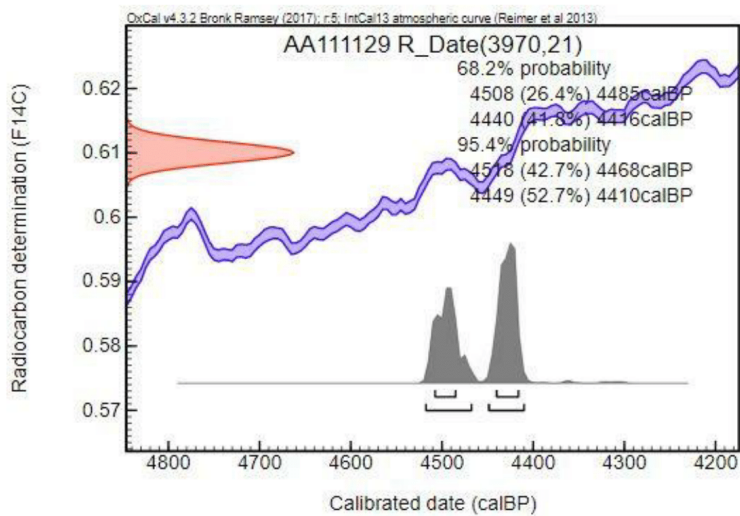
UNIVERSITY OF ARIZONA AMS LABORATORY

Ellett, N. (AA111128 - AA111130) – Radiocarbon Analytical Report

Data Report (2 of 3)

<i>User Information</i>	<i>Laboratory Information</i>
Submitter: Ellett, N.	AA-number: AA111129
User ID: 4-6	Laboratory number: X32825
Expected age: 6000 BP	Sample type: charcoal
Sample origin: Clear Creek, Idaho	Pretreatment: ABA
	Carbon yield: 58%
	Carbon mass: 1.89 mg

<i>Results</i>	
$\delta^{13}\text{C}$ ($\pm 0.1\text{‰}$, 1σ):	-23.3 ‰
Fraction of modern carbon ($\pm 1\sigma$):	0.6100 \pm 0.0016
Uncalibrated ^{14}C Age ($\pm 1\sigma$):	3970 \pm 21 14C years BP
Calibration Program / Dataset:	OxCal 4.2 / IntCal13 atmospheric
Calendar Age Range (68%):	4508 calBP to 4416 calBP
Calendar Age Range (95%):	4518 calBP to 4410 calBP



UNIVERSITY OF ARIZONA AMS LABORATORY

Ellett, N. (AA111128 - AA111130) – Radiocarbon Analytical Report

Data Report (3 of 3)

<i>User Information</i>	<i>Laboratory Information</i>
Submitter: Ellett, N.	AA-number: AA111130
User ID: 4-4	Laboratory number: X32826
Expected age: 4000 BP	Sample type: charcoal
Sample origin: Clear Creek, Idaho	Pretreatment: ABA
	Carbon yield: 63%
	Carbon mass: 1.93 mg

<i>Results</i>	
$\delta^{13}\text{C}$ ($\pm 0.1\text{‰}$, 1σ):	-27.7 ‰
Fraction of modern carbon ($\pm 1\sigma$):	0.9248 \pm 0.0022
Uncalibrated ^{14}C Age ($\pm 1\sigma$):	628 \pm 19 14C years BP
Calibration Program / Dataset:	OxCal 4.2 / IntCal13 atmospheric
Calendar Age Range (68%):	652 calBP to 561 calBP
Calendar Age Range (95%):	660 calBP to 555 calBP

